Synthesis of Platinum Rare Earth Alloy Catalysts for Fuel Cells

Knudsen, Brian Peter; Chorkendorff, Ib; Stephens, Ifan

Publication date:
2016

Document Version
Publisher's PDF, also known as Version of record

Citation (APA):
Knudsen, B. P., Chorkendorff, I., & Stephens, I. (2016). Synthesis of Platinum Rare Earth Alloy Catalysts for Fuel Cells. Department of Physics, Technical University of Denmark.

Synthesis of Platinum Rare Earth Alloy Catalysts for Fuel Cells

PhD dissertation by

Brian Peter Knudsen

Supervisor: Professor Ib Chorkendorff
Co-supervisor: Associate Professor Ifan E. L. Stephens

Kongens Lyngby 2016

This is the description of the front page image

Technical University of Denmark
Department of Physics
Center for Individual Nanoparticle Functionality (CINF)
Fysikvej, building 311,
2800 Kongens Lyngby, Denmark
Phone +45 4525 3344
info@fysik.dtu.dk
www.fysik.dtu.dk

Preface

This thesis is submitted as partial fulfilment of the PhD degree in physics at the Technical University of Denmark (DTU). The work herein was carried out at the Department of Physics and the Center for Individual Nanoparticle Functionality (CINF), from December 2012 until June 2016. The work was supervised by professor Ib Chorkendorff and associate professor Ifan E. L. Stephens. The work was funded by The Department of Physics and in part by the Innovation Fund Denmark project NACORR, project no. 12-132695.

I would like to thank my supervisors for granting me the opportunity to work on such a challenging but rewarding project and for the sublime research environment they have established. With great possibilities both physical, in the form of facilities, and mentally in the form of a stimulating atmosphere formed by former and present colleagues. I would like to thank them all for making my time at CINF so memorable. They have always been happy to share and discuss ideas, both those useful for the work and also those without any meaning. A special thank you has to go to the persons at CINF that I have had the pleasure of working directly with during my PhD studies: Amado Velázquez-Palenzuela, Claudie Roy, Christoffer Mølleskov Pedersen, Paolo Malacrida, Patricia Hernandez-Fernandez and Jacqueline McAnulty. Robert Jensen and Kenneth Nielsen have also been of great help with their knowledge and repair work on the Theta Probe. I would also like to thank my colleagues that had to share an office with me and especially Rasmus Frydendal, whom I have had the pleasure of studying with since 2007. I have always enjoyed our conversations about everything and nothing.

I also have to thank my family for their understanding in the last period of the project and for always supporting me, and encouraging me when I first started to dabble with the idea of studying physics back in primary school. Finally, Tine has been the one carrying me through it all, always there to pick me up if I was down, always ready to be there if needed. Without her I would never have made it. I look forward to spend far more time with you and see where things will take us from here.

Kongens Lyngby, 14th June 2016
Brian Peter Knudsen

Abstract

This PhD thesis presents the work performed on synthesising catalytically active platinum rare earth alloys for use in fuel cells. For fuel cells to become an integral part of the future transportation sector, the activity of platinum, the cathode catalyst of choice, has to be improved significantly. Alloying is a common way to improve the activity of platinum, however, true long term stability of the common alloys of platinum and late transition metals is unknown and could suffer from the low heat of formation.

A group of alloys that are active and have strong heats of formation, possibly enabling enhanced long term stability, is those of platinum and the rare earth elements. These have shown six fold improvement over pure platinum, for bulk crystals, and an impressive mass activity of $3.6\,\mathrm{A\ mg_{Pt}^{-1}}$ for mass selected $\mathrm{Pt}_x\mathrm{Gd}$ nanoparticles, prepared by magnetron sputtering. However, these alloys have not yet been produced by a scalable method that allows for practical application.

Herein methods for scalable synthesis of carbon supported platinum rare earth alloys are explored. Cathodic corrosion proved promising given further optimisation are done, however, high temperature reduction of rare earth precursors into commercial Pt/C was found to be the most promising method. The thermodynamics of the system was explored and the synthesis is found to be feasible at temperatures from 500 °C. The many alloy phases for platinum rare earth alloys, that are very closely related in structure, complicated the characterisation of the system.

Through optimisation of the initial synthesis setup an active Pt-Y alloy catalyst was formed showing an increase in mass activity from $0.27 \pm 0.07\,\mathrm{A\ mg_{Pt}^{-1}}$ to $0.41 \pm 0.01\,\mathrm{A\ mg_{Pt}^{-1}}$. This initial activity for a new group of catalysts, produced for the first time by a scalable method is very promising. However, further work into phase purity and alloying conditions is needed to fully realise the potential of this group of catalysts.

Resume

Denne ph.d. afhandling præsenterer arbejdet med, at syntetisere katalytisk aktive legeringer mellem platin og de sjældne jordarter til brug i brændselsceller. For at brændselsceller kan blive en væsentlig del af den fremtidige transportsektor skal aktiviteten af platin, som er den foretrukne katodekatalysator, øges drastisk. En ofte anvendt metode til, at øge aktiviteten af platin er at legere det med et af de sene overgangsmetaller. Den endelige Stabilitet af disse legeringer i brændselscellemiljøet er dog ukendt, og kan fejle på grund af den lave formationsenergi for disse legeringer.

En gruppe af legeringer der både er aktive og har høje formationsenergier, der muligvis kan sikre høj stabilitet, er legeringer mellem platin og de sjældne jordarter. Disse legeringer har udvist seks gange den aktivitet der ses for platin når der måles på makroskopiske krystaller. For massefiltrerede $\mathrm{Pt}_x\mathrm{Gd}$ nanopartikler, fremstillet med magnetron katodeforstøvning, har masse aktivitet været imponerende med $3.6\,\mathrm{A\ mg}_{\mathrm{Pt}}^{-1}$. Disse legeringer er dog aldrig blevet fremstillet med en skalerbar metode der tillader praktiske anvendelser.

Heri bliver metoder for den skalerbare syntese af legeringer mellem platin og de sjældne jordarter undersøgt. Katodisk korrosion viste sig at være lovende, hvis yderligere optimering af parametrene finder sted, men den mest lovende metode var modifikationen af en kommerciel Pt/C katalysator ved høj temperaturs reduktion af salte af sjældne jordarter. Termodynamikken bag dette system blev undersøgt og det viste sig muligt, at danne de ønskede legeringer fra 500 °C. De mange legeringsfaser, hvis strukturer er tæt relaterede med hinanden og som kan dannes for fasesystemet mellem platin og de sjældne jordarter, komplicerede karakteriseringen af systemet.

En aktiv Pt-Y legering blev syntetiseret efter en optimering af opsætningen til syntesen. Denne udviste en masse aktivitet på $0.41 \pm 0.01\,\mathrm{A\ mg}_{\mathrm{Pt}}^{-1}$ mod $0.27 \pm 0.07\,\mathrm{A\ mg}_{\mathrm{Pt}}^{-1}$ for den kommercielle katalysator. Denne aktivitet er lovende eftersom dette er første gang denne nye gruppe af katalysatorer, bliver syntetiseret med en skalerbar metode. Der skal dog fortsat arbejdes med faserenheden og synteseparametrene for, at kunne udnytte denne gruppe af katalysatorers fulde potentiale.

List of Included Papers

Appended Papers

Paper I

Scalable Synthesis of Carbon Supported Platinum - Rare Earth Alloys for use as Fuel Cell Cathodes
Brian P. Knudsen, Christoffer M. Pedersen, Amado Velázquez-Palenzuela, Leif H. Christensen, Ifan E. L. Stephens, Ib Chorkendorff,
In preparation

Papers Not Appended

Paper II

Benchmarking the Stability of Oxygen Evolution Reaction Catalysts: The Importance of Monitoring Mass Losses
Rasmus Frydendal, Elisa A. Paoli, Brian P. Knudsen, Björn Wickman, Paolo Malacrida, Ifan E.L. Stephens, Ib Chorkendorff
ChemElectroChem, 2014, Volume 1, pages 2075-2081

List of Patents

Patent I

Process For The Preparation of Alloy Nanoparticles Comprising A Noble and A Non-Noble Metal
Ib Chorkendorff,Amado Velazquez-Palenzuela, Ifan E. L. Stephens, Brian P. Knudsen, Christoffer M. Pedersen
Application Filed with the EPO

List of Acronyms

ADT Accelerated Degradation Test

AFC Alkaline Fuel Cell

AR-XPS Angle Resolved X-ray Photoelectron Spectroscopy

BE Backscattered Electron

BEV Battery Electric Vehicle

CE Counter Electrode

CV Cyclic Voltammogram

DFT Density Functional Theory

DMFC Direct Methanol Fuel Cell

DOE Department Of Energy

DTI Danish Technological Institute

ECSA Electrochemical Surface Area

EDS Energy Dispersive Spectroscopy

EM Electron Microscopy

EMT Effective Medium Theory

EPC Energy Per Capita

EROI Energy Returned On Investment (here Energy Invested)

EXAFS Extended X-ray Absorption Fine Structure

FCEV Fuel Cell Electric Vehicle

FEG Field Emission Gun

FFT Fast Fourier Transform

GC Glassy-carbon

GDL Gas Diffusion Layer

GDP Gross Domestic Product

GHG Green House Gasses

HAADF High-angle Annular Dark Field

HDI Human Development Index

HOR Hydrogen Oxidation Reaction

ICE Internal Combustion Engine

IFFT Inverse Fast Fourier Transform

LCA Life-cycle-assessment

MEA Membrane Electrode Assembly

ML Monolayer

NIST National Institute Of Standards And Technology

OCV Open Circuit Potential

ORR Oxygen Reduction Reaction

PEMFC Proton Exchange Membrane Fuel Cell

PGM Platinum Group Metal

PSD Particle Size Distribution

PVP Polyvinylpyrrolidone

RDE Rotating Disc Electrode

RE Rare Earth

REF Reference Electrode

RHE Reversible Hydrogen Electrode

SAXS Small Angle X-ray Scattering

SE Secondary Electron

SEM Scanning Electron Microscopy

SHE Standard Hydrogen Electrode

SOFC Solid Oxide Fuel Cell

STEM Scanning Transmission Electron Microscopy

TEM Transmission Electron Microscopy

THF Tetrahydrofuran

TKK Tanaka Kikinzoku Kogyo

toe Tons Oil Equivalent

UN United Nations

UNFCCC United Nations Framework Convention On Climate Change

WE Working Electrode

WTW Well-to-wheel

XPS X-ray Photoelectron Spectroscopy

XRD X-ray Diffraction

XRF X-ray Fluorescence Spectroscopy

List of Figures

List of Tables

Contents

CHAPTER 1

Introduction

The work presented in this PhD thesis, encompasses a very small fraction of a future based on renewable energy. It revolves around the synthesis and optimisation of a new class of electrocatalysts for the oxygen reduction reaction (ORR). These are candidates for the catalyst material in fuel cell electric vehilces (FCEVs), utilising renewable energy stored in chemical form as hydrogen for vehicular transportation. For those experienced in the field, jumping directly into the details of the work would be tempting, however, for the casual readers an introduction is in order. This chapter will serve to motivate and introduce the work carried out.

1.1 A Change of Climate in the Energy Landscape

Energy consumption is on the rise globally and has been ever since the industrialization. In more recent years, since 1971, primary energy consumption has risen by 150 %.[1,2] This surge in energy use has generally been driving overall human development. This development is visualized in figure 1.1 and 1.2 showing how the human development index (HDI) correlates to the energy per capita (EPC) in ton oil equivalent (toe) for the individual countries for 1985 and 2010 respectively.[3] The HDI is a measure of overall achievements in key dimensions of human development: Long and healthy life, knowledge and standard of living.[4]

Looking at figure 1.1 of the HDI v EPC in 1985, it is clear that the western countries were doing well, high on the HDI at the cost of high energy use, as can be seen in the EPC. The United States scores very high on the HDI while also paying for it with high EPC. China and India are on the other hand placed directly opposite, with a low development status, HDI, and low EPC. European countries such as Denmark and Germany are high on the HDI, similar to the United States, while at the same time having close to half the energy expenditure per capita. In other words, the European countries are generating societal advancement at a lower energy cost. This can to a large extent be attributed to the fact that countries, such as the United States, that have low energy prices use more. These low prices often come from a combination of being net exporter of energy while at the same time not limiting energy use through taxes and regulations. The western countries also have higher gross domestic product (GDP) per capita signifying higher growth and productivity.

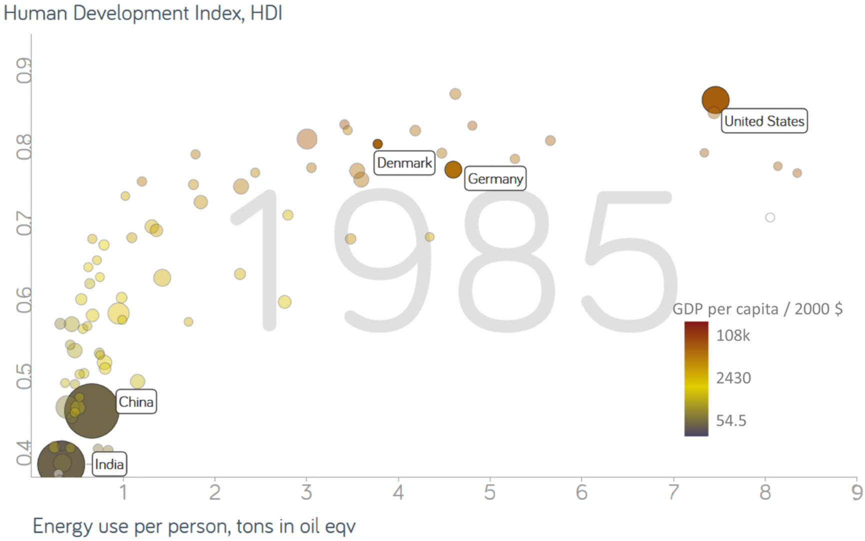

Figure 1.1: HDI as function of EPC for 1985. Color of the spheres indicates GDP per capita, with blue and red signifying low to high respectively. The size indicates the population size of the country. Generated with Gapminder tools[3].

Fast forward to 2010 and some parts of the world have changed significantly. China and India have experienced significant economic growth as seen in their respective GDPs. This growth has driven the increase seen in both HDI and EPC. Especially China is experiencing astronomical growth, even breaking double digits for the growthrate in 2010.[5] At the same time western countries have seen slight increase in HDI while at the same time slightly lowering the EPC. This is a general trend seen for developed countries. Through technological advancements, efficiency is increased for areas such as electricity production, industrial production and residential use. From the figures it is also worth noting that only countries with high GDP and EPC seem to place well on the HDI. With countries like India and China seeking to improve their development status, thereby increasing their HDI placement, it can be projected that their EPC will increase significantly. Compounding the effect of improved living standard is the population growth. As of 2015 the world was inhabited by roughly 7.35 billion people, by 2100 the United Nations (UN) projects that the world population will hit 11.2 billion. With most of the population growth occuring in developing areas such as India and Africa.[6] Using the energy mix of today, namely 86 % fossil fuels, it will not be possible to supply the energy needed, both resource-wise and economically.[1,7,8] To overcome this, more sustainable energy, such as wind, solar, hydro and nuclear is being added to the grid. This will also increase energy security as sustainable energy is not tied directly to repositories confined to individual countries, such as fossil fuels are. With recent developments these energy sources are also able to compete with traditional fossil fuels when it comes to energy returned on (energy) invested (EROI).[9,10] Furthermore the renewables, wind, solar and hydro account for the largest growth in energy production in recent years.[1,11–13]

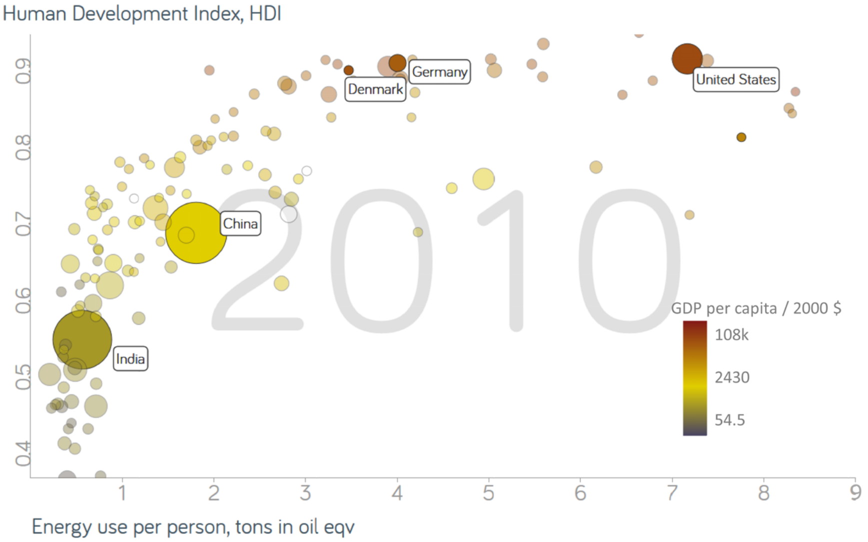

Figure 1.2: HDI as function of EPC for 2010. Color of the spheres indicates GDP per capita, with blue and red signifying low to high respectively. The size indicates the population size of the country. Generated with Gapminder tools[3].

1.2 The Ugly Shadow of CO_2

Economic concerns, energy security and resource limitations are not the only reasons why more renewable energy is being implemented at a higher rate than before. The adverse effects of anthropogenic green house gasses (GHG's) associated with energy production from fossil fuels, have lead most of the world to combat emissions. Especially CO_2 is being singled out as it constitutes 60 % of global emissions.[2] One study from 2009 showed that it is not only the magnitude of changes in the CO_2 levels that causes problems, the irriversibilities of the levels are what will haunt society for the coming 40 generations or more.[14] Already In 1992 the UN set up the United Nations Framework Convention on Climate Change (UNFCCC) to mitigate the threats of climate. Through this framework it arranges meetings and conferences on the topic of GHG emissions. Some of the outcome has been trading systems for CO_2 emissions and in December 2015 it drafted its first binding agreement for reductions in emissions of GHGs.[12,15,16] This framework is also part of the explanation for the reduced EPC of the western countries. By increasing efficiency of the energy use, the anthropogenic GHG footprint can be lowered without sacrificing societal development. This is feasible in established economies and highly developed countries like Denmark, Germany and the United States and is done by switching fuel mixes to be less carbon intensive, advancing technology and by utilising renewable sources to a higher extent. The same does not seem to happen in developing countries, where the growth is directly coupled to the emissions per capita.

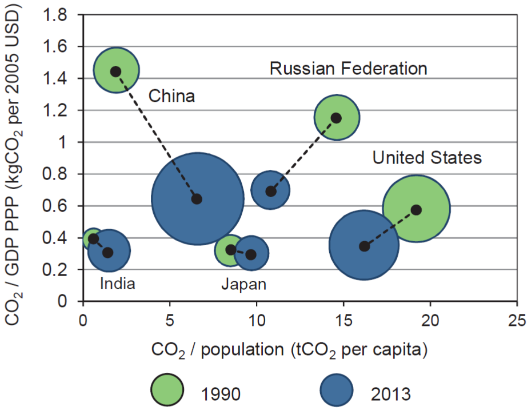

Figure 1.3: CO_2 emission per GDP as function of CO_2 emission per capita for 1990(green) and 2013(blue). The size of the speheres indicate the total CO_2 emissions in the respective year. Reproduced from [2].

This can be seen in figure 1.3, where the CO_2 emission per GDP is plotted against CO_2 emission per capita. The size of the spheres indicate the total emission of CO_2 for that year respectively. The countries experiencing high growth are growing in both total and per capita emissions. At the same time, the established economies have reduced their emissions per capita while only increasing overall emissions slightly. An interesting observation is the tendency to converge on a per capita emission. If it is assumed that in the future this convergence level would fall around 10 tCO_2 per capita, that level would be more than twice that of the world in 2013, where it was just below five tCO_2 per capita.[2] With the expected population growth in the near future the consequences for the climate would be incomprehensible and devastating. This, however, does not have to happen as indicators are already now showing changes. In 2014, for the first time in 40 years, the year-on-year increase in energy-related CO_2 emissions, on a global scale, were insignificant. At the same time, global growth sat around 3 % signifying a decoupling of growth and emissions.[12] Diving into the details, stationary use of energy, electricity generation, heating and industrial processes, are shifting towards renewable sources, however, one area is more difficult; Transportation. It constitutes a quarter of all emissions and road transportation constitutes, by far the largest, growing from 60 % of the total transportation emissions in 1970 to 72 % in 2010. At the same time, the energy intensity for transportation follows that seen for primary energy, with developing and emerging countries having lower per capita use, while also experiencing higher growth rates in use.[2,17,18]

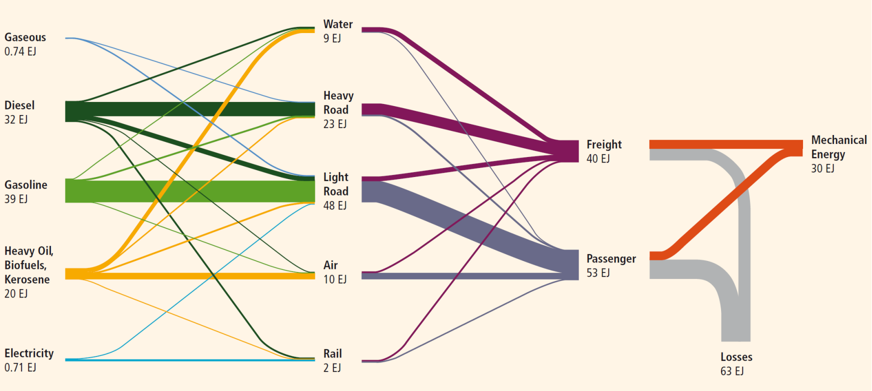

Figure 1.4: The total flow of energy from source to transport sector. As seen, fossil fuels dominate the energy use for transportation, with road transport constituting the majority. Reproduced from [18].

Figure 1.4 shows the distribution of energy flow to the different transport sectors and their contribution to either passenger or freight transport. The width of the individual lines indicate the magnitude of energy flow from source to sector to type. It also shows the energy efficiency on the far right, with an overall

efficiency of 32 %. To mitigate emissions, each sector must work to improve efficiency, utilizing all possible avenues for improvements such as; aerodynamics, weight reduction, fuel carbon intensities, etc.
While economics and supply security drives the electricity, heat and industry supply chain. The same does not hold for the transportation sector. Freight transport is governed by these factors, however, the passenger road transportation suffers from the habits, percieved benefits and convenience of fossil fuels. Thus far, the route taken to lower the emissions of road transport has been through legislation, mandating lower emissions and tax rebates afforded to both industry and consumers for choosing low emission vehicles. These measures, while seemingly providing economic incentive to lower emissions have proved ineffective. This is in part due to the unrealistic laboratory test-cycles used to certify vehicle emissions. Manufacturers have steered development of technology towards optimizing their vehicles for these test cycles and not towards real world conditions, rendering the emissions 38 % higher than those achieved during certification testing.[19,20] In long term the only viable option for reaching goals set for the transport sector is switching to electrified propulsion, by battery electric vehicles (BEVs) and fuel cell electric vehicles (FCEVs).

1.3 Re-envisioning Transportation

As mentioned above only two technologies hold the potential to truly mitigate emissions; BEVs and FCEVs. Both of these are purely electric vehicles with zero tailpipe emissions. Often when the discussion falls on the technologies that should supersede the internal combustion engines (ICEs) for transportation, it devolves into a fight between the two electric camps. This is not limited to the public debate, since the automotive industry and scientific community also resort to "picking a side". The reasoning for the latter parties' focus on a singular technology and borderline bashing of the other, can be found in the limited funding for the field and the battle for public favour in the initial market. This internal power struggle is counter productive, as the two technologies actually complement each other in the transportation sector. As both technologies are purely electrical, it is pivotal that renewable energy sources supply the electricity. Without a renewable energy source, their potential diminishes dramatically, with FCEVs becoming as emission heavy as ICEs when comparing well-to-wheel (WTW) emissions and life-cycle-assessments (LCA). From a pure emissions point of view BEVs will perform better than FCEVs when given the same electricity production conditions.[21,22]

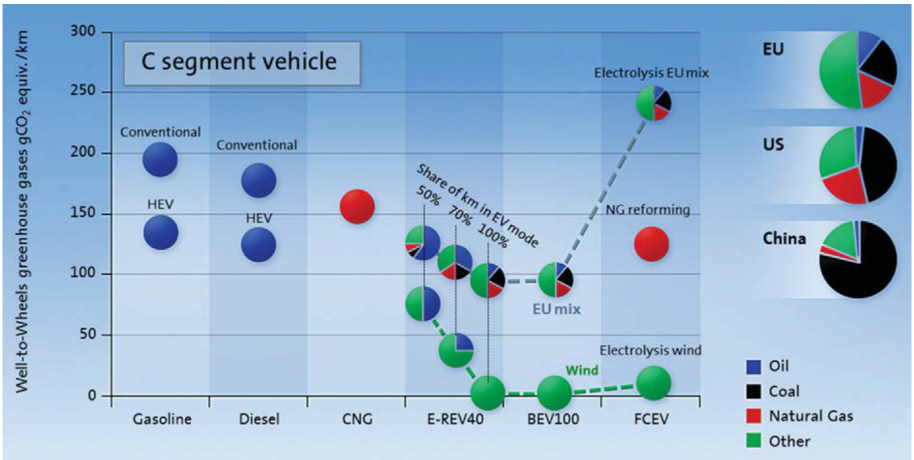

Figure 1.5: The projected emissions in gCO_2 eqiuv./km for ICE vehicles, with and without batteries BEVs on the Eroupean electricity mix and FCEVs on European mix and natural gas reformate. Reproduced from [21]

Had this been the only condition for choosing the next propulsion system, BEVs would be crowned the winners, however, there are many more parameters that need to be taken into account. Some of these are close to impossible to change, in particular the apparent needs and wishes of the end user. While actual driving patterns for the daily travel needs fall below approximately 160 km, several studies report drivers view that approximately 250 km to 346 km would be an acceptable range for vehicles.[23,24] Here public opinion would prefer the characteristics of the FCEV, as for this range it is both cheaper and faster to refuel/recharge. Even considering the most optimistic improvements in cost per kilo-Watt-hour, in this driving range the FCEVs would be the cheaper system, while also being the lighter system. Only BEVs for the luxury and sports segments would be feasible due to their higher pricing.[25] This is the general story, for long ranges the FCEV is projected to win over the BEV on weight, cost and refuelling time, making them the ideal choice for commuters with long travel distances and freight services, where cost and weight of the needed battery capacity would constrain the haul capacity significantly. For city commuters, driving the BEV offers the most desirable characteristics, with lower price and weight. The medium range market would be shared between the two technologies.
BEVs are already widely available, from several manufacturers, in all of the market segments for passenger vehicles. FCEVs have not matured as rapidly as BEVs, as the battery technology development has benefited from its widespread use in consumer electronics. Conversely, FCEVs are only in their infancy, with only the Toyota Mirai being produced at volume, however, limited to a total of 700 in 2015.[25] The United States Department of Energy (DOE) estimates the main cost of the fuel cell stack to be a even split between the different compo-

nents, at the production level of the Toyota Mirai in 2015. Estimating the cost for a production of 500,000 systems per year shifts the main contribution for the fuel cell stack to the catalyst, contributing roughly a quarter of the total system cost.[26]

In order to drive the FCEV forward, cost and efficiency must be improved, most components in the system becomes cheaper with large scale production, however, the amount of catalyst material needed does not. Improving the catalyst material can increase efficiency and enable material and price reductions.[27] The work in this thesis addresses this very problem by investigating a new class of catalysts designed for high activity, driving material need down.

1.4 Fundamentals of Fuel Cells

The previous section compared BEVs and FCEVs without explaining the working principles of either. As this thesis examines electrocatalysts that can be used in FCEVs, the fuel cell as a concept and the type that is utilised for FCEVs will be introduced.

The fuel cell is no new invention and has been known since 1839, where Sir William Grove discovered it. Since then a plethora of types have been developed: Proton exchange membrane fuel cells (PEMFCs), direct methanol fuel cells (DMFCs), alkaline fuel cells (AFCs), solid oxide fuel cells (SOFCs), etc. They convert energy stored in chemical bonds into electricity without having to drive any mechanical components. It resembles a battery in the sense that the chemical reaction is split into an oxidation reaction on the anode and a reduction reaction on the cathode, with a membrane separating the two reactions. A substantial difference lies in the handling of the stored chemical energy. In the battery it is sealed internally and can only be regenerated by driving the opposite reaction, by supplying energy to the system, assuming it is a rechargeable battery. For the fuel cell the it is stored outside the system and in the form of a liquid, gas or solid, that can be refilled easily similar to an ICE. For commercialisation of FCEVs compressed hydrogen is the fuel of choice as this is the simplest molecule to store energy in.

1.4.1 Proton Exchange Membrane Fuel Cell

For automotive usage the PEMFC class holds many advantages that makes it the technology of choice. It has an operating temperature range overlapping with that of ICEs, high conductivity of the membrane as well as an overall high electrical efficiency.[21,28,29] A sketch of a PEMFC can be seen in figure 1.6, with the individual components marked. In the center there is a proton exchange membrane that separates the two half cell reactions, it only allows for proton transport and it consists of a sulphonated fluoro-polymer e.g. Nafion (®Dupont) that becomes proton conducting as it is humidified.

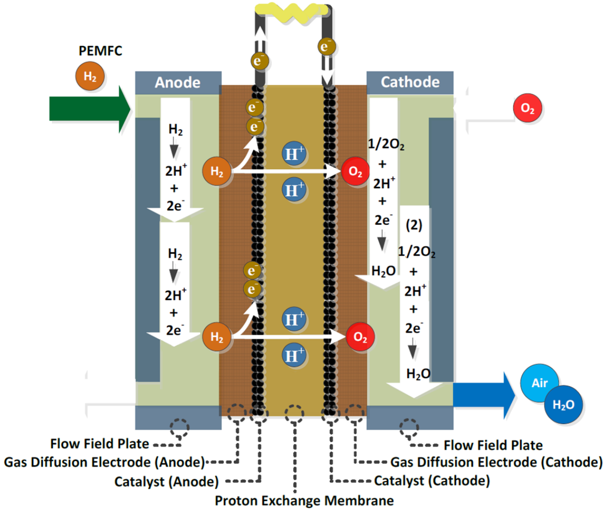

Figure 1.6: Sketch of a PEMFC fuel cell. The membrane only allows protons to pass through, forcing electrons from the oxidation reaction through the external circuit. Adapted from Yun-Sheng Ye *et al.*[30].

The conductivity also increases with temperature, though humidity is dominating factor.[31] As only protons can pass through, the electrons released from the oxidation reaction on the anode pass through the external circuit and is used to drive it. the electrodes are pressed on the membrane from either side and are comprised of a catalyst layer and a gas diffusion layer (GDL). The GDLs act as support for the catalyst as well as ensuring good electrical contact and distribution of reactants and products. The combination of GDLs, catalyst layers and membrane is known as the membrane electrode assembly (MEA). In it self the MEA is a working fuel cell, however, in order to get the desired power from a fuel cell, these MEAs are stacked together with field flow plates that acts as channels for the gaseous reactants and products.[28,31] Below is the two half cell reactions and the overall reaction, when using pure H_2 as fuel. On the anode, eq. 1.1, the H_2 is oxidised supplying protons that go through the membrane and electrons that are run through the external circuit. This reaction is called the hydrogen oxidation reaction (HOR). On the cathode the protons react with the supplied oxygen and the electrons from the circuit, eq. 1.2, resulting in the oxygen reduction reaction, (ORR) forming water as the only product.

$$2H_2 \rightarrow 4H^+ + 4e^- \quad (\textbf{Anode}) \tag{1.1}$$

$$O_2 + 4H^+ + 4e^- \rightarrow 2H_2O \quad (\textbf{Cathode}) \tag{1.2}$$

$$2H_2 + O_2 \rightarrow 2H_2O \quad (\textbf{Overall}) \tag{1.3}$$

Up until recently the only viable material for the catalysts was pure Pt as the environment in a PEMFC is very corrosive. This is due to the acidic nature of the proton exchange membrane and the working potential that promotes the dissolution of most metals[32]. With the recent launch of the Toyota Mirai a new catalyst has seen commercial use; an improved alloy of Pt and Co, with close to double the activity per gram of Pt, that in part has made it possible to actually bring the fuel cell to a market that is not a niche market.[25,27] With Pt as the catalyst, the amount needed for a single car would have been around 50 g of Pt or ten times more than what is used in a regular catalytic converter for ICEs. This is assuming a car with a 100 kW output and state-of-the-art Pt based fuel cells, with a platinum loading of $0.5\,\mathrm{mg_{Pt}/kW}$.[25,33] The price for a single car at this usage would be too high, at roughly 1600 $ per-car in raw metal price, without processing. The potential for mass production is also non existing, as even totalling a production of 500.000 FCEVs would use a quarter of all the Pt used for catalytic converters. That might not seem too horrific, however, the car production totals some 68 million cars per year.[34,35]

1.4.2 Fuel Cell Thermodynamics

The theoretically attainable voltage from a fuel cell can be calculated from equation 1.4, the thermodynamic open circuit voltage (OCV) of a galvanic cell.[36]

$$U^\circ(T) = -\frac{\Delta G(T)}{zF} \tag{1.4}$$

U° is the standard potential, $\Delta G(T)$ is the change in Gibbs free energy for the reaction which depends on the temperature, z is the number of electrons involved in the reaction and F is Faradays constant. For the overall reaction in eq. 1.3, the potential at 25 °C is 1.23 V.[28] When drawing a current from the cell several loss mechanisms play a role and have to be considered. Equation 1.5 summarises the main factors contributing to the energy loss.

$$U_{\mathrm{cell}}(I,T) = U_{\mathrm{rev}}(T) - J \cdot R_{\mathrm{Ohmic}}(J,T) - \eta_{\mathrm{ORR}}(J,T) - \eta_{\mathrm{t}}(J,T) \tag{1.5}$$

Here J denotes the current density of the cell, with $R_{\mathrm{Ohmic}}(J,T)$ describing the ohmic resistance of the cell as a function of current density and temperature. The loss at the cathode and from mass transport are denoted $\eta_{\mathrm{ORR}}(J,T)$ and $\eta_{\mathrm{t}}(J,T)$ respectively and are also functions of current density and temperature.

$U_{\text{rev}}(T)$ is the reversible potential of the fuel cell, taking into account the partial pressures of reactants and products. It is calculated using the Nernst equation (1.6), where R is the gas constant and P_X is the partial pressure of the reactants and products. Losses from the anode have been neglected as they are small in comparison to the rest when utilising Pt as HOR catalyst.[33,37,38]

$$U_{\text{rev}} = -\frac{\Delta G(T)}{zF} + \frac{RT}{zF}\ln\left(\frac{P_{\text{H}_2}\sqrt{P_{\text{O}_2}}}{P_{\text{H}_2 O}}\right) \tag{1.6}$$

Figure 1.7 shows a deconvoluted polarisation curve for a fuel cell MEA in operation at 80 °C and utilizing pure Pt, as reported by Gasteiger *et al.*[33] It is clear than the main losses in the fuel cell can be attributed to the ORR, and in turn the slow kinetics of this reaction. To improve the efficiency, new catalyst materials are needed that show improved kinetics when compared to pure Pt. This will be discussed further in chapter 2.

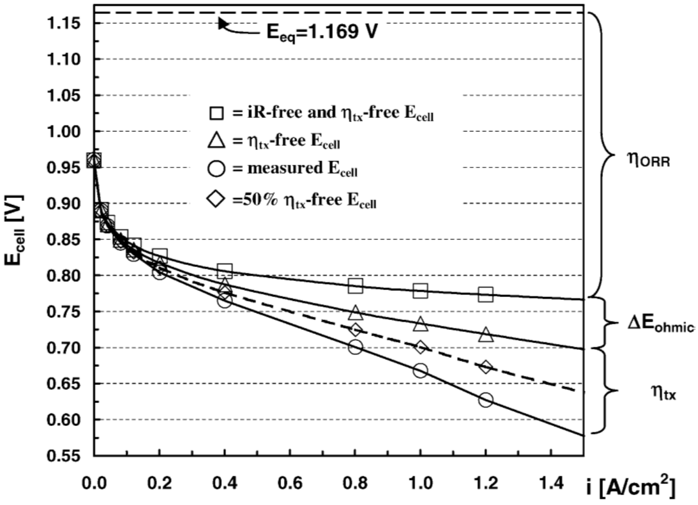

Figure 1.7: Polarisation curve of a PEMFC fuel cell based on pure Pt, in operation at 80 °C. The major loss component is the overpotential for ORR (squares). Adapted from Gasteiger *et al.*[28].

1.5 Catalysts

As mentioned above, better catalysts are needed in order to improve the fuel cell efficiency and moreover the price for fuel cell stack production. This can be done effectively by improving the activity of the catalyst that is used. This section serves to introduce the catalyst and how they work. It will be a stepping stone for the next chapter that will introduce the concepts needed for improving the activity.

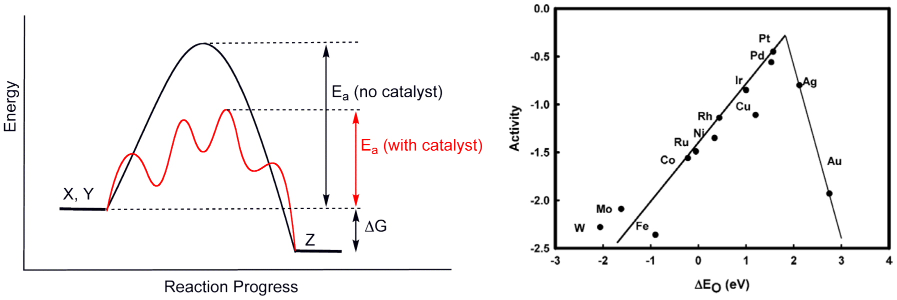

(a) Reproduced from [39]

(b) Reproduced from Nørskov *et al.*[40]

Figure 1.8: **(a)** The concept of catalysis. The reaction from X and Y to Z proceeds at a higher rate on the system with a catalyst (red line) as it has an overall lower barrier for the reaction. **(b)** Theoretical investigation of the correlation between ORR activity and oxygen binding energies.

In heterogeneous catalysis the intermediate states are adsorbed species on the surface of the catalyst material. As catalysis is directly coupled to the surface area, this needs to be maximised in order to fully utilize the often expensive material. To do this, ever smaller nanoparticles are formed that increase the surface to bulk ratio dramatically, however, with this decrease in size the ideality of the structure breaks down and defects become more and more relevant, and in turn the activity becomes much more difficult to model and predict.[37,41] Figure 1.8a shows a schematic overview of a chemical reaction proceeding with, and without a catalyst. Overall the reaction can proceed as the energy of product, Z, is lower that that of the two reactants, X and Y, combined. Assuming the same environmental conditions for the two systems, the system with the catalyst (red curve) will run at a higher reaction rate as it provides intermediate states with lower barriers or activation energies. These states have a longer lifetime than the transition state of the system without catalyst (black curve) and overall lower barriers or activation energies, symbolised by the local minimas.[39,42] This means that utilising a suitable catalyst can increase the reaction rate or lower the cost of running the reaction by easing the conditions needed, be it temperature, pressure, potential, etc. The optimal catalyst will be one that allows reactants, intermediates and products to interact "just right" as formulated by Nobel Laurate Paul Sabatier.[43] If the catalyst and reactants interact too weakly, the intermediates will not form and the reaction rate will be slow. If it interacts too strongly, the product will not be able to leave the catalyst again blocking the catalyst for further reactions and lowering the reaction rate. This balance of components can be seen in figure 1.8b. Here Nørskov *et al.* used calculations with the binding energy of oxygen to a metal surface as a descriptor to show this balance of the activity for ORR.[40] The calculations show the same trend as experiments, with Pt being the most active metal for the reaction. The coupling between descriptors and activity is a cornerstone that allows for rational design of new catalyst materials.

1.6 Thesis outline

The overall goal of this thesis is to explore methods for synthesising platinum rare earth alloys for use as electrocatalysts in fuel cells. To that end chapter 2 introduces the relevant parts of the field of electrocatalysis for the oxygen reduction reaction. Chapter 3 will in a brief way introduce the techniques used to analyse and confirm the formation of alloys. Chapter 4 introduces the main methods studied for synthesising the platinum rare earth alloys. It also characterises the produced catalysts and goes over the thermodynamics of reducing precursors for the rare earths. Chapter 5 introduces the initial synthesis of carbon supported platinum and yttrium alloys and characterises the catalyst. Chapter 6 expands upon the elements that are used for the synthesis to also include Terbium and Gadolinium. The complex structure of the alloys is also touched upon and the initial electrocatalytic activity of the alloys is also assessed. The main conclusions and an outlook is presented in chapter 7 that also closes out the main part of the thesis.

Chapter 2

Electrocatalysts for Oxygen Reduction

This chapter will dive into the kinetics of the ORR and what can be done to optimise the catalyst of choice Pt. A brief overview of the literature will be presented, for a more comprehensive view I would point the reader towards the many great overview articles on the advances made in the field [25,33,37,44–47]. The chapter will also introduce the alloys of interest in this thesis work, namely alloys of Pt and alkali earth, rare earth and rare earth like early transition metals, with a focus on the latter two. These will from here on be referred to as REs for the whole group.

2.1 ORR Kinetics

The ORR follows from equation 2.1, below it, in equations 2.2-2.5 are the four steps in the associative pathway, with the three intermediates; *O, *OH and *OOH. Here (*) denotes the adsorbed species with (g) and (l) denoting gas phase and liquid phase respectively. There is another pathway known as the dissociative, where oxygen is dissociated on the surface before it is protonated, however, at the relevant potentials for fuel cell operation the associative mechanism determines the activity.[40,48,49]

$$O_2\,(g) + 4H^+ + 4e^- \leftrightarrow 2H_2O(l) \tag{2.1}$$

$$O_2\,(g) + H^+ + e^- \leftrightarrow {}^*OOH \tag{2.2}$$

$${}^*OOH + H^+ + e^- \leftrightarrow {}^*O + H_2O(l) \tag{2.3}$$

$${}^*O + H^+ + e^- \leftrightarrow {}^*OH \tag{2.4}$$

$${}^*OH + H^+ + e^- \leftrightarrow H_2O(l) \tag{2.5}$$

The reaction has been studied in great detail over the last decade, with theoretical work done by the groups of Nørskov and Rossmeisl.[40,48,50,51] For the ORR on a Pt(111) surface, the reaction is visualised in figure 2.1, as calculated by Anders Jepsen.[52] The idealised case show the free energy of the different intermediates at OCV conditions (blue lines) and at 0.75 V (black lines) where all reaction steps are downhill in free energy and the reaction can run at an appreciable rate. For this it is assumed that the barriers for proton transfer are comparatively small. For OCV it is clear that the ideal catalyst binds *OOH too strong, while it binds *O and *OH too weak compared to Pt. However, as all intermediates bind through oxygen, their binding energy scales with each other, a trend that holds for many systems and adsorbates.[53,54] This scaling relation sets a limit as to what is possible to do, and the optimal catalyst for ORR will be the one that binds *OH 0.1 eV weaker than pure Pt.[49,55]

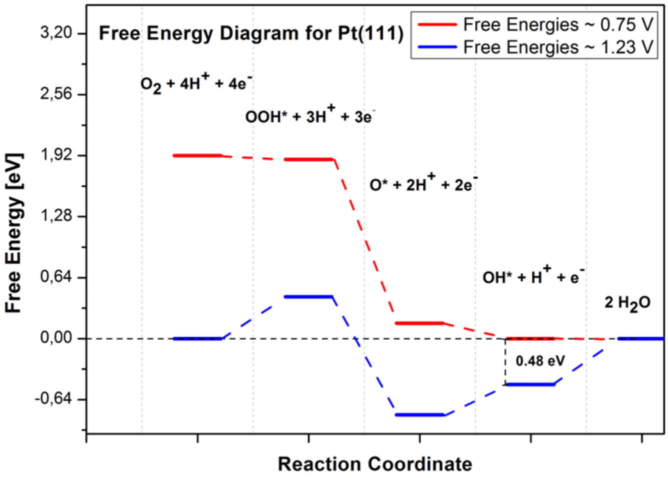

Figure 2.1: Free energy for Pt(111) at the potential of 1.23 V (blue) and at 0.75 V where all the reaction steps are downhill in free energy (red). Original work by Rossmeisl *et al.* [49].

In order to improve the Pt as a catalyst, the binding energy of *OH should be weakened. To do this a second element is often introduced through alloying. It is generally accepted that in doing so there are two different mechanisms that alter the binding energies: Strain effects and the ligand effect. There is a third way to alter the activity of a catalyst and that is the bifunctional catalyst, where instead of modifying the original metal with the solute metal, this second metal acts a separate site opening a new pathway for the reaction to follow.[56,57] For the ORR only the former two mechanisms have been experimentally verified, as such only these will be introduced in greater detail in section 2.1.1 and section 2.1.2. The two mechanisms can be explained by the d-band model that describes how the position of the d-band, in transition metals, directly influence adsorbates binding energies. Shifting the d-band center down will weaken the adsorbates interaction with the surface, while an upwards shift will increase the interaction.[42,58–61]

2.1.1 Ligand Effects

The weakening of the binding energies of adsorbates on the surface of platinum can be achieved through alloying. In doing so the electronic structure of the Pt atoms will change. This changes the center of the d-band and thereby alters the binding energy of the adsorbates. This has both been modelled theoretically by density functional theory (DFT) and experimentally using Ni annealed into the surface of a Pt(111) crystal and examining the *H binding energy.[62,63] In another study by Stephens *et al.*, the activity for ORR of a Pt(111) crystal was tuned by controlling the amount of Cu in the first subsurface layer.[55] As the solute metal in these studies only were introduced is small quantities, the lattice parameter of the catalyst did not change, thereby only probing the effect of the changed electronic structure. Depending on the solute metal the binding of the adsorbates can be weakened or strengthened.

2.1.2 Strain Effects

The other mechanism that can alter adsorption properties is strain. Removing a metal from its equilibrium lattice constant will change the interaction with adsorbates.[64] For metals where the d-band is more than half filled, compressive strain increases the overlap between the atoms d-orbitals, this in turn causes a broadening of the d-band as the d-orbitals become more delocalised. The d-band center will move down as the filling degree cannot change, weakening the interaction with adsorbates. To decrease the *OH binding energy on Pt by the desired 0.1 eV for the ORR, a compressive strain of $2\,\% - 3\,\%$ would suffice in the absence of any other effects.[37,64,65]

2.2 Advances in ORR Catalysis

With the two primary mechanisms used to understand and design the catalyst of interest described, the recent developments will be presented.
The requirements of new catalysts for the ORR are currently set at reaching a Pt specific power density of $0.1\,\mathrm{g_{Pt}\,kW^{-1}}$. In order to meet this, the mass activity of platinum should be enhanced by a factor of four to 10, translating to activity enhancements in current densities from $0.4\,\mathrm{A\,mg_{Pt}}^{-1}$ to $1.0\,\mathrm{A\,mg_{Pt}}^{-1}$ in MEA measurements. This should be while also improving the stability under operating conditions, all while the production of the catalyst should be scalable, allowing for mass production.[66–68]

2.2.1 Dispersion of Pt

While not an intrinsic change in the catalyst, creating highly dispersed nanoparticles on high surface area support has long been the standard for improving the mass activity of Pt. As mentioned in Chapter 1 decreasing the particle size increases the utilisation of the catalyst mass. However, as the size decreases the increasing presence of undercoordinated sites will hinder the ORR, as interaction with adsorbates increases.[69,70] This trade off between surface area and active sites was examined for a model system mass selected nanoparticles on GC electrodes by Perez-Alonso *et al.*Here the optimal size was 3 nm, showing $1\,\mathrm{A\,mg_{Pt}}^{-1}$.[71] The particle size effect has also been seen for commercial Pt catalysts with Nesselberger *et al.* reporting an increase in mass activity with Pt dispersion. However specific activity remained unchanged for $1-5$ nm particles.[72] One parameter not captured by this study was the effect of loading and therefore interparticle distance. For a model system of magnetron sputtered nanoparticles of Pt progressing from low loading, highly dispersed, Pt nanoparticles of $2-3$ nm to agglomerated and extended surfaces of high loading, Schmidt and co-workers reported that the specific activity increased as the ECSA decreased.[73] This change was correlated to an decrease in adsorption energy for oxygenated species at low ECSA and the same trend has recently been shown for thermally reduced carbon supported Pt catalysts with loadings from $20-80$ wt% by the same group.[74] An explanation for the effect of interparticle distance was presented by Arenz and co-workers, that through tailoring of the interparticle distance of mass selected Pt nanoparticles achieved a six-fold increase in mass activity over commercial Pt/C.[75] The authors show how the electric potential in electrochemical double layer at low interparticle distances resemble that of the extended surfaces. This reduces the adsorption strength of oxygenated species, leading to the increased specific activity. Another way of increasing the utilisation of Pt is through the use of unsupported aerogels, as those presented by Schmidt and co-workers.[76,77] These show very high specific activities and similar dispersion as the supported catalysts. They consist of elaborate three-dimensional network of nanowires. Attaining the surface area of the supported catalyst without the support has the benefit that degradation through support corrosion is avoided.[78]

So far state-of-the-art supported Pt nanoparticles have reached ~ 0.18 A/$\mathrm{mg_{Pt}}$ in MEA tests, while lab-scale rotating disc electrode (RDE) measurements show ~ 0.55 A/$\mathrm{mg_{Pt}}$.[25,72] This highlights that, while lab-scale RDE measurements can be used to gauge relative activity between catalysts, only MEA test can verify the potential of a catalyst.

2.2.2 Alloying

As mentioned alloying with other elements will induce strain and ligand effects, modifying the interaction with adsorbates. Many alloys between Pt and late transition metals are known for improving the catalytic activity. Bulk crystalline samples of Pt_3M (M = Ti, V, Fe, Co and Ni), all show higher activity than Pt.[79–81] Stamenkovic *et al.* showed that the active phase of most alloys was a pure, slightly roughened, Pt overlayer of 1-2 nm on top of the bulk alloy. This pure Pt surface forms as none of the alloying metals are stable in acidic environment[32] and has been coined as the "Pt-skeleton" surface. If the surface is annealed in vacuum prior to immersion into electrolyte, a "Pt-skin" surface is formed that typically only measures a single monolayer and that is stable under electrolyte exposure.[81–83] This surface of Pt help stabilize the bulk structure by protecting the sub surface alloy from further oxidation.

Figure 2.2 shows the measured ORR activity of bulk alloys related to their computationally determined binding energy of *OH. Overlayed with the data is the computational volcano with the calculated activity enhancement compared to pure Pt. For these bulk systems, none have shown higher activity than the $Pt_3Ni(111)$ surface.[84] As mentioned earlier, translating activities from well defined bulk systems to the active nanoparticle catalyst is very difficult as the idealised surface breaks down. As such, most of the these alloys only show two to four times the specific activity of similar Pt nanoparticles.[85,86] To increase this several groups have worked on shape controlled nanoparticles, allowing the particles to retain many of the high activity (111) facets.[85,87–92] Stamenkovic *et al.* have even synthesised elaborate three-dimensional PtNi nanoframes eliminating the inaccessible core of the particles.[92] These types of particles have only been produced for lab scale and are yet to be tested in MEAs. Furthermore the labourious synthesis limits the scalability of the process. A different group of alloys is further along; dealloyed nanoparticles. Pioneered by Strasser *et al.*, these alloys start with a stoichiometry of PtM_x ($x \geq 1$ and M=Cu, Ni, Co). In the final step of the preparation process the catalyst is exposed to an acidic environment. The over representation of 3d metal causes excessive leaching forming the active catalyst that has a thick Pt overlayer in the form of the skeleton structure.[93–99]

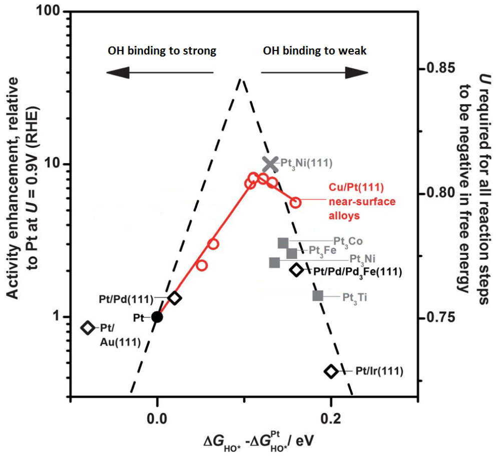

Figure 2.2: Experimental activity enhancement, compared too bulk polycrystalline Pt, for different Pt based systems. The red circles are the Cu modified Pt(111) system from [100]. Right axis shows the computated potential where all reaction steps are downhill in free energy. Adapted from Stephens *et al.* [37].

Figure 2.3 shows the difference between electrochemical and chemical dealloying procedure. While electrochemical dealloying produces a uniform Pt rich overlayer, the chemical dealloying leaves a spongy particle with no ordered structure visible. Both structures are more active that pure Pt with the electrochemically dealloyed structure having the highest specific activity and the chemically dealloyed having the highest Pt mass activity due to increase in surface area from the porosity [101].

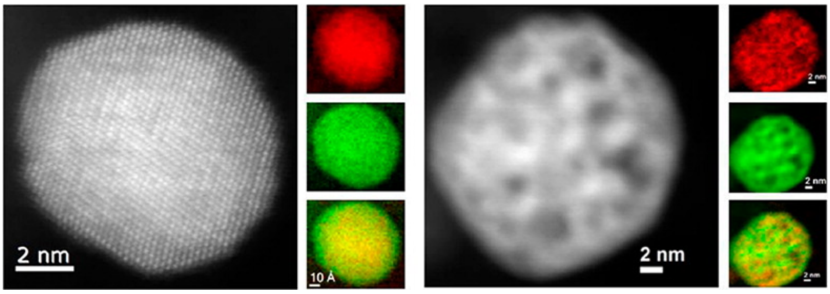

Figure 2.3: STEM images of dealloyed $PtCu_3$ particles after either electrochemical (left) or chemical (right) dealloying. The color maps indicate the presence of Pt(green) and Cu (red) mapped by EELS. Adapted from Wang *et al.*[101].

While these dealloyed structures have proven very active for ORR they have suffered from excessive activity loss when tested in both laboratories and MEAs as the leaching contiues.[102,103] Recently the groups of Shao-Horn and Strasser, together with General Motors showed record high activity for dealloyed $PtNi_3$ alloys in MEA tests. The activity is above the DOE target for activity (0.4 A $\mathrm{mg_{Pt}}^{-1}$) and retains the activity after stability measurements.[99] The improvement in stability witnessed in these results can in part be explained by the annealing procedure that the catalyst experiences as a final step; annealing. In a study by Makharia *et al.* on the methodologies of evaluating PEMFC activity, it was shown that annealing alloy nanoparticles help them retain their surface area, see figure 2.4, the same happens for pure Pt nanoparticles. The annealing process allows the nanoparticles to sinter, moving the particle size distribution (PSD) up, lowering the difference in surface tension that drives sintering. At the same time the particles are allowed to restructure, removing many of the undercoordinated sites that are points of dissolution during operation.[104] These results are very promising, however, they are based on accelerated degradation tests and real performance cannot be assessed before true long term testing is carried out.[105,106]

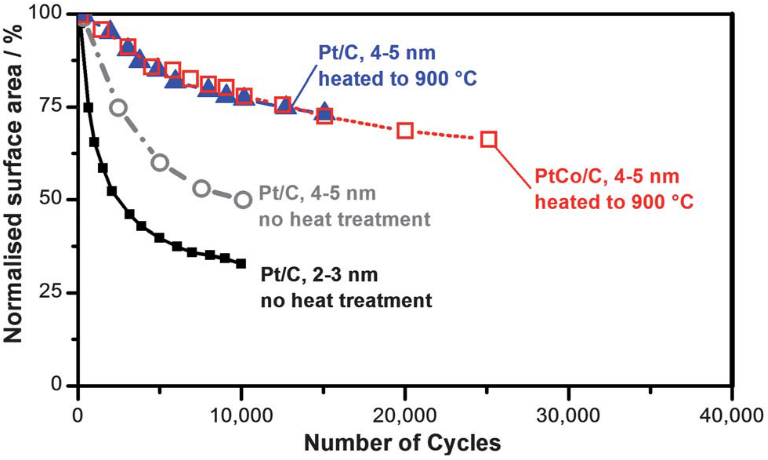

Figure 2.4: Polarisation curve of four different PEMFCs; Pt/C without heat treatment of 2-3 nm and 4-5 nm, black squares and grey open circles respectively. This is compared to 4-5 nm and PtCo/C 4-5 nm with heat treatment to 900 °C, blue triangles and red open squares respectively. Reproduced from Stephens *et al.*[37] original work from Makharia *et al.*[107].

Accelerated Degradation Tests

At this point a small discussion on accelerated degradation tests (ADT) and their efficacy for determining stability is in order.

ADTs are becoming more common when establishing catalyst stability. In these, the true long term use of the fuel cell systems is attempted compressed into periods of roughly 24 hours to save time. These effects include load cycling, potential escursions and start stop cycles.[108–110] However, there are several issues with ADTs that limits the transferability of the results to true long term stability. Especially in ex-situ setups like rotating disc electrodes (RDEs) can ADTs prove very difficult. Arenz and co-workers argue that there are many paramters to concider when utilising ADTs for determining catalyst stability. The many different protocols used in literature with different potential ranges, hold times and duration makes comparison across different studies difficult, but the components used for the ADT also needs to be concidered. The potentiostat and even the software controlling it can cause deviations between the potential set and the potential applied to the working electrode (WE).[108] With the fast potential cycling and exponential dissolution dependence on applied electrode potential, the amount of dissolved Pt can vary significantly from test to test.[111] At the same time Morimoto and co-workers argue that the dissolution of Pt measured in RDE setups is directly coupled to the ion diffusion in the electrolyte and therefore loading and rotation speed, as redeposition will increase for high loadings and low rotation speed.[110] The fuel cell environment is also very different from the RDE, with higher partial pressures of O_2 and H_2 and the solid electrolyte changes the mass transport of dissolved species significantly. At the same time, compressing the many load cycles down to a mere 24 hours could promote degradation mechanisms that occur due to the cycling in potential, such as oxide formation and reduction[111] and surface diffusion.[112] Other degradation mechanisms that do not depend so much on the cycling but more on time and temperature, e.g. bulk diffusion processes, might not be captured as well in such short tests. As such, ADTs could probe the surface stability of the nanoparticles, more than the bulk stability. So while Acadts provide valuable information on aspects of long term stability they might not capture all of the mechanisms.

2.2.3 Alternatives to Platinum

A way to lower the cost of the catalyst is to remove Pt as a catalyst completely. While catalysts void of platinum group metals (PGM) is the ultimate goal, they are still in the very early stages of development. The extremely corrosive environment of the PEMFCs causes many of problems for these non-noble catalysts. Most promising are the carbon and nitrogen coordinated Fe and Co catalysts. These are produced by decomposing organometallic precursors containing the metal of interest. This can be done by heating the precursors in an inert an atmosphere of N_2 to form the active phase.[113,114]

2.3 The Story of Pt-RE Alloys

As seen above the alloys between Pt and the 3d metals allow for the initial increase in mass activity set as goal by the DOE. In accelerated testing these alloys can also exhibit great stability if the catalyst is annealed prior to testing, however, long term stability is still uncertain.[105,106] Under reaction conditions the driving force for dissolution of the solute metal is substantial, and the factors that will determine long-term stability are thermodynamic stability of the alloy and kinetic barriers for intermetallic diffusion.[32,115]

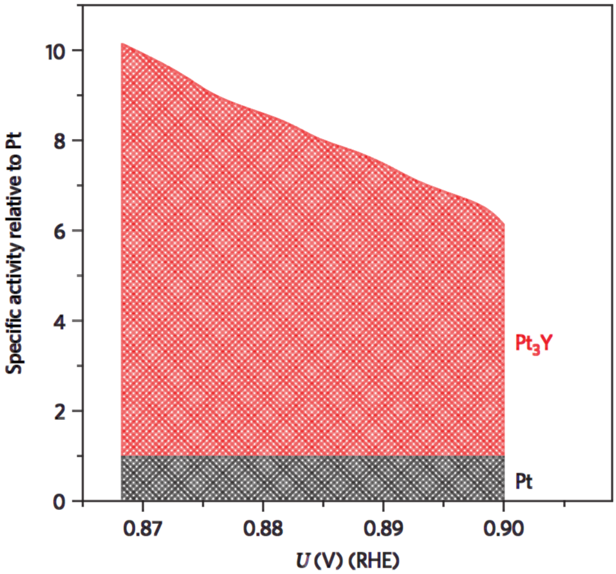

Figure 2.5: Specific activity of Pt_3Y (red) compared to pure Pt (black) for polycrystalline samples. Pt_3Y shows an enhancement from six to ten fold that of Pt. Adapted from Greeley *et al.*[116].

In 2009 Greeley *et al.* published an article describing a new class of alloys that were screened using the thermodynamic stability as a parameter together with the weakening of the *O binding energy.[116] When performing the theoretical work Pt_3Y was identified as a suiting candidate, exhibiting high alloying energy and a weakened *O binding energy. The subsequent RDE measurements of the polycrystalline sample, performed at our laboratory, revealed a six fold activity enhancement for ORR compared to pure Pt, see figure 2.5.

Since the initial publication the group at CINF-DTU and other groups around the world have continued to work with this design philosophy of thermodynamic stability. With the work they have brought new insight into the activity, structure and stability of the Pt_3Y alloy and subsequent alloys containing lanthanide and alkali earth metals.[37,117–119] The following sections will go over the literature comparing the results and highlighting the overall trends seen across the different alloys.

2.3.1 Origin of Activity: Theory and Experiment

After the initial publication by Greeley *et al.* the group and CINF-DTU expanded the group of known thermodynamically stable and active alloys to encompass many of the lanthanide metals and even alkali earth metals. All of them show an enhancement factor of three to ssix for initial activity measurements, when comparing to pure Pt.[37,117–120]

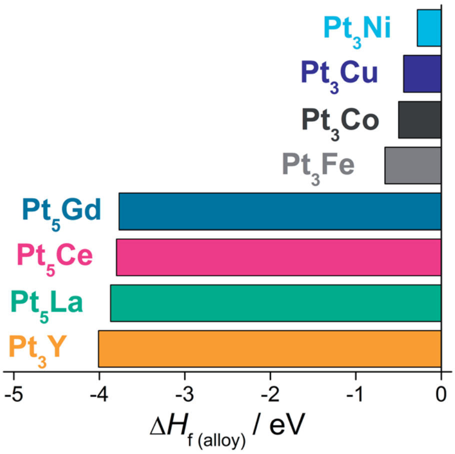

Figure 2.6: Enthalpy of formation, per formula unit in electronvolts, $\Delta H_{\mathrm{f(alloy)}}/\mathrm{eV}$, for selected $\mathrm{Pt_xM}$ alloys, where $\mathrm{x} = 3, 5$ and $\mathrm{M} =$ Ni, Cu, Co, Fe, Gd, Ce, La, Y. Reproduced from Malacrida *et al.*[120].

The examined alloys where all intermetallics found to have very negative enthalpies of formation, as seen for an excerpt of alloys in figure 2.6. The enthalpy of formation for the Pt-RE alloys are significantly more negative than for the well known 3d metal alloys.[121–125] Under the assumption that thermodynamic stability plays a role for long term stability these alloys exhibit the right trend in alloying energy. A theoretical study from 2015 by Vej-Hansen *et al.* into diffusion barriers of alloys reveal an overall correlation between alloying energy and barriers for bulk diffusion of solute metal. For alloys of Pt_3X, Pd_3X and Al_3X the barriers for interatomic diffusion increased with the allyoing energy. While These calculations were done on alloys with the cubic Cu_3Au structure the authors argue that this correlation should also hold for other structures, however, the dependence may change.[115] As a result the substantial enthalpy of formation for the Pt-RE alloys provides them with kinetic stability through barriers for bulk diffusion. However, the standard potential for dissolution of the various RE metals fall below $-2.3\,\mathrm{V}$, meaning that the overall thermodynamic driving force for dissolution is $\approx -10\,\mathrm{eV}$ at a potential of $1\,\mathrm{V}$. When factoring in the stabilisation offered by alloying of $\approx 4\,\mathrm{eV}$, the thermodynamic driving force for dissolution becomes $\approx -6\,\mathrm{eV}$.[32] The thermodynamic driving force for dissolution of the RE is therefore strong even when factoring in the strong heat of formation for these alloys.

The initial modelling of the active Pt_3Y assumed a single monolayer of pure Pt on top, the Pt-skin surface that was observed for the Pt_3Ni system. In doing so the ligand effect was a main contributor to the weakening of the *O binding energy.[116] For later publications by Stephens *et al.* and Escudero-Escribano *et al.*, used angle resolved x-ray photoelectron spectroscopy (AR-XPS) to probe the elemental composition of the alloys prior to and after electrochemical measurements.[37,117,118] After electrochemical measurements an overlayer of Pt had formed of two to four monolayers (MLs) in thickness. Figure 2.7 shows the initial and final elemental composition of a Pt_5Gd crystal as a function of depth. Underneath are sketches of what the structures can look like. From the dissolution potential described above pure Pt would be expected with no alloy, the kinetic barriers imposed by the alloying energy stabilises the bulk and stops the dissolution.

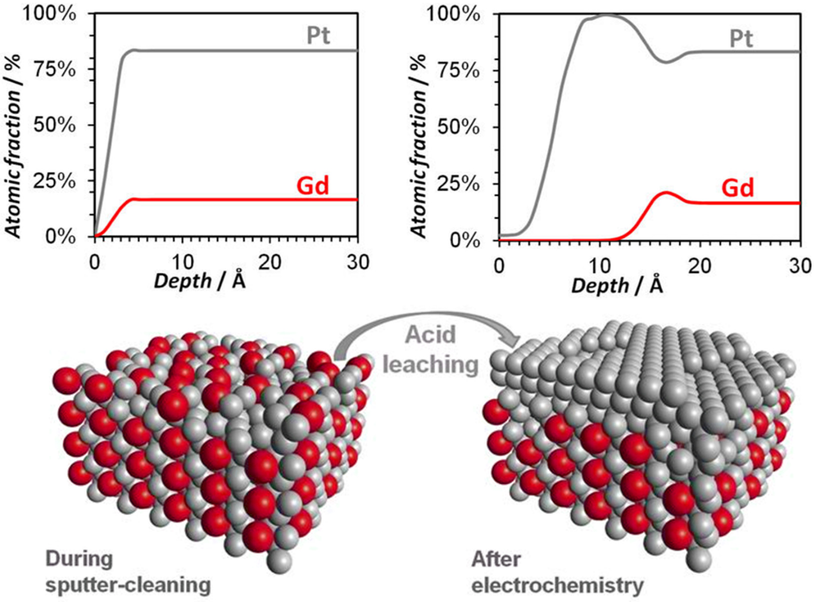

Figure 2.7: Elemental composition from non-destructive AR-XPS with artistic sketch of the corresponding structure. Adapted from Escudero-Escribano *et al.*[118,119].

This thick overlayer of pure Pt excludes the ligand effect from having any influence on the activity, and leaves only strain effects to alter the binding energies.[37,63] At the same time over the accelerated stability measurement, these alloys retain most of their activity. While Pt_5Tb has the highest initial activity Pt_5Gd retains the most activity and is still five times as active as Pt after stability measurements, see figure 2.8a. Here the alloys are ordered by initial activity, with highest activity to the left (Pt_5Tb) and decreasing as one goes to the right with pure Pt at the end.

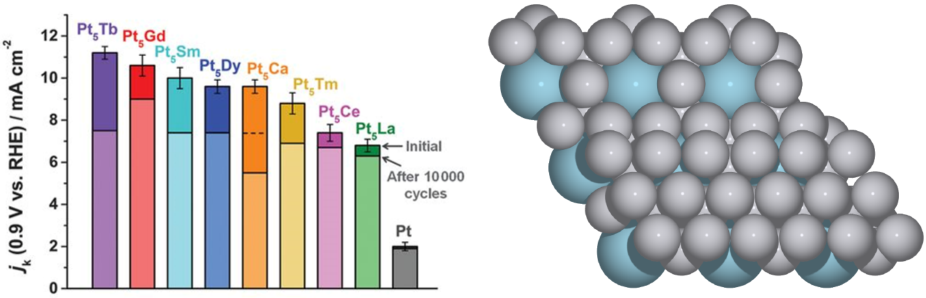

(a) Adapted from Escudero-Escribano *et al.*[119]

(b) Reproduced from Vej-Hansen *et al.*[126]

Figure 2.8: **(a)** Specific activity at 0.9 V vs. RHE of Pt and selected Pt_5M alloys, where M = Tb, Gd, Sm, Dy, Ca, Tm, Ce, La **(b)** Pt_5La kagome structure with hexagonal close packed Pt overlayer. La atoms (cyan) create vacancies in pure Pt (grey) layer. the stacking in the bulk structure for these alloys goes; Pt_3, Pt_2M, Pt_3

Explaining the Activity and Stability

All of the alloys in figure 2.8a have a stoichiometry of Pt to RE of 5:1 and the crystal structures are of either the hexagonal $CaCu_5$ or the orthorombic $AuBe_5$. The main difference between the two structures comes from the stacking sequence that causes the lattice parameter c to change, while the lattice parameter a is shared between the two structures. Common for both is the formation of kagome layers where the size of the solute metal creates vacancies in the pure Pt layers on top of it, for these structures, the Pt-Pt distance is $d_{\text{Pt-Pt}} = a/2$. As the lanthanide metals covalent radii decreases as the atomic number increases the $d_{\text{Pt-Pt}}$ also decreases, see figure 2.8b, furthermore the kagome structure allows for close-packed Pt layers on top of these vacancy layers that conform to the lattice parameter of the bulk structure. This is believed to be the cause of the strained overlayer.[37,118]
Comparing the bulk lattice parameters of the Pt_5RE alloys to that of pure Pt reveals that the strain would range from 3 % to 6 %, more than predicted for optimal *OH binding energy. In the real system, approaching the high levels of strain in these structures would cause dislocations in the Pt overlayer and strain relaxation lowering the overall strain in the surface.[97] This relaxation can

explain the decrease in activity observed as the alloys go beyond Tb in the lanthanide series. From here it would seem the structure experiences an excessive strain causing the overlayer to relax beyond optimal conditions.
Escudero-Escribano *et al.* found that the overlayer thickened after stability test, for increasing strain. As the alloying energy does not differ much from the alloys of Pt and La to those of Pt and Tm, kinetic barriers for diffusion should be similar according to what was mentioned in the previous section. As such the thickening should not stem from the changes in diffusion barriers. The authors examined the correlation between the strained bulk and the stability of the Pt overlayer. What they found was that while the strain increases activity, the overlayer is destabilised by it. This is illustrated in figure 2.9a, here the strained bulk lowers the dissolution potential of the equally compressed Pt overlayer.[119] The strain on the x-axis was derived from the experimental determination of the bulk alloys structure via X-ray diffraction (XRD). The dissolution potential was calculated by DFT and related to the reversible hydrogen electrode (RHE). The authors explain these changes in measured stability of the alloys going from Pt_5La to Pt_5Tm to This destabilisation of the overlayer.[119]

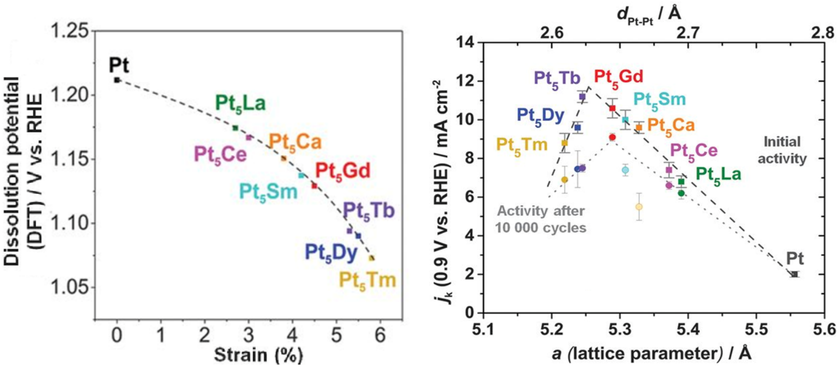

(a) Dissolution potential vs. bulk strain

(b) specific actvity vs. bulk lattice parameter

Figure 2.9: **(a)** Relationship between bulk strain and overlayer stability calculated by DFT. **(b)** Plot showing volcano-like behaviour for specific activity vs. the mean bulk lattice parameter / $d_{\text{Pt-Pt}}$. Adapted from Escudero-Escribano *et al.*[119]

The true stability of these alloys can be questioned with the observation that the higher the initial activity the higher the leaching of the alloying metal. Erlebacher and co-workers argue that for core-shell nanoparticles surface diffusion of Pt is sufficient for creating pin-holes in the surface allowing dissolution of the alloying metal in the core.[112] Coupled with this, Shao-Horn and co-workers have shown that the decreased dissolution potential observed for alloys with increased alloying energy cause excessive and continued leaching of the metal for similar sized particles.[127] With this, the Pt-RE alloys and their proposed stability seem less likely. However, the intermetallic structure of the Pt-RE alloys and the increased kinetic barriers predicted for these could still prove indispensable for true long term stability. As argued in section 2.2.2, the ADT used to determine the stability might favour degradation mechanisms coupled to the cycling of the potential and not the long term exposure to the fuel cell environment. The positive effects of the kinetic barriers would manifest itself as a reduced interatomic diffusion over long term usage, that would otherwise allow the solute metal to reach the surface and be dissolved. This will, however, only be relevant if the pin hole formation argued for by Erlebacher and co-workers does not dominate dissolution over long time scales as well. With the lack of data for these alloys in nanoparticulate form, the effect of the alloying energy on the true long term stability cannot assessed and the chemical synthesis is needed in order to provide this.

Compiling these observations, Escudero-Escribano *et al.* produced figure 2.9b. Here the initial activity and that after stability tests are plotted against the mean experimental lattice parameter / $d_{\text{Pt-Pt}}$. It is seen how initial activity decreases after Pt_5Tb and that after stability the peak of this empirical volcano is located at Pt_5Gd.

To further understand the active part of the Pt_5RE catalysts, model systems of Y/Pt(111) and Gd/Pt(111) were prepared by physical vapour deposition under ultra high vacuum conditions. The structures formed resemble those seen for the bulk Pt_5Y and Pt_5Gd, however, the surface is terminated with a pure Pt overlayer resembling the structure of annealed $Pt_3Ni(111)$.[128,129] Once these structures were exposed to electrolyte and tested for ORR the thicker overlayer, observed from the bulk samples, formed. It was these overlayers that were investigated. Utilizing synchrotron radiation for X-ray diffraction at low angles for high surface sensitivity strain and domain size of the overlayer was investigated by Pedersen *et al.*[130] They found that the overlayer is not under the same strain as observed for the bulk systems. The strain observed was in the range of 1.4 % of compressive strain for Y/Pt(111) and 0.3 % compressive strain for the Gd/Pt(111). The overlayer was also estimated to be twice as thick on the Gd system compared to the Y system. This shows how the surface strain is relaxed and more so for larger bulk compression.

2.3.2 Mass Selected and Computational Nanoparticles

While the Bulk systems have led to greater understanding as to why these alloys are active for ORR and have yielded insight into possible factors determinig alloy stability in general. These alloys are of no use unless they are also active and stable in nanoparticulate form. As mentioned in chapter 1, the translation of activity from extended surface to nanoparticles is not straightforward and the trends observed might change. Both theoretical and experimental model nanoparticle studies have been used to confirm the viability of these alloys as promising PEMFC catalysts.[131–133]

Activity and Strain

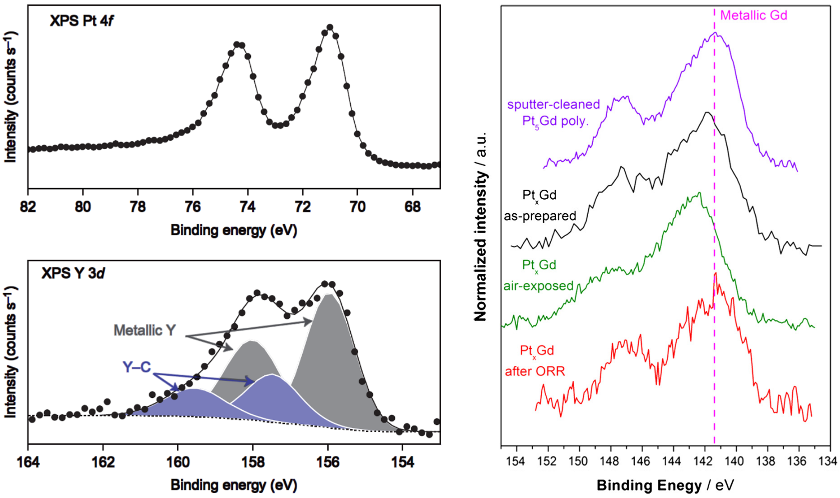

(a) Adapted from Hernandez-Fernandez *et al.*[131]

(b) Reproduced from Velazquez-Palenzuela *et al.*[132]

Figure 2.10: **(a)** XPS data for Pt 4f and Y 3d levels in Pt$_x$Y nanoparticles as deposited. The Pt 4f binding energy corresponds to that reported in literature. The grey area is ascribed to metallic yttrium, while the purple area is ascribed to an yttrium carbide. **(b)** XPS of the Gd 4d core-level for polycrystalline Pt$_5$Gd as well as Pt$_x$Gd nanoparticles. The Gd 4d is evaluated by peak position compared to the bulk alloy.

In 2014 Hernandez-Fernandez *et al.* published a study on Pt$_x$Y nanoparticles produced by a magnetron sputtering, followed by mass selection. Again in 2015 Velazquez-Palenzuela *et al.* published a similar study, this time on Pt$_x$Gd nanoparticles produced by the same process.[131,132] The nanoparticles were produced from Ar$^+$ sputtering of an alloy target with subsequent gas aggregation into nanoparticles. The mass filtering was done by using a time of flight mass filter and the desired mass was deposited on a glassy-carbon substrate (GC) for electrochemical measurements. The initial Pt:M composition from XPS of the nanoparticles ranged from 3:1 to 5:1, from XPS, even though there was no direct control of composition of the final particles.
From transmission electron microscopy (TEM) images the particles were determined to consist of smaller crystallites in both studies. This is consistent with

gas aggregation method used for making the particles. As the material produced for each sample was in the range of 50 to 300 nanograms, XRD was not a possibility for confirming the alloy formation. Instead the authors used XPS as verification method, by looking at the Y 3*d* and Gd 4*d* core-levels as seen in figure 2.10.
For the study of Pt_xY nanoparticles, figure 2.10a, it was found that the binding energy of the Y 3*d* and Pt 4*f* were at the metallic values reported in literature and in-house from measurements on Polycrystalline samples.[134] The secondary yttrium phase is ascribed to a Y-C interaction upon deposition or possible Y-OH species. For the Gd 4*d*, figure 2.10b, the complex nature of the spectra from the localisation of the 4f electrons complicates the deconvolution. Therefore the shape and position was compared to verified alloy samples from the bulk measurements reported earlier. Comparing as-deposited (black), air-exposed (green) and after ORR (red) it is clear that once the Gd in the surface layers is leached out the remaining Gd is metallic.

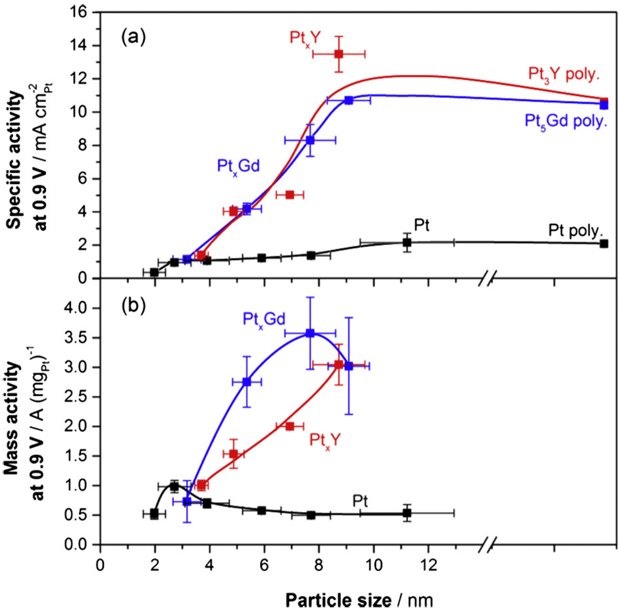

Figure 2.11: The specific and mass activity at 0.9 V vs. RHE for Pt_xY [131], Pt_xGd [132] and Pt [71] nanoparticles prepared by Ar^+ sputtering and mass selection. Reproduced from Velazquez-Palenzuela *et al.*[132].

Turning the attention to the specific and mass activity, see figure 2.11, both are among the highest reported in literature.[119,135] The Pt_xY reaches 3.05 A $mg_{Pt}{}^{-1}$ for ∼9 nm particles without reaching a maximum. The Pt_xGd on the other hand reaches a maximum at ∼8 nm particles with 3.6 A $mg_{Pt}{}^{-1}$. As the particle size increases we see that the specific activity goes toward that of the extended surfaces. It is this steady increase in specific activity that renders the mass activity more than three times that of pure Pt, the balance between the surface to bulk ratio going down and the specific activity going up shift the optimal size of the particles.

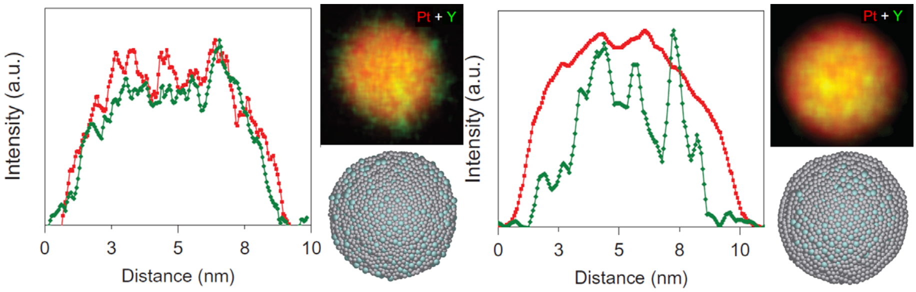

Figure 2.12: STEM EDS line scans over Pt_xY nanoparticles with EDS maps as reported by Hernandez-Fernandez *et al.*[131]. On the left is the particle before measurements. On the right is after measurements. Inserted are theoretical simulation of the different structures by Vej-Hansen [126].

From STEM-EDS mapping of the nanoparticles after ORR it is seen how a shell of ∼1 nm is depleted of solute metal.[131] Continuing this and measuring after stability test the shell had only thickened by ∼0.2 nm, what more, following the shell and core separately with EDS showed no change in core composition with Pt:Y staying at ∼5, while the shell only changed slightly from Pt:Y ∼10 to ∼11.[133,136] While there are large uncertainties connected to these observations, it is nonetheless noteworthy how this could verify the stabilising effect the alloying energy. A similar study on Pt_3Ni or Pt_3Co would be of great interest for investigating their stability under similar conditions. For the smaller particles, $\sim 3-4$ nm, it is clear that there is no enhancement in activity over pure Pt. This is explained by the lack of an alloy core to exert strain on the surface. Removing the solute metal from a 1 nm shell of a 3 nm particle leaves no structural core to alter the surface properties. This is also seen from a theoretical study performed by Vej-Hansen on the formation and properties of these nanoparticles.[126] Here the influence of the core lattice parameter on the overall and shell specific strain was investigated, using a combination of effective medium theory (EMT) and DFT. Overall nanoparticles under 4 nm would see a compressive strain resulting in a smaller $d_{\text{Pt-Pt}}$, however, the average compression of the active surface sites would not be significantly different from that on Pt and the frequency of these sites would be lower than on pure Pt.

Overall the strain, as calculated from the EMT and DFT modelling, fall in line with the experimental observations of the average particle strain / $d_{\text{Pt-Pt}}$. As seen of figure 2.13 the activity, irrespective of sample and treatment, increases with the measured mean particle strain as measured by extended X-ray absorption fine structure (EXAFS).

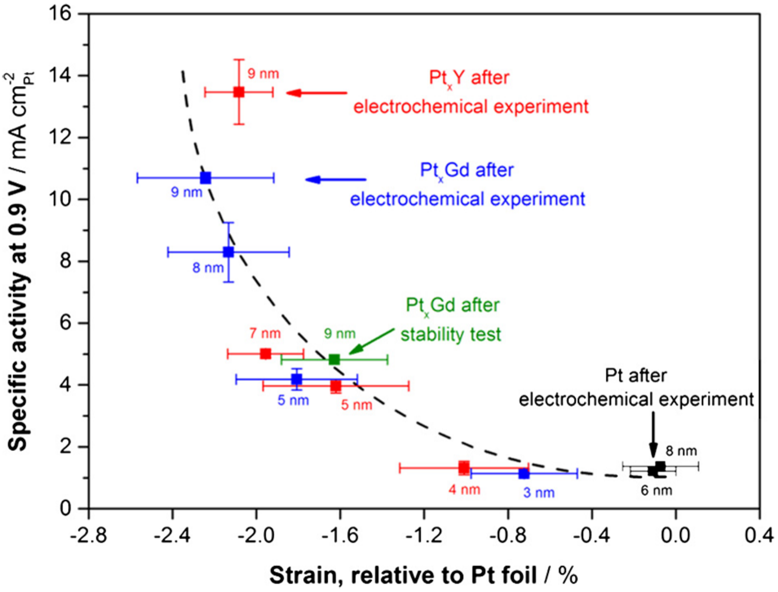

Figure 2.13: Specific and mass activity at 0.9 V vs. RHE for Pt_xY [131], Pt_xGd [132] and Pt [71] nanoparticles as function of strain measured by EXAFS. Reproduced from Velazquez-Palenzuela *et al.*[132].

Bulk structure and Overlayer-Strain

The theoretical work done by Vej-Hansen also delved into the crystal structure of the nanoparticles and the effect of this on the overlayer strain. As already mentioned the Pt_5M alloys of interest here are all known to be of the $CaCu_5$ type, with hexagonal symmetry, and the $AuBe_5$ type, with an fcc symmetry for the yttrium atoms surrounded by the Pt atoms. This structure is similar to the $CaCu_5$. The Pt_3M alloys are of the Cu_3Au type, a close packed structure. Through the theoretical screening a third structure was recognised for Pt_5Y, it resembles the $CaCu_5$ in that the Pt_3 layer with a vacancy in it expands to remove this. The stacking sequence changes from that of ABAB in $CaCu_5$ to ABAC in the new structure. As such it resembles a double-axis hexagonal close-packed (dhcp) structure. Moreover these three structures are very close in energy, making it difficult to predict which structure will be preferred.

Both the $AuBe_5$ and the $CaCu_5$ structures have Pt-Pt distances that are shorter than in pure Pt, however, the Cu_3Au and dhcp structures both have expanded bulk structures compared to Pt. Nonetheless, all the simulations on the known structures showed shorter Pt-Pt distances in both cores and overlayers. The author offers the explanation that the shell decouples from the core with sufficient

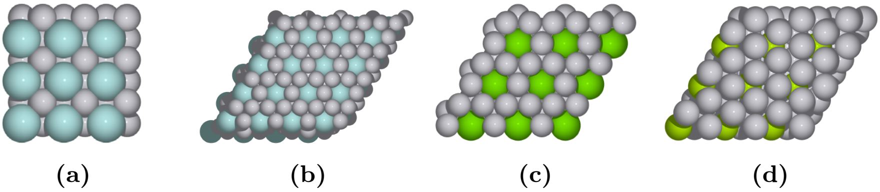

Figure 2.14: The four different bulk structures for the Pt_xM alloys of interest are **(a)** Cu_3Au close packed structure, **(b)** $AuBe_5$ fcc structure, **(c)** $CaCu_5$ hexagonal and **(d)** dhcp. Adapted from Vej-Hansen [126]

difference between the lattice parameters in core and the Pt shell. This allows the shell to contract to lower its overall energy and increasing catalytic activity. These are however not the only alloys formed by Pt and the REs. One alloy structure that can be detrimental to the catalytic activity is the $MgCu_2$ that is formed for the Pt RE alloys.[137–139] This phase was shown to be unstable during electrochemical measurements by Stephens *et al.*[117] To further complicate the structure system the only difference in structure between the $MgCu_2$ and $AuBe_5$ is the placement of the individual atoms.[140] This close relation between these two structures and the close relation between the dhcp structure and the $CaCu_5$ and the $AuBe_5$ structure lead to a very complex structure system. A system that very well could have many more structures in close relation to those mentioned here. An example of this is the proposed structure of the Pt_5Gd alloy formed in the study of Gd modified Pt(111).[129] The unit cell needed to describe the hexagonal structure observed counted 6 layers in the stacking sequence repeated three times with two displacements perpendicular to the c-axis of the unit cell.

2.3.3 Chemical Synthesis

The bulk system and the model nanoparticle studies have provided great insight into the viability and underlying nature of this group of alloys. One area they do not tackle is the viability of producing these alloys in an active form with a scalable method. The major obstacle that has so far prevented widespread reports of successful synthesis of the alloys of interest is the appreciable difference in standard reduction potential. Taking the reduction of Y^{3+} at -2.38 V and comparing it to that of Pt^{2+} at $+1.18$ V shows the core issue. While Pt is easily reduced by just about anything, yttrium and the other REs can only be reduced by very few reducing agents. This is very different from the case of Pt and late transition metals such as Ni, for which the standard reduction potential for Ni^{2+} is -0.26 V.[32] The REs also form very stable oxides, with yttrium being one of the most oxyphilic elements, furthering the difficulties.[141] The following sections will present what has been published in literature on the chemical synthesis of Pt RE alloys.

Prior Art - Bulk-like Synthesis

High temperature reduction of yttrium and lanthanide oxides and fluorides together with Pt powder has been reported by several groups using either H_2 or NH_3 as reducing agent.[142–144] These were in the form of unsupported powders and would not be applicable as electrocatalysts. When analysing the powders with XRD they were found to have the hexagonal structure of $CaCu_5$, or the orthorhombic structure of $AuBe_5$ for the alloys studied, the same as reported for arc-melted alloys. The alloys of composition Pt_3RE was found to be of the same Cu_3Au structure as already mentioned.[145–147] These structures match those reported earlier by Stephens *et al.*[117] and Escudero-Escribano *et al.*[118,119] Another method also based on thermal reduction was reported by Lux *et al.*, synthesising yielding crystallites of Pt_2Ce and Pt_2Pr of ∼25 nm.[148,149] The flash reduction of the catalyst was done from a cyanide complex ($HLn[Pt(CN)_6]_2$) under a flow of hydrogen at 800-1000 °C. The complex was formed from $Ln(NO_3)_3$ and $K_2[Pt(CN)_6]$ prepared in the presence of water and air. While the catalyst was unsupported and of an unwanted stoichiometry that will corrode upon electrolyte exposure,[37] the method holds the desired trait of being seemingly insensitive to water present during preparation of the precursor.

Prior Art - Chemical Synthesis

The previous examples, while successful in forming the alloys, only yielded large crystallites, not suited for electrocatalysts. The other methods that have been reported have been more akin to the methods used to synthesise the platinum late transition metal alloys. Jeon *et al.* reported the suposed synthesis of carbon supported Pt_3Y back in 2011 by reducing $H_2PtCl_6 \cdot 6H_2O$ together with $Y(NO_3)_3 \cdot 6H_2O$ [150]. This was done using $NaBH_4$ as reducing agent in a mixture of methanol and de-ionised water. They report only slight doping of Y in their nanoparticles as no alloy phase is observed in XRD measurements. Attempting conventional reduction methods in any solvent containing water is from a thermodynamics point of view not going to succeed. For one mole of yttrium converted to half a mole of Y_2O_3 the enthalpy of formation is -9.41 eV, close to twice the enthalpy of formation for one mole of Pt_3Y at -3.98 eV.[141,151] So in an solvent consisting mainly of H_2O, the oxidation will always be favoured. Another study by Liu *et al.* claimed to have made Pd-Y-Pt/C, a PtY alloy shell on a core of Pd.[152] Their idea was to absorb H_2 in the Pd core and use that to reduce the Y precursor. This was then covered by a Pt shell. While they claim alloying from XPS and TEM measurements, their binding energy of the $Y3d_{5/2}$ at 157.9eV is clearly an oxidised species when compared to the $Y3d$ spectrum for the cluster source Pt_xY nanoparticles in figure 2.10a. Their enhancement can also directly be explained by an increase in active surface area. Other groups have reported enhanced activity towards methanol oxidation and ORR from oxide and hydroxide decorated Pt/C nanoparticles.[153,154] The preparation of Pt_3Gd under solvothermal conditions was reported by Dipankar *et al.*[155] The synthesis was performed during in-situ X-ray scattering measurements while under a 250 bar pressure and 250 °C. Here a 1:1 molar mixture of $H_2PtCl_6 \cdot 3H_2O$ and $GdCl_3 \cdot 6H_2O$ in ethanol was reportedly reduced with the calculated pair distribution function after reduction best matching that of a Pt_3Gd phase. This catalyst was, however, not measured electrochemically or confirmed by either ex-situ XRD or XPS.

While not directly synthesis of the relevant alloys it has been reported that the Lanthanide metals can be reduced using alkalides. These are complexes of alkali metals and crown-ethers, stabilizing the metal ions K^+ and Na^- in solution, resulting in a reducing power close to 3 V.[156–160] More recently Yan *et al.* showed Au covered Gd nanoparticles prepared using alkalides.[161] No direct evidence of metallic state was supplied and only evidence of something other than Au was from XRD showing a phase not belonging to bulk Gd, that they ascribed to a nano-phase of Gd. TEM images show a different core structure compared to the confirmed Au shell, this was accompanied by EDS showing the presence of Gd but not the chemical state of it.

Finally electrodeposition of PtY has been reported by Han *et al.* in anhydrous ethanol.[162] Starting from H_2PtCl_6 and YCl_3 in the anhydrous ethanol the potential was set to -4.3 V vs the reversible hydrogen electrode (RHE) for 1500s. They do show specific activities higher than expected for pure polycrystalline Pt, there is no direct proof of alloying and yttrium could act as a capping agent promoting selective growth of facets.[163] Similar to electrodeposition, cathodic corrosion has been shown to be able to form alloys from corroding a Pt-wire in an electrolyte containing salts of the desired solute metal.[164] In general cathodic corrosion has shown great potential as a top down method of creating nanoparticle alloys of Pt, starting from the desired alloy in wire form.[165–167]

Chapter 3

Experimental Methods

This chapter will go over the experimental techniques used to characterise the different catalysts synthesised. The purpose of these techniques have been to verify the alloys of Pt and REs, as such techniques that allow for structural verification of the crystal structure and the verification of the metallic state has been integral. Namely X-ray diffraction (XRD) and X-ray photoelectron spectroscopy (XPS). Other techniques that are able to help understand local differences and local structures have been used as a supplement. These include several electron microscopy EM techniques. Finally the catalysts have been tested electrochemically to explore their activity for the ORR. The methods used for preparing the different catalysts will be presented in the respective chapters of their introduction.

3.1 X-ray Diffraction

X-ray diffraction (XRD) was used to determine the crystal structure of the synthesised catalysts. This section is based on the sources in [42,168]. The technique is based on elastic scattering of a specific radiation wavelength on the periodic lattice of the sample. The radiation source can be X-rays, neutrons or electrons. When these are directed towards a sample the wave will be elastically scattered on the crystal lattice. At certain angles the scattered waves will be in phase and amplify the signal. As such the interplanar distance in the crystal structure will define when this constructive interference occurs and be a fingerprint of the structure. the condition for when this happens is given by Braggs law.

$$n\lambda = 2d \sin(\theta) \quad , n = 1, 2, ... \tag{3.1}$$

Here θ is the angle relative to surface, d is the spacing between the different lattice planes and λ is the wavelength of the incoming wave. This relation can be seen on figure 3.1. As more planes contribute to the interference the shape of the peaks will become sharper.

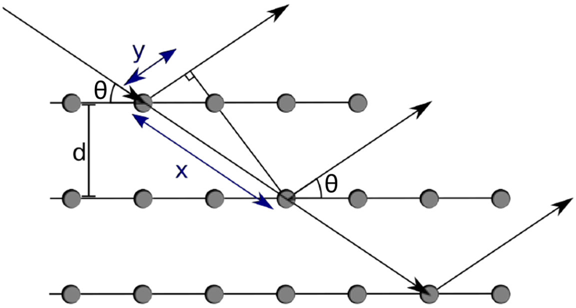

Figure 3.1: Sketch of Bragg condition for constructive interference. The lattice planes are separated by d, and the angle of the incoming wave to the surface is θ. Adapted from [168].

3.1.1 Setup and Measurements

For the actual measurements two systems were used, both were from PANalytical. One was an Empyrean, located at Danish Technological Institute (DTI), and the other was a X'Pert Pro. For both zero background plates and a spinner stage for automatic sample change and measurement was used to ensure correct alignment of sample height and streamlining the measurement process. For measurements at DTI a standard of LaB_6 was used and for in-house measurements a pressed powder Si standard was used. All structures (and if applicable ICSD code) are listed and described in appendix A.

3.1.2 Data Analysis

All data analysis of XRD data was handled in the PANalytical software package HigScore Plus. It was also used to perform the Rietveld analysis described below.

Rietveld Refinement

Rietveld refinement is used to extract information on size, strain and composition of samples characterised by scattering. For it to be applicable information on all the phases that are present in the sample is needed. An incomplete picture of the sample can give results that are not physically sound. The calculated profile is fitted to the measured profile by changing the structural parameters for the different phases present in the sample.

As the shape and width of the diffraction peaks change with the diffraction angle, due to instrumental effects and the Voight function nature of X-ray diffraction peaks a standard is measured first to capture these effects. With the the decription of the system broadening as a function of the diffraction angle, the broadening from the catalyst can be extracted after measurements of the sample. To account for any asymmetry to the peaks that the instrument may introduce, the Finger, Cox & Jephcoat asymmetry function[169] was used and only size analysis was done with Rietveld refinement.

3.2 Small Angle X-ray Scattering

Small angle X-ray scattering (SAXS) was used to determine particle sizes of the seed Pt/C catalysts. As the name suggests it is a technique that relies on X-ray scattering at small angles, here it probes the electron density on a length scale of 1-100 nm.[170,171] Probing at these length scales allows SAXS to measure particle and pore sizes of different material without them having to be crystalline.

The SAXS measurements were done on the Empyrean diffractometer at DTI using a vacuum pumped stage. Prior to sample measurements the support material was measured and the signal was subtracted from the catalyst signal in order to separate out the metal nanoparticles. The analysis was performed by Solveig Røgild Madsen and Christoffer Mølleskov Pedersen from DTI, using the EasySAXS software package from PANalytical.

3.3 X-ray Photoelectron Spectroscopy

X-ray photoelectron spectroscopy (XPS) is a widely used technique for identifying both the presence of an element in a sample and the chemical state of it.[42,172] It relies on the electronic structure of the elements for the identification. By irradiating the atoms, in this case with X-rays, and exiting the system, electrons are ejected from the different elements with a kinetic energy that depends on the binding energy in the element, the energy of the radiation used and the chemical environment of the element. This relation is described in equation 3.2.

$$E_{kin} = h\nu - E_b + E_{chem} - \Phi \tag{3.2}$$

Here $h\nu$ is the energy of the incoming X-ray, E_b is the binding energy of the emitted electron, E_{chem} is the contribution from the chemical environment and contain information on the oxidation state. Finally Φ is the work function of the analyser.

The energy of the electrons emitted is normally in the range from 10 eV to 1000 eV. This energy range limits the electrons mean free path to less than 20 Å as seen from figure 3.2. While X-rays penetrate deep into the sample and excite atoms only those electrons ejected within the first couple of nanometers contribute to the signal. This makes XPS a surface sensitive technique that is especially useful for identifying surface contaminations.

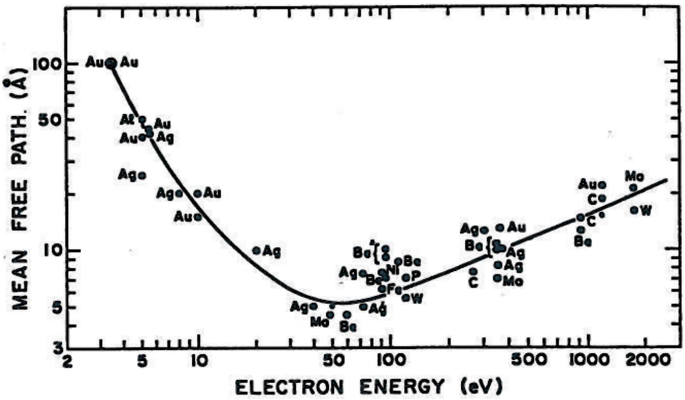

Figure 3.2: Universal electron mean free path as function of kinetic energy. Reproduced from from [172].

The intensity of the signal from each element differs as the cross section for the electron emission changes with electronic configuration and thereby the elements. To properly quantify the amount of elements present the sensitivity for each element needs to be established.

The surface sensitivity of XPS can actually impede the analysis of the Pt-RE alloys. In chapter 2 it was explained how the active structure of the catalyst has an overlayer of pure Pt on top of the alloy. With this follows that the signal from the alloying element, be it Y, Gd or any other rare earth is very low. Therefore identifying the presence of the elements can be difficult, and it often manifests in the absence of RE from the survey scan if the catalyst has been acid washed.

3.3.1 Setup and Data Analysis

All measurements were carried out using a Theta Probe system from Thermo Fisher Scientific, with a base pressure of less than $2{\cdot}10^{-9}$ mbar. It was operated with a monochromatised Al anode using the Kα (1486.7 eV) line and a spot size of 400 μm. All samples were pressed onto carbon tape placed on a cut-out of Al foil prior to measurements to ease handling.

All data treatment was done in the Avantage software suite from Thermo Fisher Scientific, with sensitivity factors for Y established by Paolo Malacrida.[173] Other sensitivity factors used were taken from the Avantage software database. For alls samples a survey spectrum was recorded to identify the most prominent elements present and identify any significant contaminations. For the most intense peaks and for any identified contaminations detailed spectra were recorded and quantified using a Shirley type background. For each peak recorded the fitting was done with as few phases as possible in order to obtain a sufficiently low residual.

3.4 Electron Microscopy

Several types of electron microscopy (EM) techniques were used to characterise the synthesised catalysts. With the previously mentioned techniques average values for the system is acquired as the probe is macroscopic. With EM electrons are used to investigate the structure and elemental composition of the sample on a more localised scale. The nature of the electron allows for resolution in the Åregime, allowing for direct imaging of the nanometer structures of catalysts.[168] The following sections will introduce the specific techniques used and the spectroscopic techniques used to gain elemental information and will primarily be based on the corresponding chapters in source [168].

3.4.1 Transmission Electron Microscopy

Transmission electron microscopy (TEM) can to a large extend be compared to its optical analogue. In both a "light" source illuminates a subject, with which it interacts and the modulated light is then magnified through lenses. These lenses can have imperfections causing aberrations in the image. For the TEM the light source is an electron emission source either a thermionic or field emission gun (FEG). The optical lenses are traded for electromagnetic lenses that unfortunately are not as perfect as their optical counterparts and spherical aberrations are the largest limitation for resolution in TEM.[168]

In TEM the sample is illuminated by a parallel coherent beam of electrons at an acceleration voltage of $80 - 300\,\mathrm{kV}$. The particle-wave duality of the electrons causes the wavefronts to interact with the sample lattice, modulating it as the potential varies over the lattice. This modulation of the wave front is essential to the atomic resolution attainable. This modulation by the potential can lead to columns of atoms both showing as dark spots and bright spots depending

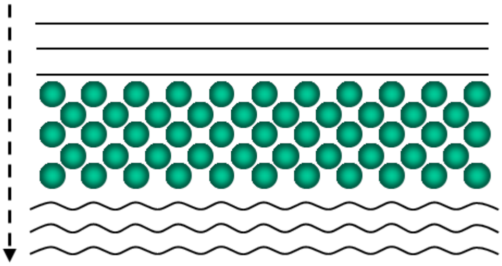

Figure 3.3: Electron wavefront passing through a crystal lattice causing modulation from interaction with the varying potential.

on the alteration of the wavefront. This makes the interpretation of images more challenging. Besides the modulation of the wavefronts scattering also contributes to the image with both mass-thickness contrast and diffraction contrast. Mass-thickness contrast causes the heavier/thicker areas of the sample to show up darker in the final image as more electrons scatter from interaction with sample. Diffraction contrast does the same with crystalline samples, showing up darker as scattered electrons does not make it to the final image.

3.4.2 Scanning Transmission Electron Microscopy

In scanning transmission electron microscopy (STEM) the parallel beam is exchanged for a collimated incoherent beam. This probe is then rastered over the sample with each point in the image generated by a probe point. Here resolution is directly related to the probe size and how aberration free it is. Two types of images can be formed; bright field and dark field. For bright field the directly transmitted electron beam is recorded. For dark field imaging the scattered electrons are collected and for scattering above $\sim 50\,\text{mrad}$, where only elstically electrons are scattered to. This ensures that only mass-thickness contrast play a role, as such atoms will therefore always be bright spots. The intensity then depends on the thickness of the sample and also scale exponentially with the atomic number ($I \propto Z^{1.7}$). This detector is known as the high-angle annular dark field (HAADF).[168]

3.4.3 Scanning Electron Microscopy

Scanning electron microscopy (SEM) is analogues to STEM with the differences being acceleration voltage and the signal recorded. It is not the transmitted signal, however, it is the backscattered electrons (BE) and secondary electron (SE) generated by the incident beam. These are collected by detectors on the same side of the sample as the electron gun. The SEs are generated by the primary beam electrons ejecting electrons from the near surface region of the sample. The intensity of the signal from SEs couples to the topography of the sample as convex surfaces will allow for more electrons escaping the surface.

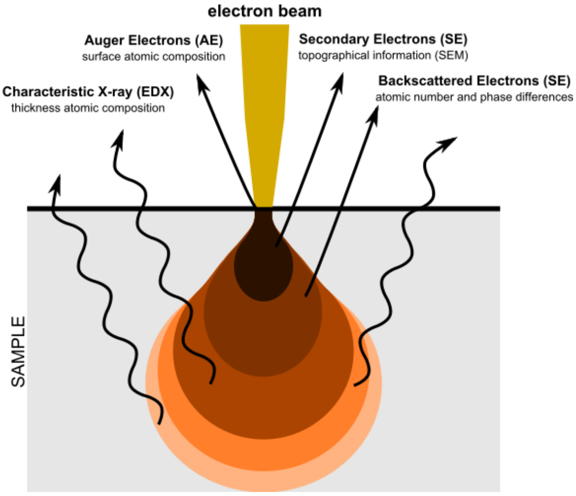

Figure 3.4: Interaction volume from SEM with characteristic emissions from secondary electrons, backscattered electrons and relaxation related emissions of Auger electrons and element characteristic X-rays. The coloured area defines the interaction volume that will determine resolution. Adapted from [174]

The BEs are primary beam electrons that undergo elastic scattering events on the atoms in the surface. As for the scattered electrons in STEM, the intensity scales with the atomic number and BEs therefore yield mass contrast.
The overall resolution of the SEM is defined by the interaction volume, which is the volume from which SEs, BEs escape together with characteristic emissions from Auger electrons and X-rays.

3.4.4 Energy Dispersive X-ray Spectroscopy

In both STEM and SEM the incident beam will leave excited atomic states. When these relax they can emit characteristic X-rays with energies specific for the electronic transition of the excited state. These X-rays will form a fingerprint for each element and can be used to identify the elements present and quantify the amount of them. When EDS is used in STEM the interaction volume is very small, only slightly larger than the probe, causing the amount of emitted X-rays to be very small at the same time the collection of X-rays is limited by the detector size and placement. In comparison EDS in SEM is help significantly by the larger interaction volume, however, the resolution is then limited by the interaction volume. As for XPS sensitivity factors need to be applied for this quantification as the characteristic emission varies over the elements.

3.4.5 Microscopes

To characterise the catalysts prepared, several microscopes were used for different techniques. The microscopes and conditions used will be listed in this section.

Tecnai T20 G^2 TEM is a 200 kV thermionic (S)TEM with a LaB_6/CeB_6 filament and is optimised for TEM. It has been used for TEM imaging of the catalyst samples for crystal structure. Work on this microscope was carried out by Claudie Roy from DTU-CINF.

Titan Analytical 80-300ST TEM is a 300kV monochromated FEG (S)TEM equipped with a CESCOR C_s spherical aberration corrector for the condenser lens. The microscope is optimised for STEM imaging. In this project it has been used to image the catalyst samples in HAADF-STEM mode. For elemental analysis EDS was used with a X-MAX SDD EDS detector from Oxford Instrument.

3.5 Electrochemical Measurements

This section will go over the setup and procedure used for evaluating the electrochemical performance of the synthesised catalysts. All measurements were carried out by Amado Velázquez-Palenzuela and Christoffer Mølleskov Pedersen from CINF-DTU.

All measurement were done in a three electrode setup, consisting of a working electrode (WE), a counter electrode (CE) and a reference electrode (REF). A sketch of the setup can be seen on figure 3.5 with the components marked. This setup allows for potential monitoring/control between the WE and the REF that has a fixed potential vs. the standard hydrogen electrode (SHE). At the same time the CE closes the circuit running the counter reaction to that on the WE. Not drawn on the figure is a second CE used when immersing the WE. By connecting these electrodes the WE can immersed under potential control ensuring that it does not go to any unwanted potentials during immersion. For all measurements a $Hg|Hg_2SO_4$ electrode was used as REF. It was placed a separate compartment connected through a Lugin capillary with a ceramic frit. A Pt-wire was used for CE. Controlling the electrode potential and measuring the current was done using a Bio-Logic VMP2 potentiostat with the EC-Lab software suite from Bio-Logic.

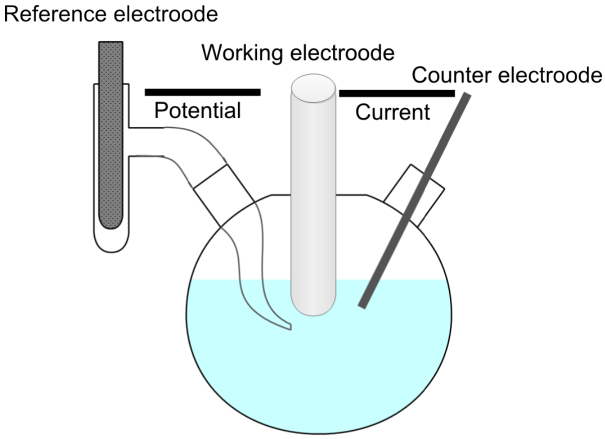

Figure 3.5: Sketch of the three electrode setup with the compontent WE, CE and REF marked. Reproduced from [134].

The cell was a custom-made three-electrode glass cell with an external jacket attached to a water bath with temperature control. Prior to the measurements the cell was cleaned with piranha solution, made from three parts 98% H_2SO_4 (Merck, Emsure®) and one part 30% H_2O_2 (Merck, Emsure®). It was left for at least 24 hours and then cleaned several times in 18.2 MΩ cm Millipore® water at 85 °C – 90 °C to remove traces of the cleaning solution.

Reversible Hydrogen Electrode

In order to be able to compare results across different electrolyte conditions, theRHE scale was used. To determine the shift between the used REF and the RHE, the potential was cycled between $-0.75\,\mathrm{V}$ and $0.28\,\mathrm{V}$ vs. the $\mathrm{Hg|Hg_2SO_4}$ in H_2 saturated electrolyte at $50\,\mathrm{mV\,s^{-1}}$. The OCV value is then taken as the shift and was normally between $-0.720\,\mathrm{V}$ and $-0.715\,\mathrm{V}$. The potential was the corrected by equation 3.3.[175,176]

$$U_{\mathrm{RHE}} = U_{\mathrm{REF}} - U_{\mathrm{OCV,H_2}} \tag{3.3}$$

Ohmic Drop Compensation

To correct for the cell resistance, potentiostatic impedance spectroscopy was performed from 100 kHz to 10 Hz with 10 mV pulses. The Ohmic drop was then found from fitting the high frequency part and reading the intercept. Equation 3.4 shows how the potential is corrected for the ohmic drop.

$$U_{\text{IR-Free}} = U_{\mathrm{Measured}} + I \cdot R_{\mathrm{ohmic}} \tag{3.4}$$

3.5.1 Rotating Disc Electrode

One of the techniques that sees the widest use for laboratory scale evaluation of electrocatalyst for fuel cells, is the rotating disc electrode setup (RDE).[33,38,177–179] This method is to an extend able to emulate the environment inside the fuel cell without having to construct an MEA every time a catalyst needs to be evaluated. To mitigate the mass transport problems associated with measuring in stagnant electrolyte, the (WE) is rotated to increase mass transport. This does not remove mass transport problems and the diffusion limited current for a uniform electrode film can be calculated from the Levich equation 3.5

$$j_d = 0.62nFSD^{2/3}C\nu^{-1/6}\omega^{1/2} \tag{3.5}$$

For this equation n is the number of electrons transferred, four for the ORR, F is the Faraday constant, S is the surface area of the electrode, D is the diffusion coefficient of the reactant in the electrolyte, ν is the viscosity of the electrolyte and ω is the rotation speed of the electrode. At a rotation speed of 1600 rpm the theoretical diffusion limited current density is 5.8 mA cm^{-2}.[38,177,178] To further simulate the fuel cell, the kinetic current in the absence of diffusion restrictions is estimated by equation 3.6.[177,179]

$$j_k(V) = \frac{j_d \cdot j_m(V)}{j_d - j_m(V)} \tag{3.6}$$

Here j_k is the kinetic current density, j_d is the diffusion limited current density and j_m is the measured current density at a given potential. For the nanoparticle experiments, the electrochemically active surface area is used for determining the current densities.

To move beyond the limitation of the standard RDE, a high pressure - high temperature RDE system as the one presented Arenz and co-workers would allow for more realistic mass transport scenarios.[180] Moving beyond the RDE setup a floating electrode like that demonstrated by Kucernak and co-workers[181,182] or the gas diffusion electrode by Arenz and co-workers[183] could be utilised. However, these were not used during these studies.

3.5.2 Electrode Preparation

Activity and stability measurements were carried out for the both commercial and synthesised catalysts. The commercial catalysts were a 60 wt% $\sim$ 3 nm Pt/C catalyst and a 50 wt% $\sim$ 6.6 nm Pt/C catalyst with the product numbers TEC10F60TPM and TEC10EA50E-HT repsectively. Both catalysts were from Tanaka Kikinzoku Kogyo K.K. (TKK).

Electrodes were prepared by drop casting a thin film of catalyst ink onto a

5 mm glassy carbon disc from Pine Instruments. These were prior to deposition polished using a Buehler MicroPolish^{TM} 0.05 µm alumina particles on a Buehler MicroCloth^{TM} PSA, followed by ultra-sonication twice in isopropanol and deionised water respectively.
The ink formula used contains 5mg of catalyst suspended in 1.4 mL of Millipore® grade water, 5 mL of ethanol or isopropanol, in both cases 99.8 % from Sigma-Aldrich (puriss. p.a., ACS Reagent). To this 15 µL of 2 wt% polyvinylpyrrolidone (PVP) solution and 20 µL of Nafion® solution (5 wt% in mixture of lower aliphatic alcohols and water) were added, both from Sigma-Aldrich. The mixture was mixed using an ultrasonic horn and re-dispersed prior to deposition of 10 µL ink. This yielded electrodes with a Pt loading of ~14 $\mu g\,cm^{-2}$, and mass fraction of catalyst, Nafion and PVP of 80 wt%, 19 wt% and 1 wt%, respectively. prior to all measurements a base cyclic voltammogram (CV) was recorded in N_2 saturated 0.1 M $HClO_4$

3.5.3 Activity Measurements

For the electrochemical testing, the WE was immersed into the cell under potential control at 0.10 V in N_2-saturated 0.1 M $HClO_4$ electrolyte, made from 70% Merck Suprapur $HClO_4$ and Millipore water. To clean the surface the electrode was subjected to potential cycling between 0.05 V and 1.00 V at 200 $mV\,s^{-1}$ until a stable cyclic voltammogram was achieved, often 100 to 200 cycles. Following this, the ORR performance of the catalysts was evaluated by means of hydrodynamic voltammetry in O_2-saturated solution at 50 $mV\,s^{-1}$ and 1600 rpm. Following the ORR experiment, CO-stripping analysis was carried out for determining the electrochemical surface area (ECSA).[177–179] Here, CO gas was first bubbled into the electrolyte for 2 min, while keeping the WE potential at 0.05 V; then, the remaining CO dissolved in solution was removed by purging with Ar for 15 min while the potential was kept constant. The stripping cycle consisted of potential scanning up to 1.00 V in Ar-purged solution at 50 $mV\,s^{-1}$. The corresponding ECSA of the catalyst was estimated assuming a ratio of 420 $\mu C\,cm^{-2}$. All gasses used were of instrument 5.0 quality from AGA. The activity was evaluated at 0.9 V vs. RHE using equation 3.6 to compensate for the diffusion limitation.

CHAPTER 4

Chemical Synthesis Methods

As mentioned in chapter 2 there is great potential in the Pt-RE alloys, however, no convincing method for the scalable synthesis of these alloys have been published. This chapter will introduce the different techniques investigated to enable the scalable synthesis of Pt-RE alloys. The idea behind the methods along with setups and procedure will be described, as well as the results from characterisation. The first method studied was alkalide reduction first introduced in chapter 2. Christoffer Mølleskov Pedersen was an integral part of planning the experiments. The next method studied was cathodic corrosion, which was studied in cooperation with Amado Andres Velázquez-Palenzuela who also carried out the electrochemical characterisation. The last method was based on previous work done in my Master thesis, this method is referred to as the high temperature reduction method.[134] Christoffer Møleskov Pedersen was involved in the planning and completion of the experiments and also carried out the electrochemical investigations.

4.1 Alkalide Reduction

In chapter 2 alkalides were presented as being a group of compounds with the potential to reduce the highly oxophilic RE metals.
Mixing alkali metals with a suitable, non-reducible, organic complexant allows

for the formation of an alkali cation and anion forming a sandwich structure with the complexant. The alkali anion then has a reducing power $\sim 3\,\mathrm{V}$, enough to reduce the RE metals. The alkalides are similar to dissolving alkali metals in liquid ammonia with the significant difference that choosing the right complexant for the alkalide allows for working at significantly higher temperatures.[157,158,184,185] The method adopted herein comes from the work of Yan *et al.*, with alterations to stoichiometry and metals in order to form the desired alloy.[161]
The work presented by Yan *et al.* focused on the core-shell structure of Gd@Au. For the current study, the method was therefore adapted to either make Gd@Pt, Y@Pt or Pt_3Y. The alkalide chosen was the same as in the reported work, namely the complex between the crown-ether; 15-crown-5 (98 %, Sigma-Aldrich) and Na and K, here in the form of NaK alloy (99.95 %, Sigma-Aldrich). The complex formed can be seen in figure 4.1.

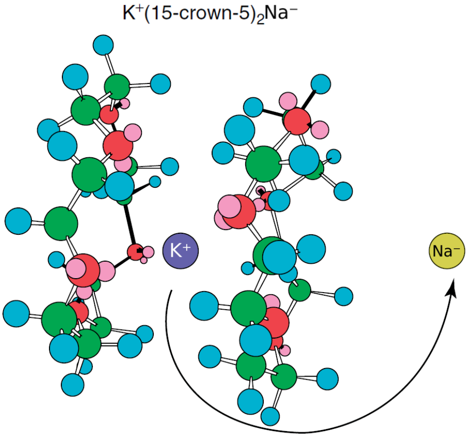

Figure 4.1: Sketch of the alkalide structure used in this work. The sandwich structure between the 15-crown-5 ether and NaK alloy. Adapted from Wagner [185].

The precursors for the metals used were $PtCl_4$ ($\geq 99\,\%$, Merck, anhydrous for synthesis), YCl_3 and $GdCl_3$ (both 99.99 %, Sigma-Aldrich, anhydrous powder), with the solvent being tetrahydrofuran (THF) ($\geq 99.9\,\%$, Sigma-Aldrich anhydrous < 20 ppm H_2O, inhibitor-free). The THF was further dried by refluxing over metallic Na (99.95 %, Sigma-Aldrich) with benzophenone (99 %, Sigma-Aldrich ReagentPlus®) under an inert atmosphere of Ar (instrumental N5.0, AGA) until a persistent deep blue/purple colour. This colour indicates the presence of the benzophenone ketyl radical and the absence of O_2 and H_2. From here the solvent was distilled into closed flasks and stored over a molecular sieve (3 Å, Sigma-Aldrich).[186–188] All handling and storage of the chemicals as well as the actual synthesis was performed in an Ar-filled glovebox (Vacuum Atmo-

spheres, O_2 and H_2O below 0.5 ppm) at room temperature.
The overall reaction is illustrated with equation 4.1. Here the alkalide reacts with both the Pt and Gd precursors reducing them into nanocrystals of the composite. Had the goal been the formation of the core-shell structure the Gd salt would be added first with subsequent addition of Pt salt.

$$\begin{aligned} &2\mathrm{GdCl_3} + 10\mathrm{PtCl_4} + 23\left[\mathrm{K^+}\,(\text{15-crown-5})_2\,\mathrm{Na^-}\right] \rightarrow \\ &2\,(\mathrm{Pt_5Gd})_{\mathrm{nano}} + 23\left[\mathrm{K^+}\,(\text{15-crown-5})_2\,\mathrm{Cl^-}\right] + 23\mathrm{NaCl} \end{aligned} \tag{4.1}$$

4.1.1 Alkalide Synthesis

Four catalysts were prepared using the alkalide method. The process and analysis of these will be presented in this section. An overview of the catalysts with key parameters can be seen in table 4.1.

Table 4.1: Summary of the different catalysts synthesised by alkalide reduction

Catalyst	Weight [mg]	Pt:RE	Precursor RE [mg]	Precursor Pt [mg]
Gd@Pt	140	5:1	216	25
Y@Pt	83	3:1	129	19
Y@Pt'	60	3:1	90	17
Pt_3Y	125	3:1	187	40

For all the core-shell catalysts the method for synthesis stayed the same, only the co-reduced Pt_3Y had a different procedure.

Method

All work was done in the Ar-filled glovebox using open glass beakers and glass covered magnetic stirrer bars. For Gd@Pt, Y@Pt and Pt_3Y, all solutions were made in volumes of 50 mL THF. In the case of For Gd@Pt, Y@Pt, the RE solution was added to the reducing agent solution over a two minute period under vigorous stirring. After a three minute mixing time the cores of reduced RE metal should have been formed. Then the Pt solution was added over another two minute period after which the reaction was left for 20 minutes. The now Pt covered RE cores was removed from the glovebox, still in solution, and left to passivate. Preparing the Pt_3Y followed the notion that forming the alloy concurrent with reduction of the salts should further favour the reduction. Therefore the precursor solution were mixed together under vigorous stirring after which the alkalide solution was added evenly over a three minute period.

The further process followed that of the other catalysts. The Y@Pt' catalyst differed by following the recipe from Yan *et al.*, with 100 mL solvent volumes, otherwise the procedure was as for the rest of the RE@Pt.

Characterisation

A small aliquot of the Gd@Pt solution was diluted by a factor of four with Millipore® before being drop-casted on a holey carbon Cu grid for STEM analysis. Representative STEM images of this catalyst can be seen in figure 4.2. From figure 4.2a it would seem that the particles are crystallites of 1 nm to 5 nm or composites thereof in non spherical configurations. What could appear as noise in the image is in fact individual Pt or Gd atoms diffusing around on the grid. Looking at figure 4.2b we see the crystalline nature of the nanoparticles, however, there is no sign of a core-shell structure as the mass contrast should yield a 50 % difference in intensity between the two elements.

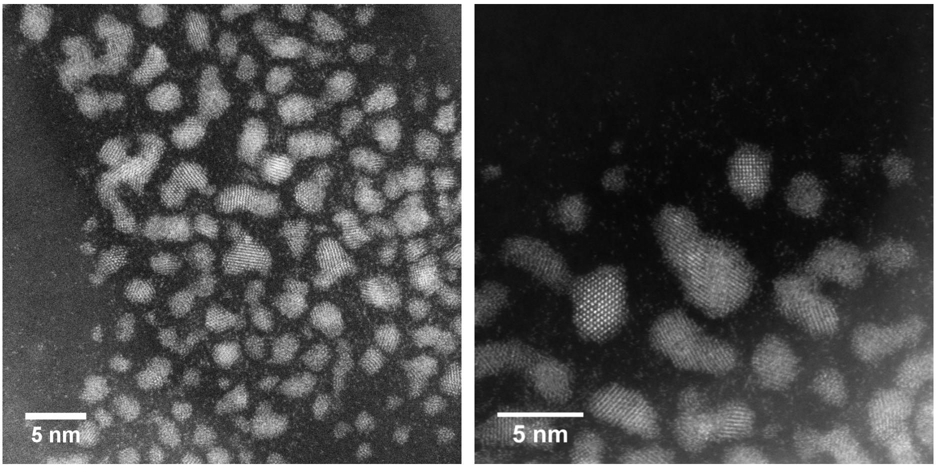

(a) STEM overview image of Gd@Pt **(b)** STEM closeup image of Gd@Pt

Figure 4.2: (a) Representative overview STEM image of Gd@Pt showing particles with sizes predominantly below 5nm **(b)** Representative closeup STEM image of Gd@Pt revealing high crystallinity without the expected core-shell structure

The same trend is confirmed from XRD on the as prepared catalyst and a sample annealed to 600 °C in H_2 (Scientific N6.0, AGA) in-situ in an Anton-Paar furnace coupled to the XRD-stage, see figure 4.3. At this temperature the Gd should be mobile in the Pt as shown by Ulrikkeholm *et al.*[129] The use of H_2 was mainly to avoid oxidation by maintaining a reducing atmosphere. Prior to annealing, only features associated with Pt are visible and after annealing new features show up, however, they correspond to those seen for Gd_2O_3. For the as prepared sample two phases of Pt were needed to achieve a low residual in the Rietveld analysis. One shows a crystallite size of 4.1 nm and one with a crystallite size of 9.6nm and with preferred [111] orientation. These observations agree with the shapes observed on figure 4.2 and similar images. After annealing the profile can be fitted by a single Pt phase with crystallites of 12 nm without preferred orientation.

The same trend was seen for all other samples as well. Re-examining the data published by Yan *et al.* reveal a possible explanation. While they never show clear proof of the metallic state of Gd, besides claiming an unpublished nanostructure for Gd, a clear omission from their part was the identification of Si in their sample. From their EDS measurements a peak is clearly seen at 1.7 kV without any labelling. This energy is the main line for Si K_α. At the same time they identified a major line for Gd which lies on top of Cu, that is one of the most common grid materials for TEM analysis and they do not state which grid type they use and it could then potentially be a Cu and not Gd. Even though the alkalide complex show great promise as a reducing agent and theoretically is able to reduce the RE's, this method was abandoned without further optimisations attempted as more promising methods were prioritised.

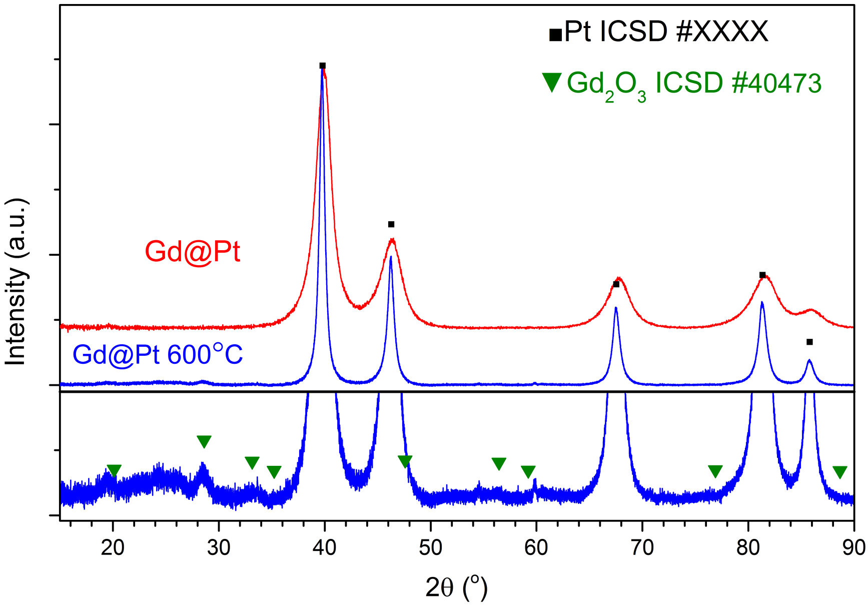

Figure 4.3: XRD of the Gd@Pt as prepared and annealed to 600 °C in-situ.

4.2 Cathodic Corrosion

Koper and co-workers have demonstrated that cathodic corrosion is capable of producing nanoparticles from many elements of varying reduction potential.[165,189] They have also shown that the method can produce alloy particles that retain the composition of the seed crystal[166] and argue that the mechanism behind this particle formation is metal anions formed in a water-free layer over the electrode. These anions are stabilised by alkali and alkali earth cations that need to be present in the electrolyte for the process to occur. Upon contact with water the anions oxidise to their zero oxidation state and form the nanoparticles.[165,190] The nanoparticles form under the strong cathodic potential, but remain anchored to the surface. An anodic pulse releases them into solution, however, this pulse does not need to reach positive potentials to release the particles. Recently it was demonstrated how alloys could also be formed from a seed Pt crystal and ions of the solute metal in solution.[164] For these reasons cathodic corrosion was tested as a method to produce Pt_xY nanoparticles.

4.2.1 Cathodic Corrosion Synthesis

While no Pt_xY wire was available, shards from a broken alloy target were used instead. The metallic state of Y in these shards was confirmed by XPS as seen in figure 4.4. Here the measurement for the shards used for cathodic corrosion, figure 4.4a, is compared to that of XRD verified Pt_3Y, figure 4.4b.[117] There are two metallic phases of yttrium; one for the $Y3d_{5/2}$ at 156.1 eV and a low binding energy phase for the $Y3d_{5/2}$ at 155.1 eV. While the first phase is in line with the average binding energy of metallic yttrium established internally in our laboratory (156.14 eV ± 0.18 eV), the other one is only seen in the bulk of polycrystalline Pt_3Y. Both acidic and alkaline electrolyte was used in this work, $HClO_4$ and NaOH ($\geq$ 99.5 %, Merck EMSURE®) respectively. For acidic synthesis, $NaNO_3$ ($\geq$ 99 % VWR Chemicals, GPR RECTAPUR) was used as cation source. $YCl_3 \bullet xH_2O$ (99.99 %, Alfa Aesar, REacton®) was also used in instances where a pure Pt wire was used (99.99 %, chemPUR 0.25 mm diamter). As counter electrode, either a Pt coil or graphite rod was used ($<$ 2 ppm impurities, TED PELLA, Spec-Pure).

Method

All experiments were carried out in open PFA beakers as two electrode experiments. The counter electrode was separated from the working electrode with a PTFE tube with a Nafion membrane as contact between the two compartments. Both potentiostatic and square-wave potential were used as well as varying electrolyte concentration. In all cases the process was run by a Bio-Logic VMP2 potentiostat using the EC-Lab Express firmware.

Figure 4.5 shows the setup used for the cathodic corrosion with the Pt_3Y shard as WE and here a graphite rod as CE/REF. The shards used for the cathodic corrosion can be seen on figure 4.5b. The shards are mounted in a hanging configuration, keeping the exposed area as small as possible. The area that was immersed can be recognised by the dark colour.

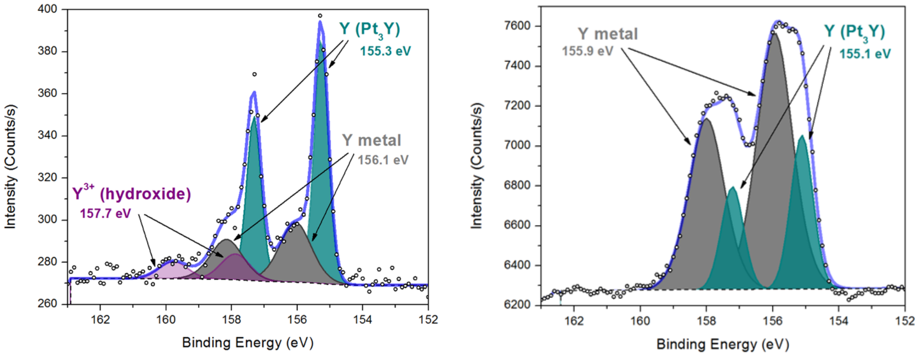

(a) XPS of Y 3*d* for Pt_3Y shard

(b) XPS of Y 3*d* for polycrystalline Pt_3Y from MaTeck

Figure 4.4: (a) Y 3*d* for shard of Pt_3Y target. Points are the recorded signal, blue line is the envelope of the three identified species; Y specific for Pt_3Y (turquoise), metallic Y (grey) and hydroxide (purple) **(b)** Y 3*d* for polycrystalline Pt_3Y disc, the same designations apply here. Both figures were made by Paolo Malacrida CINF-DTU.

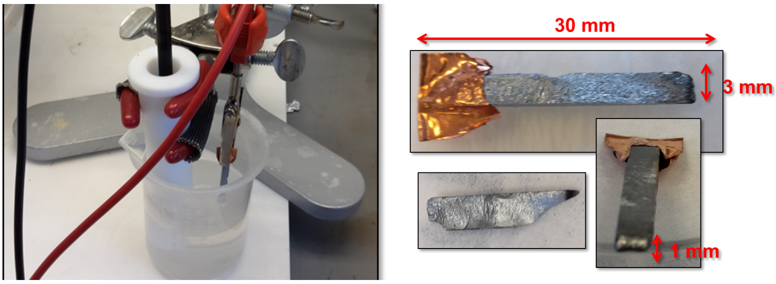

(a) Cathodic corrosion setup

(b) Shards of Pt_3Y used for cathodic corrosion

Figure 4.5: (a) Setup for cathodic corrosion with working electrode (Pt_3Y shard) in PFA beaker and counter electrode in separate tube with Nafion membrane **(b)** Images of the Pt_3Y shards used, the area that was immersed turned dark

Characterisation

Applying a square-wave potential between a Pt wire and the graphite rod going from 0 V to −10 V vs. CE with a frequency of 100 Hz in 1 M NaOH produce a steady stream of free flowing nanoparticles. A TEM image of these particles can be seen on figure 4.6a, where the unsupported particles have agglomerated. the particle in the middle show the fringes of the (111) lattice planes of Pt with an inter-planar distance of 2.28 Å, it is also seen how the electrons are scattered on the amorphous carbon that covers the surface of the particle, contributing

to the contrast in image.
This particle formation does not happen for the Pt_3Y shard. When applying the square-wave potential, the surface darkens as seen on figure 4.5b. This colour stems from an increase in surface area and was confirmed from cycling in shard in 0.1 M $HClO_4$ before and after the square-wave potential treatment. If the potential is instead kept at -10 V vs. CE, the shards starts to delaminate into the "micro" particles seen on figure 4.6b.

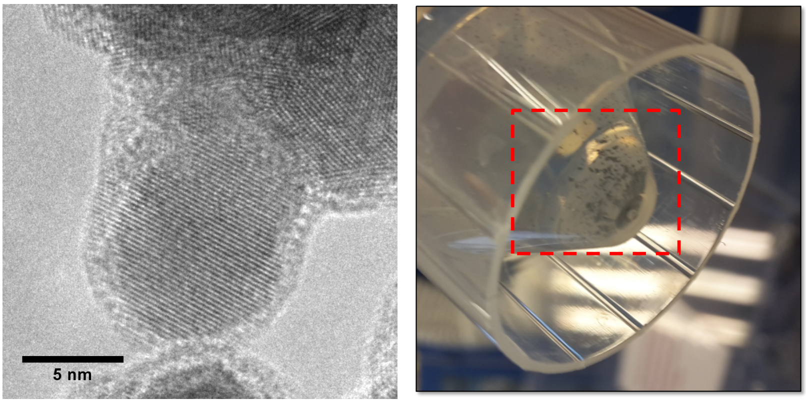

(a) Pt nanoparticles from cathodic corrosion in 1 M NaOH

(b) "Micro" particles formed from cathodic corrosion of Pt_3Y

Figure 4.6: **(a)** TEM image of Pt nanoparticles formed by cathodic corrosion in 1 M NaOH **(b)** Image of the "micro" particles formed from cathodic corrosion of Pt_3Y shards under potentiostatic conditions

While these "micro" particles retain the composition of the shard they originate from, as determined by XPS, they are not useful as electrocatalysts. Instead adopting the method reported by Bennet *et al.* cathodic corrosion of a Pt wire in 0.1 M $HClO_4$ with 0.5 M YCl_3 and 5 M $NaNO_3$ was attempted.[164] Here nanoparticles were formed as for the pure Pt wire. The particles were collected by centrifugation followed by washing with Millipore water. These particles were compared to Pt particles produced in 10 M NaOH and Pt particles prepared in 0.1 M $HClO_4$ with 5 M $NaNO_3$ without the YCl_3.
Figure 4.7 shows the recorded XRD pattern of the three samples prepared by cathodic corrosion of a Pt wire. The control particles prepared in NaOH show a multi-modal profile with preferred orientation along the [111] direction. Two phases with crystallite sizes of 10.5 nm and 57.6 nm respectively were fitted through Rietveld analysis. The particles prepared in $HClO_4$ are similar albeit the small amount of product recovered yielded very low count rates.

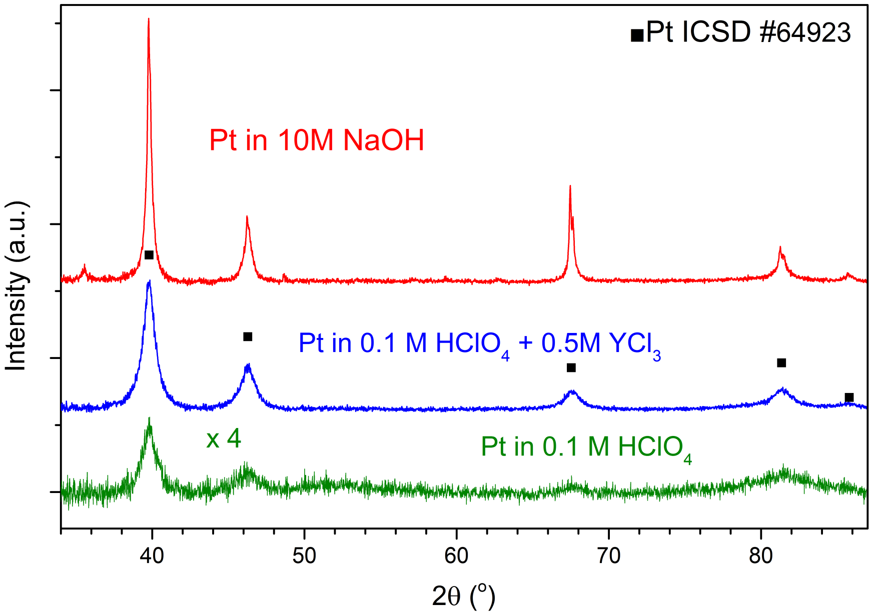

Figure 4.7: XRD pattern of the nanoparticles prepared by cathodic corrosion. Pt in 0.1 M $HClO_4$ (green), Pt in 0.1 M $HClO_4$ + 0.5 M YCl_3 (blue) and Pt in 10 M NaOH (red).

The particles prepared in the presence of YCl_3 only show features from pure Pt, with no additional features that would clearly show the presence of an intermetallic alloy. The presence of yttrium in the particles could also manifest itself as a solid solution. However, this would lead to gradual shifts in the peak positions, as the lattice would expand due to the larger atomic radii of yttrium. Analysing the profile, two phases were used with a minor phase oriented along the [111] direction with a crystallite size of 15.4 nm and a majority phase of particles without a preferred orientation and a crystallite size of 6.3 nm. The multiple phases needed to describe the catalyst particles are not indicative of multiple particle sizes, more the possibility of preferential growth during the formation process or orientation specific stacking when the sample was deposited for XRD measurements. The sizes estimated through Rietveld analysis are in line with observations done by Yanson *et al.* on particle size as function of electrolyte concentration.[167,191]

Despite the lack of evidence of alloying, the catalyst prepared in the presence of YCl_3 showed a higher specific activity than expected for pure Pt particles of the same size, see figure 4.8. Due to the low mass produced during synthesis ($<$ 5 mg) uncertainty on the mass on the electrode prohibited mass activity assessment. The Pt black used for comparison were specified to be $<$ 50 nm (Aldrich, $<$ 50 nm from TEM). At 3 $mA\,cm^{-2}$, the specific activity is 50 %

higher than what could be expected for bulk polycrystalline Pt under equal conditions.[135] With no clear explanation for why this was the case the catalyst was examined with XPS in order to determine if yttrium was present at doping levels. These measurements were done on the sample after electrochemistry.

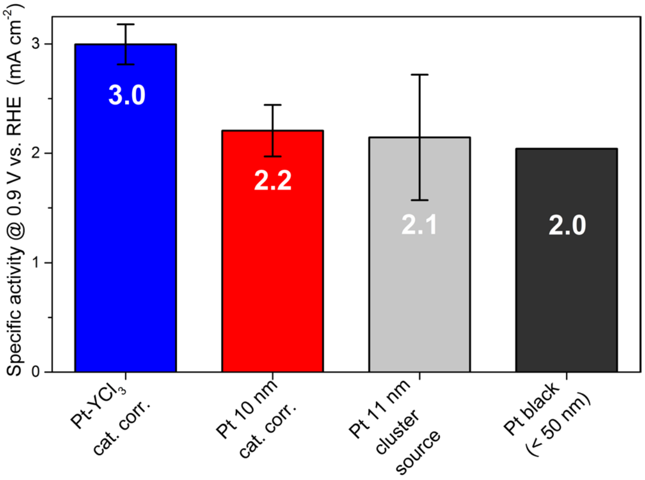

Figure 4.8: Specific activity for catalysts prepared by cathodic corrosion. Catalyst prepared in the presence of YCl_3 show higher activity than expected for Pt nanoparticles (blue). Here compared to reference cathodic corrosion particles (red), commercial Pt black (black) and 11 nm Pt particles from [71]. All areas evaluated by CO-stripping and CVs were corrected for ohmic drop before evaluation. Error bars on the cathodic corrosion samples are derived from three separate measurements

Looking at figure 4.9a the Pt $4f$ line for the catalyst can be seen. Here the binding energy of the $4f_{7/2}$ is 71.28 eV which is within the reported values from United States National Institute of Standards and Technology (NIST) ranging from 70.6 eV to 71.3 eV for metallic Pt.[192] While no evidence for the presence of Y was provided by XRD, Y is present in the catalyst even after electrochemical measurements. The Y $3d$ spectra recorded can be seen in figure 4.9b, here the measured signal is marked by the open circles. While there is no clear separation of the $Y3d_{5/2}$ and $Y3d_{3/2}$ lines, fitting the profile with three doublet phases results in the envelope seen in grey. The phase with the lowest binding energy for $Y3d_{5/2}$, at 155.0 eV (blue), matches with that seen for polycrystalline Pt_3Y. At 156.12 eV the second phase of $Y3d_{5/2}$ is found (green). This value is in line with the average for metallic yttrium measured in our laboratory. The third phase for $Y3d_{5/2}$, is at 156.9 eV (purple) and falls within the NIST range of values for the oxide at 156.4 – 158.6 eV and cant most likely be ascribed to this. The final phase can also be ascribed to the oxide species. The ratio of Pt:Y is 48.6 when only including the metallic phases of yttrium.

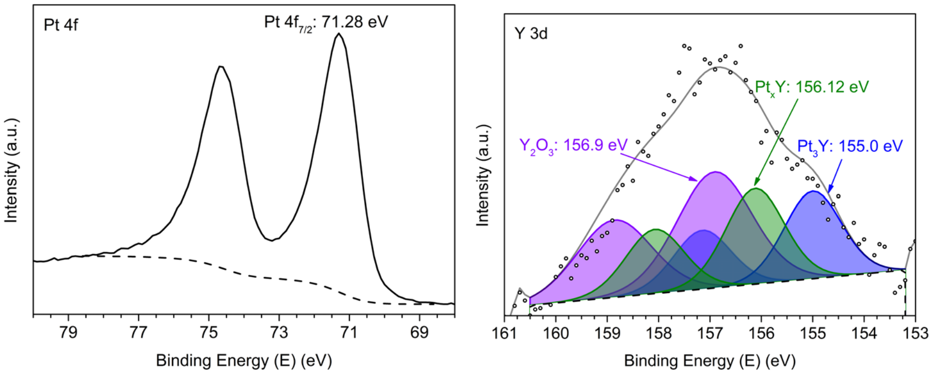

(a) XPS of Pt 4*f* for cathodic corrosion of Pt wire

(b) XPS of Y 3*d* for cathodic corrosion of Pt wire

Figure 4.9: **(a)** Pt 4*f* for the Pt prepared in the presence of YCl_3. **(b)** Y 3*d* for the same catalyst, points are the recorded signal, grey line is the envelope of the three identified species; Y specific for Pt_3Y (blue), metallic Y (green) and oxide (purple)

While the method does show signs of enabling higher activity than expected for Pt nanoparticles, the reason for this is not fully understood. The increased activity could come from faceting of the particles during the cathodic corrosion, however, TEM imaging is needed to investigate this. If actual alloying does take place, the effect is small enough to not be detectable with XRD and so far there is no evidence that point to these alloys forming solid solution that would not show up as additional features in XRD. Further work into the conditions for cathodic corrosion could shed light on the viability of the method. Changing the electrolyte to one without water and examining other cations with a higher reduction potential than yttrium would be interesting. If the proposed mechanism is correct, these cations could enhance the reduction of yttrium as the Pt anions would be more likely to donate their electron to Y if this is the less electropositive element present.

4.3 High Temperature Reduction

This method is based on the work done during the thesis work of my Master thesis.[134] Here thermal reduction of an organometallic precursor was explored as a path for synthesising the desired Pt_3Y and Pt_5Y alloys in nanoparticulate form.[134] The idea was to modify an existing Pt/C catalyst with yttrium through thermal decomposition and reduction of the yttrium precursor. This impregnation of already prepared Pt/C was chosen as co-reducing the two metals thermally deemed unlikely as their reduction potentials are too far apart at

−2.37 V and 1.18 V for Y and Pt respectively.[193]
While the results were never conclusive, there were indications of reduction of the yttrium precursors: There was still yttrium in the catalysts after washing in $HClO_4$ at 60 °C, as confirmed by X-ray fluorescence spectroscopy (XRF). Multiple phases were needed to describe the features observed during XPS analysis, with the lowest binding energy phase was found to be at 156.4 eV for the $Y3d_{5/2}$. There were however, no additional peaks in the XRD patterns of the prepared catalysts. The electrochemical measurements also revealed that the electrochemical surface area was significantly reduced, with no improvements in specific activity. As a consequence the mass activity dropped dramatically from the initial Pt/C catalyst.
To check the feasibility of the synthesis route, experiments were designed together with Christoffer Mølleskov Pedersen from CINF. As for the work in my Master thesis the experiments were carried out using an organometallic precursor; tris(cyclopentadienyl)-yttrium(III), YCp3, ($Y(C_5H_5)_3$, 99.9 %, Sigma-Aldrich, anhydrous). We also tested another yttrium precursor, namely the anhydrous YCl_3 used for the alkalide reduction. As mentioned in chapter 3 the groups of Erdmann and Bronger have shown that the alloys can be formed by thermal reduction of oxides and fluorides.[142–144] With chlorides expected to offer lower reduction temperatures in general,[134] we had anticipated that reduction of the YCl_3 would occur at lower temperatures than observed for the fluorides. To simplify the system, compared to the one used during my Master thesis, no solvent was used to disperse the precursor and the carbon supported catalyst was exchanged for a platinum black catalyst (HiSPEC1000, Johnson Matthey).

Method

The setup used for the thermal reduction was based on the one used during my Master thesis work and the setup is shown in figure 4.10a.[134] It consists of two gas bottles, each of instrument quality (N5.0 AGA) one containing Ar and the other H_2. These are connected with two three way valves to a Schlenk line that allowed for changing between gas and vacuum that was generated by an rotary vane pump (Duo 5M from Pfeiffer Vaccum). The H_2 was connected to allow for direct inlet to the reactor in order to force the H_2 through before, and during reduction. The exhaust of the Schlenk line was connected to an oil trap filled with silicone oil to prevent back diffusion of O_2 and H_2O. All tubing used for connections was made of Tygon S3 (Food grade, SAINT-GOBAIN). The reactor was made from quartz and consists of a top cross with inlet on one side connected to an inner tube and exhaust on the opposite side. All three inlets/outlets of the top part had PTFE valves for sealing the reactor of. The bottom part was shaped like a standard test tube, however, with grind cuts to connect to the top. To seal the reactor for synthesis, Glindemann PTFE sealing rings were used. Each of the yttrium precursors had their own bottom half of the reactor to keep the systems separate. All handling of precursors prior to synthesis was done inside the glovebox mentioned for the alkalide reduction. Prior to synthesis work the Pt black catalyst was dried at 200 °C for one hour in H_2 to remove any adsorbed water and reduce any surface oxides. While the volume of the catalyst diminished during the this process and as such surface area was lost, the purpose of the experiments was only to verify the possible path for synthesis and therefore the final particle size was not a priority. When the catalyst had reached room temperature the gas was exchanged to Ar and the sealed reactor transferred to the glovebox.

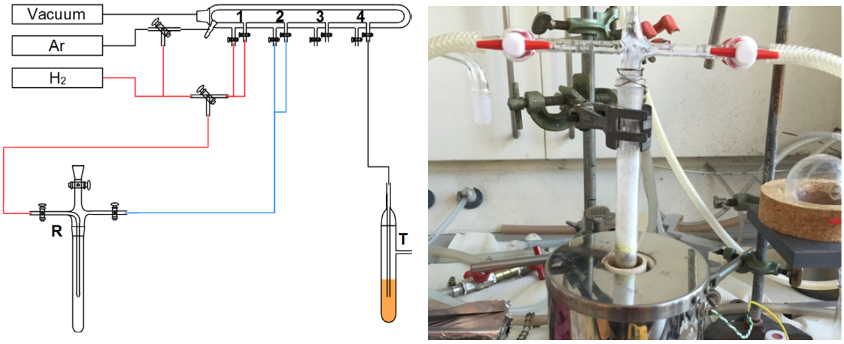

(a) Setup used for high temperature reduction **(b)** Image of the reactor in furnace

Figure 4.10: **(a)** Diagram of the setup for high temperature reduction. The reactor is marked by **R** and the oil trap is marked by **T** **(b)** Image of the reactor in the furnace during synthesis. Reproduced from Christoffer Pedersen [194]

The precursors were mixed inside the glovebox using a mortar with mixing ratio, by weight, of 1:3 for Pt:Y. Once mixed to a uniform powder, the precursor mixture was sealed in the reactor and connected to the setup. Here the connections were evacuated and refilled with Ar three times before opening to H_2. The system was then flushed with H_2 before starting the annealing process. Here the two precursors had different treatments: The YCl_3 precursor was heated to 900 °C from room temperature in 90 minutes and kept there for 360 minutes for the reduction. Hereafter the reactor was left to cool naturally to room temperature. For the YCp3 the reactor was heated from room temperature to 200 °C in 20 minutes and kept there for 60 minutes. The temperature was then raised to 900 °C over 70 minutes, here it was kept constant for 60 minutes. Finally the temperature was lowered to 500 °C for 30 minutes before cooling naturally to room temperature. The final step at 500 °C was a legacy step in the annealing procedure from the work during my Master thesis and was kept for consistency of annealing profile with earlier experiments. The idea was to slowly decompose/react the organometallic precursor on the surface of the Pt/C at the 200 °C with subsequent alloying at 900 °C. As the chloride would not decompose at the lower temperature step of the organometallic precursor temperature profile, this step was omitted. When the reactor reached room temperature the gas was again switched to Ar before the reactor was opened to air and left to pacify the surface of the catalyst. From here the catalyst material was characterised and the results of this will be presented in the following sections.

4.3.1 High Temperature Reduction of YCp3

During the synthesis of Pt_xY from the YCp3 precursor sublimation of the precursor appeared as a yellow-green deposit just above the edge of the furnace as seen on figure 4.10b. Lightly tapping on the reactor during the reduction loosened the deposits and it dropped to the bottom and melted. This process was repeated until the annealing program finished.
Upon removing the product from the reactor small lumps were observed next to the powder catalyst. These lump were extracted and analysed separately by XPS and showed only the presence of Y and C with a binding energy for $Y3d_{5/2}$ at 157.5 eV. This was ascribed to a yttrium carbide species. The rest of the powder was first characterised by XRD. Figure 4.11 shows the patterns recorded for the sample reduced with YCp3 (blue), the pristine HiSPEC 1000 catalyst (red) and polycrystalline Pt_3Y from (green).[116,117] Comparing the synthesised catalyst with that of Pt black it is clear that the features of platinum have disappeared from the catalyst (black squares). Instead all features overlap with those observed in the polycrystalline disc used by Greeley *et al.*[116] and Stephens *et al.*[117] Here the main features can be ascribed to that reported in literature for Pt_3Y, symbolised by the inverse green triangles (ICSD #649852). In both of these there are features that cannot be assigned to the Pt_3Y phase. These can best be described by a Pt_2Y phase symbolised by the purple triangles. Overall the XRD pattern reveal close to a clean phase of Pt_3Y. The width of the peaks have decreased significantly and Rietveld analysis of the Pt black catalyst reveal crystallites of 6.9 nm while the synthesised catalyst has crystallites of 67 nm.

Before characterising the catalyst with XPS it was washed in 0.1 M $HClO_4$ to remove the leftover precursor and any oxidised surface layers. Figure 4.12 shows both the Pt $4f$ and the Y $3d$ spectra. The asymmetrical shape of the Pt $4f$ line indicates multiple species and can be described by a metallic phase at 71.2 eV (grey) and what comes closest to a PtO phase at 72.1 eV (red).[192] For the Y $3d$ line the overall spectrum is broad and centered at a high binding energy for yttrium. One small feature is present below 156 eV and corresponds to the binding energy of yttrium in Pt_3Y at 155.3 eV (blue). The rest of the feature is explained by an oxidised phase at 156.6 eV (red) and a carbide at 157.9 eV (grey). The carbide is the dominant phase from XPS, however, the XRD did not reveal any significant features that could be identified as a crystalline carbide

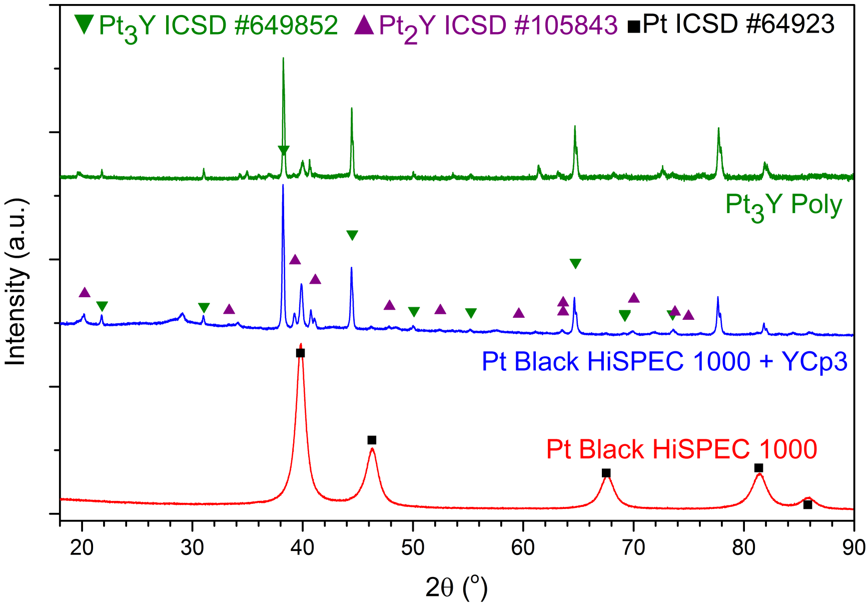

Figure 4.11: XRD pattern of the nanoparticles prepared by high temperature reduction of YCp3. Shown are the measured catalyst (blue), Pt black HiSPEC 1000 (red) and the Pt$_3$Y crystal from [116,117]. The phases that coincide with the pattern are Pt$_3$Y (ICSD #649852), Pt$_2$Y (ICSD #105843) and Pt (ICSD #64923)

phase. To further investigate the catalyst, SEM with EDS was used.

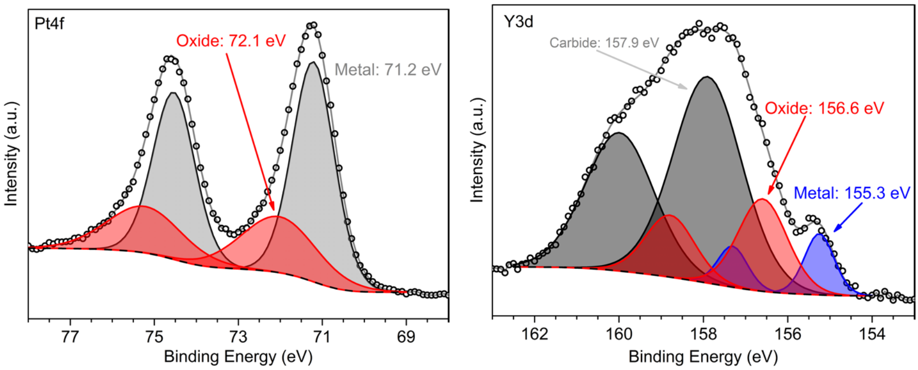

(a) XPS of Pt 4*f* for High temperature reduction of YCp3

(b) XPS of Y 3*d* for High temperature reduction of YCp3

Figure 4.12: **(a)** Pt 4*f*, two distinct phases were identified; metallic at 71.2 eV and an oxide at 72.1 eV **(b)** Y 3*d*, three phases identified the metallic indicative of Pt$_3$Y at 155.3 eV, oxide at 156.6 eV and a carbide at 157.9 eV

The SEM analysis was performed at DTI by Erik Wisaeus and representative images can be seen in figure 4.13. What is seen in both images are large spherical structures of $0.1 - 0.2\ \mu m$ and $1 - 2\ \mu m$. Mixed in with these structures are smaller agglomerates of YC_2, see figure 4.13a. From figure 4.13b it is seen how the larger structures seem to emanate from the smaller agglomerates. No Pt was observed with EDS for the as prepared sample.

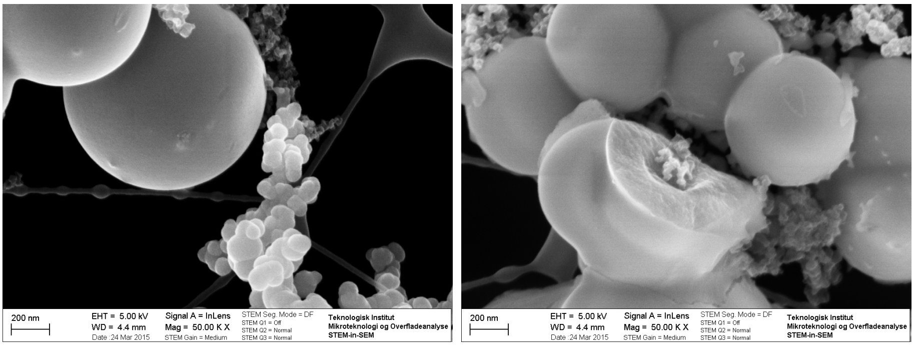

(a) SEM image of as prepared high temperature reduction from YCp3

(b) SEM image of as prepared high temperature reduction from YCp3

Figure 4.13: **(a)** Large spherical structures most likely YC_2 spheres, mixed with smaller agglomerates of YC_2 **(b)**The spherical structures surrounding a small agglomerate of YC_2

Analysing the structures with EDS mapping after acid wash reveal more information, see figure 4.14a. After the acid wash, the oxide species were removed leaving behind only stable structures. A rough structure is seen centrally in the image, surrounding it are the same spherical structures, with the agglomerate in a cavity of these. The rectangle in figure 4.14a is mapped for C $K_{\alpha 1,2}$, O $K_{\alpha 1}$, Y $L_{\alpha 1}$ and Pt $M_{\alpha 1}$ and these maps are shown in figure 4.14b. The carbon is seemingly confined to the outer edges of the map with almost no signal from the central part. Both the Y and the Pt show higher intensities in the region void of C signal. Combining the information from the EDS maps and the topographical information from the SEM image gives an idea of how the process occurs. The YCp3 decomposes on the surface of agglomerated Pt black, however, most of the precursor does not react with the Pt. Instead it decomposes into YC_2 that covers the surface. The alloy formed by the reduction of YCp3 has the right stoichiometry and is close to phase pure, however, the inaccessible surface area lowers its potential as an electrocatalyst. Optimising the reduction conditions could potentially reduce or eliminate the formation of YC_2.

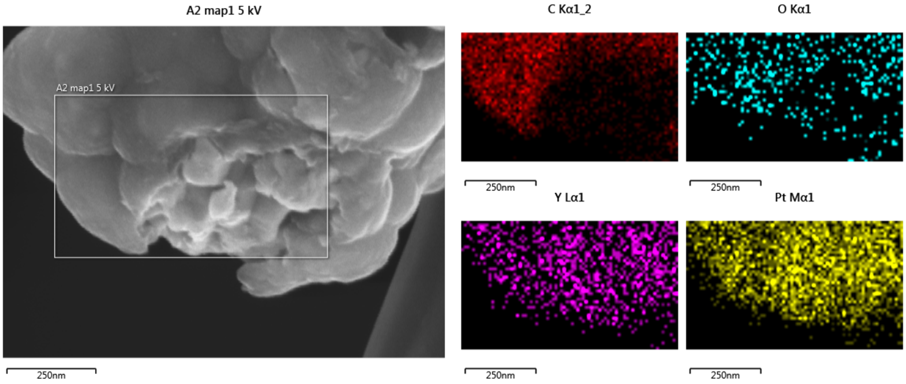

(a) SEM image with area for EDS MAP

(b) SEM EDS maps for C, O, Y and Pt

Figure 4.14: **(a)** SEM image of the catalyst with spherical structure and small agglomerates in the center after acid wash **(b)** EDS maps of C $K_{\alpha1,2}$, O $K_{\alpha1}$, Y $L_{\alpha1}$ and Pt $M_{\alpha1}$ after acid wash

4.3.2 High Temperature Reduction from YCl_3

The catalyst prepared by reduction of YCl_3 came out as a mixture of white powder of surplus YCl_3 and a dark grey powder. Analysing this powder mix with XRD reveals the pattern seen in figure 4.15. Here the features of polycrystalline Pt_3Y are again prominent in the synthesised catalyst. There are many more features besides those for Pt_3Y and these can best be described by yttrium chloride, oxychlorides, platinum silicides and yttrium silicides.[195] As for the other precursor the width of the peaks have decreased significantly indicating agglomeration. The pattern of the synthesised catalyst is, however, so complex that Rietveld analysis did not give any meaningful results.

Analysing the acid washed sample with XPS gives the spectra for Pt $4f$ and Y $3d$ seen in figure 4.16. The features of the Pt $4f$ line were broader than seen for the YCp3 precursor and were best described by three phases; one metallic at 71.1 eV (grey), a PtO at 72.2 eV (red) and a phase at a lower binding energy than pure Pt, 69.8 eV (blue), see figure 4.16a. For the Y $3d$ line an even wider line than for the YCp3 precursor. Here two Yttrium phases were needed to describe the high end of the features of the spectrum. For the low end two Si $2s$ phases were used, as this is the most likely element to describe these energy features. The individual phases are shown in figure 4.16b. For Y $3d_{5/2}$ the binding energies were 155.6 eV for the metallic phase (blue) and 158.7 eV for the an oxidised phase (purple). This is either an oxide or a chloride according to the NIST database.[192]

The two phases needed to describe the low energy region were fitted to be 151.5 eV (dark blue) and 153.9 eV (pink). These were in close agreement with energies observed for various Pt-Si alloys examined by Permyakova.[196] The proposed cause of this alloy formation is a reaction between the YCl_3 and the quartz reactor. This intermediate of Y-Si-Cl-O allows the further reduction of Si that can react with the Pt black.

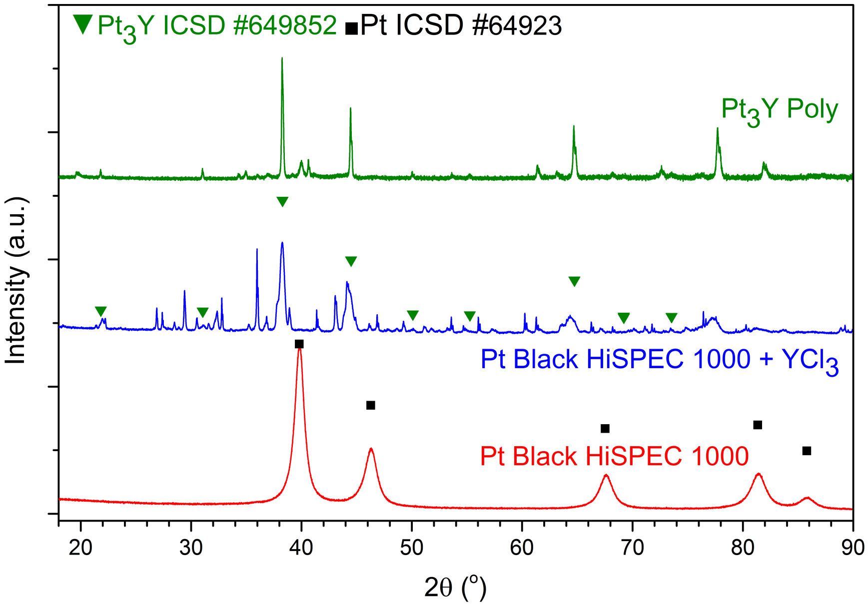

Figure 4.15: XRD pattern of the nanoparticles prepared by high temperature reduction of YCl_3. Shown are the measured catalyst (blue), Pt black HiSPEC 1000 (red) amd the Pt_3Y crystal from [116,117]. The phases that coincide with the pattern are Pt_3Y (ICSD #649852) and Pt (ICSD #64923)

The next section will go into the thermodynamics of the high temperature reduction of the chlorides and oxides to establish the limitations for the alloy formation of Pt-RE alloys from the thermal reduction with H_2.

4.4 Thermodynamics of High Temperature Reduction

The Pt-RE alloys have very negative heats of formation and the theory is that this will provide them with long term stability surpassing that of platinum alloys with late transition metals. On the other hand the REs also form very stable oxides that can pull the reduction reaction towards oxidation instead. This sensitivity towards oxygen and water will be elaborated on during this section. To perform the analysis presented in this section, most of the data had to be gathered from different sources and converted for use in HCS Chemistry 6.1.

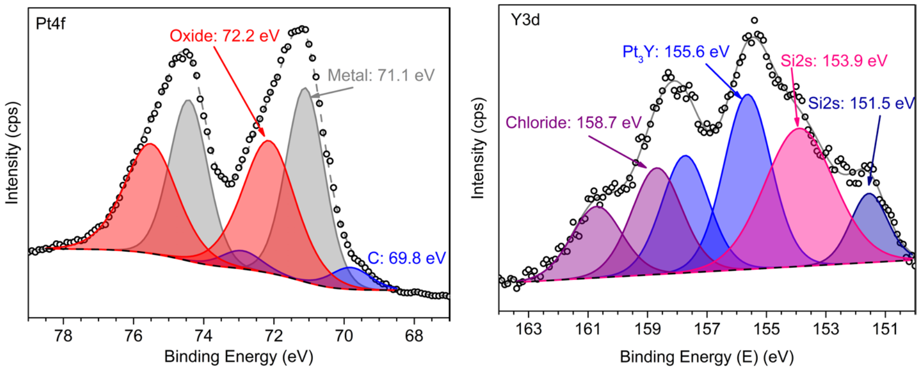

(a) XPS of Pt 4*f* for High temperature reduction of YCl_3

(b) XPS of Y 3*d* for High temperature reduction of YCl_3

Figure 4.16: **(a)** Pt 4*f*, three phases were identified; metallic at 71.1 eV and an oxide at 72.2 eV and a third phase at 69.8 eV **(b)** Y 3*d*, four phases were identified the metallic indicative of Pt_3Y at 155.6 eV, chloride at 158.7 eV and two Si phases at 151.5 eV and 153.9 eV

This work was done by Christoffer Mølleskov Pedersen and section 4.4.1 will go over the process.[194]

4.4.1 Thermodynamic Data and Model

The thermodynamic data for the Pt-RE alloys has preveiously been reported from reduction experiments using the RE oxides and Pt powder in a stream of purified H_2. During the reduction, the partial pressure of H_2O was measured using a galvanic cell. This was then used to calculate the formation enthalpy and formation entropy, by extracting the equilibrium constant from the partial pressure measurment.[197–199] The thermodynamic data acquired through this along with the ranges investigated is listed in table 4.2.
The software used for the thermodynamic calculations was HSC Chemistry (version 6.1) developed by Outotec Technologies. While it contains an internal database with thermodynamic data for more than 28.000 species, the Pt-RE alloys were not included in this. The data needed was therefore added from the sources in literature and include the standard enthalpy of formation.[143,144,197–200] To perform the calculations the program also uses the standard entropy of the materials and the specific heat capacity as a function of temperature. These are not directly available in the reported literature, however, they can be extracted from the published data. The following will present the methodology for used for extracting the data and performing the calculations in HSC Chemistry. All calculations are first evaluated under the assumption that kinetics are insignificant in limiting the reaction. Later the possible influences

of kinetics will be discussed.

Table 4.2: Thermodynamic data for the Pt_xRE alloys.

Alloy	$T_{Reduction}$ [K]	ΔH [kJ/mol]	ΔS [J/(mol K)]	T_{Range} [K]	Ref
Pt_5Y	1200	-385.97	-5.4	1100-1600	[197,198]
Pt_3Y	1350	-386.83	-19.6	1300-1700	[197,198]
Pt_5Gd	1200	-438	-51	1073-1373	[197,199]
Pt_2Gd	1400	-412	-60	1373-1673	[197,199]
Pt_5Tb	1200	-442	-44	1073-1373	[197,199]
Pt_3Tb	1300	-425	-46	1273-1573	[197,199]
Pt_5Ca	1200	-231.5	-25.5	1200-2133	[200]

The reaction carried out in the relevant literature is seen in equation 4.2.

$$x\mathrm{Pt} + \frac{1}{2}\mathrm{M_2O_3} + \frac{3}{2}\mathrm{H_2(g)} \rightleftharpoons \mathrm{Pt}_x\mathrm{M} + \frac{3}{2}\mathrm{H_2O(g)} \tag{4.2}$$

Here M, denotes the alloying elements and x indicates the alloy stoichiometry. When the reaction is in equilibrium, the equilibrium constant, K can be written as

$$K = \left(\frac{P_{\mathrm{H_2O}}}{P_{\mathrm{H_2}}}\right)^{\frac{3}{2}} \tag{4.3}$$

The equilibrium constant can also be written in terms of the change in Gibbs free energy for the reaction[42]

$$K = e^{-\frac{\Delta_r G}{RT}} \tag{4.4}$$

Here R is the gas constant, T is the temperature and $\Delta_r G$ is the change in the Gibbs free energy for the reaction. This change can also be calculated from the following

$$\Delta_r G = G_{\mathrm{Pt}_x\mathrm{M}} + \frac{3}{2}G_{\mathrm{H_2O}} - \left(xG_{\mathrm{Pt}} + \frac{1}{2}G_{\mathrm{M_2O_3}} + \frac{3}{2}G_{\mathrm{H_2}}\right) \tag{4.5}$$

Here the Gibbs free energy for the alloy and the other compounds can be written by the elemental Gibbs free energies.

$$\Delta G_{\mathrm{H_2O}} = G_{\mathrm{H_2O}} - \left(G_{\mathrm{H_2}} + \frac{1}{2}G_{\mathrm{O_2}}\right) \tag{4.6}$$

$$\Delta G_{\mathrm{M_2O_3}} = G_{\mathrm{M_2O_3}} - \left(2G_{\mathrm{M}} + \frac{3}{2}G_{\mathrm{O_2}}\right) \tag{4.7}$$

$$\Delta G_{\mathrm{Pt}_x\mathrm{M}} = G_{\mathrm{Pt}_x\mathrm{M}} - (G_{\mathrm{Pt}} + G_{\mathrm{M}}) \tag{4.8}$$

Substituting these expression into equation 4.5 and reducing gives the following for the Gibbs free energy of the reaction.

$$\Delta_r G = \Delta G_{\mathrm{Pt}_x\mathrm{M}} + \frac{3}{2}\Delta G_{\mathrm{H_2O}} - \frac{1}{2}\Delta G_{\mathrm{M_2O_3}} \tag{4.9}$$

With $\Delta_r G$ measured at different temperatures and table values for $\Delta G_{\mathrm{H_2O}}$ and $\Delta G_{\mathrm{M_2O_3}}$ it is possible to determine change in Gibbs free energy for the alloy as function of temperature. This was done in the published studies on the thermal reduction of the oxides with platinum powder and here a linear relation between temperature and $\Delta_r G$ was reported in the investigated temperature range. This means that the formation enthalpy and formation entropy are constant in the temperature range investigated and can be extracted from equation 4.10.

$$\Delta G_{\mathrm{Pt}_x\mathrm{M}} = H_0 - TS_0 \tag{4.10}$$

Expanding equation 4.8 with that of 4.10 and writing it out in terms of enthalpy and entropy it is possible to write two equations; one for the enthalpy of the alloy and one for the entropy of the alloy respectively.

$$H_{\mathrm{Pt}_x\mathrm{M}} = H_0 + xH_{\mathrm{Pt}} + H_{\mathrm{M}} \tag{4.11}$$

$$S_{\mathrm{Pt}_x\mathrm{M}} = S_0 + xS_{\mathrm{Pt}} + S_{\mathrm{M}} \tag{4.12}$$

The standard enthalpy is then H_0 as both H_{Pt} and H_{M} are zero for standard conditions. The standard entropy can be calculated using equation 4.12 with table values of S_{Pt} and S_{M} for standard conditions (25 °C).

As mentioned the program also uses the temperature dependent specific heat capacity. This can be written as below for a constant pressure P

$$C_P = T\left[\frac{dS}{dT}\right]_P \tag{4.13}$$

The specific heat capacity for the relevant alloy can the be calculated using the database values for $S_{\mathrm{Pt}}(T)$ and $S_{\mathrm{M}}(T)$ inserted into equation 4.12. The software uses the function in equation 4.14 to describe the specific heat capacity. By fitting this function to the calculated data the last parameters for the software was determined.

$$C_P(T) = A + 10^{-3}BT + 10^{5}CT^{-2} + 10^{-6}DT^{2} \tag{4.14}$$

To ensure the validity of the fitted data and the thermodynamic module in HCS Chemistry, the program calculated data was compared to the experimental data and found to be in good agreement.[194]

The temperature range over which the calculated change in Gibbs free energy is valid can be discussed. While the experimental data that form the foundation of the calculations is in a temperature range of ca. 800 °C – 1800 °C the temperature range of interest is that from 400 °C – 1000 °C. There is an overlap of the ranges for some of the elements, however, the interesting low end of the temperature range can only be evaluated by extrapolating the trend to lower temperatures than used for the determination of the data used for the fitting. However, there are no indications that anything should suddenly change dramatically as no phase transitions occur for any of the components in this extended low end temperature range.

4.4.2 Alloying from Oxides

The reduction of the RE oxides together with Pt will be examined first. These will serve as models for the general condition needed for alloying to take place. Almost all the REs are promising electrocatalysts when alloyed with Pt.[119] In this section the focus will be on Y as a model reaction, it was chosen as it was the main alloying element for the synthesis work. At the end of the section the the observations will be extended to the rest of the RE elements.
The reduction of the oxides together with platinum can be written in a generalised way as

$$x\mathrm{Pt} + \frac{1}{2}\mathrm{M}_y\mathrm{O}_z + \frac{z}{y}\mathrm{H}_2(\mathrm{g}) \rightleftharpoons \mathrm{Pt}_x\mathrm{M} + \frac{z}{y}\mathrm{H}_2\mathrm{O}(\mathrm{g}) \tag{4.15}$$

With M denoting the RE elements. This equation accommodates the presence of other oxides than the common M_2O_3. The change in Gibbs free energy for this type of reaction with Y can be seen in figure 4.17a with the free energy normalised per mole of Pt_xY. From this it would seem that the formation of Pt_3Y is the least preferred (blue line) with Pt_5Y being marginally more favourable (red line). The conversion from Pt_5Y to Pt_3Y is the most favourable when normalising to the moles of alloy formed. If the reactions instead are normalised to the moles of H_2O produced during the reaction the ordering of the alloys change, see figure 4.17b. Now Pt_5Y is the reaction that will be the preferred one of the three, followed by the formation of Pt_3Y and finally the change from Pt_5Y to Pt_3Y. All changes in Gibbs free energy are positive over the whole temperature range from 20 °C – 1400 °C. Therefore none of the reactions will proceed when in equilibrium. By equation 4.4 the equilibrium constant can be determined as function of temperature. Relating the calculated equilibrium constant to that for the gas phase equilibrium constant yields the partial pressure of H_2O in equilibrium.

$$K = \left(\frac{P_{\mathrm{H_2O}}}{P_{\mathrm{H_2}}}\right)^{\frac{z}{y}} \Longleftrightarrow \frac{P_{\mathrm{H_2O}}}{P_{\mathrm{H_2}}} = K^{\frac{y}{z}} \tag{4.16}$$

This equilibrium partial pressure of H_2O is plotted for the three Pt-Y reactions in 4.18a. Here the equilibrium partial pressure is plotted on a logarithmic scale as a function of the temperature.

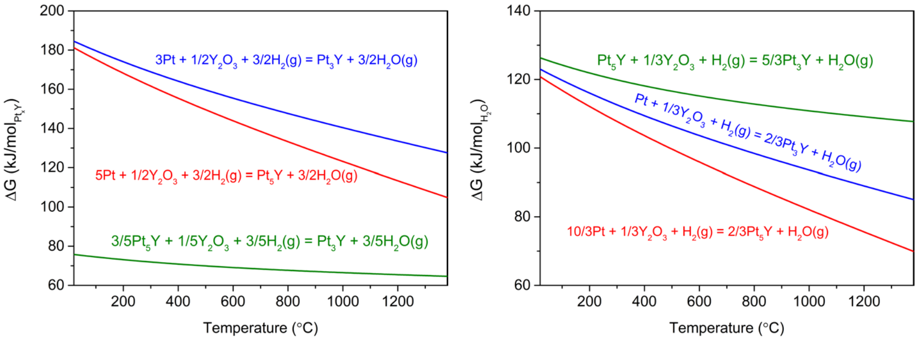

(a) ΔG normalised per $\text{mol}_{\text{Pt}_x\text{Y}}$ **(b)** ΔG normalised per $\text{mol}_{\text{H}_2\text{O}}$

Figure 4.17: ΔG for the reduction of Y_2O_3 to Pt_5Y (red), Pt_3Y (blue) and conversion of Pt_5Y to Pt_3Y (green) with different normalisations **(a)** normalised per $\text{mol}_{\text{Pt}_x\text{Y}}$ and **(b)** normalised per $\text{mol}_{\text{H}_2\text{O}}$

For any partial pressure of H_2O above the red line for Pt_5Y, the oxidation of any alloy material will occur. At a partial pressure in the red area the formation of Pt_5Y can take place and in the blue area both Pt_5Y and Pt_3Y can be formed. In the green area, the partial pressure of H_2O is low enough for the Pt_5Y to be converted into Pt_3Y. These equilibrium curves show the tolerance towards H_2O for the different reactions, moreover it shows that the normalisation to moles of H_2O produced is the correct way to gauge how favourable the reactions are. For temperatures below 400 °C the equilibrium partial pressure falls below 1 ppb. This indicates the extreme sensitivity towards water for this reaction.

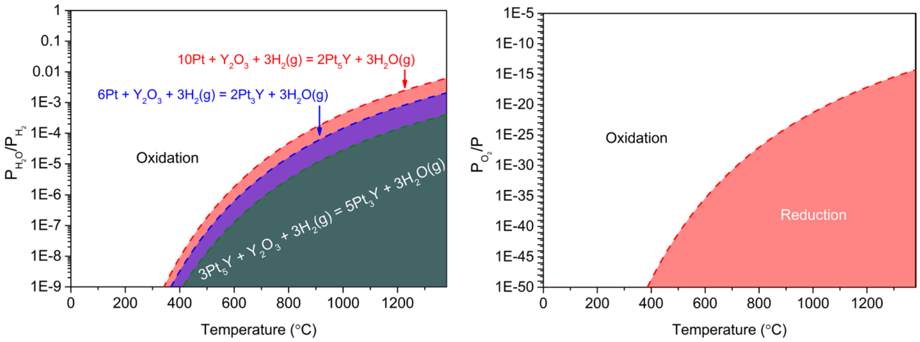

(a) Equilibrium partial pressure of H_2O for Pt_xY alloys

(b) Equilibrium partial pressure of O_2 for Pt_xY alloys

Figure 4.18: Equilibrium partial pressures for Pt_5Y (red), Pt_3Y (blue) and conversion from Pt_5Y to Pt_3Y (green) for **(a)** partial pressure of H_2O and **(b)** partial pressure of O_2

The same analysis can be performed for the alloys tolerance towards oxygen by using the following standard equation for oxidation of the alloys with O_2

$$\mathrm{Pt}_x\mathrm{M} + \frac{z}{2y}\mathrm{O}_2(\mathrm{g}) \rightleftharpoons x\mathrm{Pt} + \frac{1}{y}\mathrm{M}_2\mathrm{O}_3 \tag{4.17}$$

Together with

$$K = \left(\frac{1}{P_{\mathrm{O}_2}}\right)^{\frac{z}{y}} \Longleftrightarrow P_{\mathrm{O}_2} = K^{-\frac{y}{z}} \tag{4.18}$$

This tolerance towards O_2 for Pt_5Y is seen in figure 4.18b. As for the tolerance towards water any partial pressure of O_2 above the line will lead to the oxidation of the alloy and any partial pressure of O_2 below will favour the reduction. It is clear that any relevant and achievable partial pressure of O_2 causes the oxidation of the alloy. Nonetheless the alloy is stable in bulk form; crystals have been kept in air and used for the past eight years in the group at CINF-DTU. The reason lies in the kinetics that so far have been neglected. While there is limited data, studies on the oxidation of the Pt-RE alloys have shown that the onset for oxidation goes from 330 °C – 660 °C.[143] The oxygen is kinetically hindered from penetrating into the bulk at lower temperatures. The reaction with oxygen at elevated temperatures does, however, imply that oxygen present during high temperature reduction will, as a minimum, prolong the time needed for complete reduction.
By forcing the partial pressure of the product gas down the reaction is brought out of equilibrium and the reduction can proceed. The minimum reduction time can then be calculated by evaluating the gas throughput of the synthesis setup. This is done in the absence of kinetic limitations and re-oxidation from trace amounts of oxygen in the reduction gas.

Without kinetic limitations the reaction rate is limited only by removal of product gas. For the mass transport limited case the equilibrium partial pressure illustrated in figure 4.18a will also be the highest partial pressure attainable . The rate of the reaction will then scale with how fast the product gas is removed. This can be expressed as the following

$$P_{\mathrm{H_2O}}V(Q,t) = n_{\mathrm{H_2O}}RT \tag{4.19}$$

$$n_{\mathrm{H_2O}} = \frac{P_{\mathrm{H_2O}}Qt}{RT} \quad , \quad V(Q,t) = Qt \tag{4.20}$$

Here R is the gas constant, T is the temperature, $P_{\mathrm{H_2O}}$ is the equilibrium partial pressure of H_2O, $\mathrm{n}_{\mathrm{H_2O}}$ is the moles of H_2O, V is the volume passing through the reactor with Q being the flowrate and t denoting the reaction time. Coupled with the expression for the moles of alloy formed, $n_{\mathrm{Pt}_x\mathrm{M}}$, the reaction time, t can then be written

$$t = \frac{y}{xz}\frac{w_{\mathrm{Pt}}RT}{m_{\mathrm{Pt}}P_{\mathrm{H_2O}}Q} \tag{4.21}$$

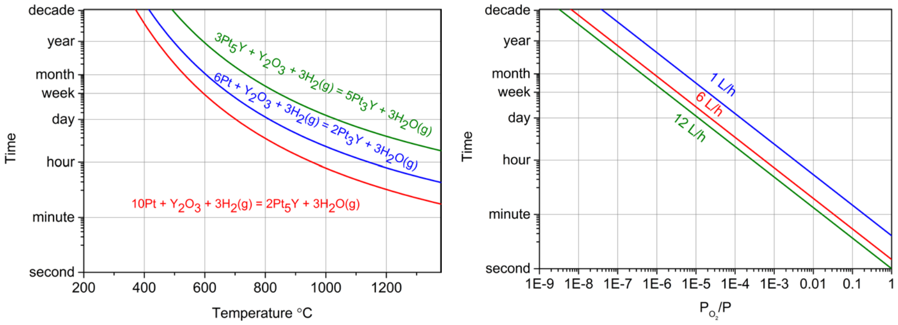

(a) Minimum reduction time for Y_2O_3 reduction to Pt_xY alloys

(b) Time for Pt_5M to oxidise assuming infinitely fast kinetics

Figure 4.19: **(a)** minimum reduction time for Pt_5Y (red), Pt_3Y (blue) and conversion from Pt_5Y to Pt_3Y (green) **(b)** oxidation Oxidation time for Pt_5M alloys with no kinitic limitations

With the internal relation between $\mathrm{n}_{\mathrm{Pt}_x\mathrm{M}}$ and $\mathrm{n}_{\mathrm{H_2O}}$ being

$$\frac{w_{\mathrm{Pt}}}{x m_{\mathrm{Pt}}} = n_{\mathrm{Pt}_x\mathrm{M}} = \frac{z}{y} n_{\mathrm{H_2O}} \tag{4.22}$$

Here w_{Pt} is the weight of Pt used and m_{Pt} is the molar mass for Pt. Figure 4.19a shows the minimum time calculated for the Pt_xY alloys with 0.1 g of Pt at a flow of 6 L/h determined at 25 °C. From this it is seen that thermal reduction of the oxide should be possible already from 800 °C this could possibly open up for the use of oxides as precursor material.

A similar analysis can be done for the oxidation the alloy by the trace amounts of oxygen in the H_2 gas. Assuming all oxygen molecules in the gas react instantaneously, the consumed moles of O_2 can be written

$$n_{\mathrm{O_2}} = \frac{P_{\mathrm{O_2}} Q t}{RT} \tag{4.23}$$

A similar relation as before couple the moles of oxidised alloy to the moles of consumed O_2. This is based on the ratio between the two species in equation 4.17.

$$n_{\mathrm{Ox}} = \frac{z}{2y} n_{\mathrm{O_2}} = \frac{z}{2y} \frac{P_{\mathrm{O_2}} Q t}{RT} t = \frac{2y}{z} \frac{P_{\mathrm{O_2}} Q t}{RT} \tag{4.24}$$

utilising the same expression for $n_{\mathrm{Pt}_x\mathrm{M}}$ as before t becomes

$$t = \frac{2y}{xz} \frac{w_{\mathrm{Pt}} RT}{m_{\mathrm{Pt}} P_{\mathrm{O_2}} Q} \tag{4.25}$$

Three different flow rates, Q, are plotted in figure 4.19b 1 L/h (blue), 6 L/h (red) and 12 L/h (green) respectively. 0.1 g of Pt was used for the calculations and the flow rates are measured at 25 °C. At a flow rate of 6 L/h the calculated times for complete oxidation is more than a week in the range of O_2 content in instrumental 5.0 and scientific 6.0 H_2 which is 2 ppm and 0.5 ppm respectively. As the reduction times used in these studies are less than a day (6-8 hours) and this is the absolute worst case scenario the reduction reaction can be done using oxygen containing hydrogen as shown in the previous section.

Figure 4.20a shows the change in Gibbs free energy of different Pt_5RE alloys, normalised per mol_{H_2O}. All of the interesting lanthanide metals have changes in Gibbs free energy that favour the reduction more than seen for yttrium and therefore they also have higher tolerances for H_2O and O_2. This should make them overall easier to reduce than the Y_2O_3.

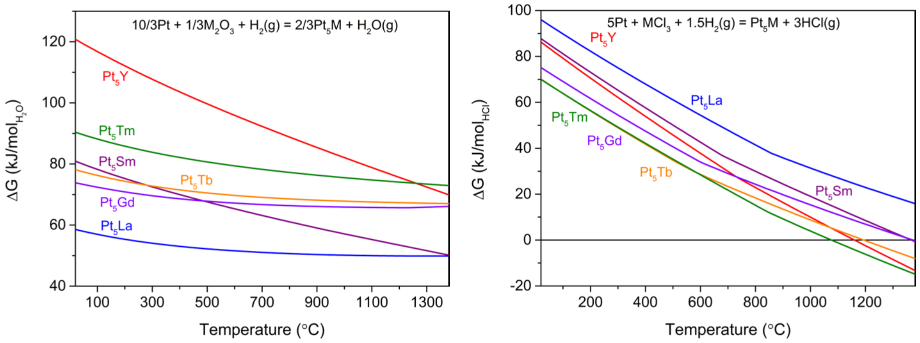

(a) Change in Gibbs free energy for Pt_5M alloys

(b) Change in Gibbs free energy for Pt_5M alloys

Figure 4.20: Change in Gibbs free energy for Pt_5M alloys from their respective **(a)** oxides or **(b)** chlorides as function of temperature. All reactions are normalised per mol of product gas

4.4.3 Alloying from Chlorides

In the previous section it was shown that the formation of a crystalline alloy can proceed through the thermal reduction of YCl_3 with Pt black in the presence of H_2. This was accomplished at 900 °C, however, this temperature is in the high end for nanoparticle preparation. In this section the analysis applied to the oxide system will be applied to the chloride salts of the RE metals.

Using HCS Chemistry and the expanded database, the change in Gibbs free energy was calculated for the following reaction.

$$5Pt + MCl_3 + \frac{3}{2}H_2(g) \rightleftharpoons Pt_5M + 3HCl(g) \tag{4.26}$$

In figure 4.20b the results for an interesting subset of lanthanide metals and yttrium can be seen. The change in Gibbs free energy is lower than for their corresponding oxide reactions (figure 4.20a) with overall tighter grouping as well. This indicates that all of them have very similar tolerances towards the product gas. Above 1000 °C the change even becomes negative shifting it to be a spontaneous reaction at equilibrium conditions. The other trend seen is the opposite internal relation for product gas tolerance. For the oxides the earlier lanthanide metals are the ones with the highest tolerance for H_2O, whereas for the chlorides these are the least tolerant for HCl_3. Continuing with the analysis the equilibrium partial pressure for the reaction can be approximated as

$$K = \frac{(P_{\mathrm{HCl}})^3}{(P_{\mathrm{H}_2})^{\frac{3}{2}}} \Rightarrow P_{\mathrm{HCl}} = \sqrt[3]{K} \tag{4.27}$$

Here it is implicit that P_{HCl} and P_{H_2} are partial pressures and therefore are divided by the total pressure. furthermore the assumption $P_{\mathrm{H}_2} \approx 1$ is made resulting in an error of 10 % when P_{HCl_3} reaches 0.03 %. Applying this to the alloying of Pt and Tb, the equilibrium partial pressures for the reduction reactions can be seen in figure 4.21. Compared to the case of oxides the tolerances for product gas is much higher with ‰ to % concentrations for relevant reduction temperatures. Even with the increasing error of the approximation the chlorides are generally easier to reduce than the oxides. As for the oxides the red area is where the Pt_5Tb can be formed, blue; both the Pt_5Tb and Pt_3Tb can be formed and finally in the green area both alloys can be formed and Pt_5Tb can be converted into Pt_3Tb.

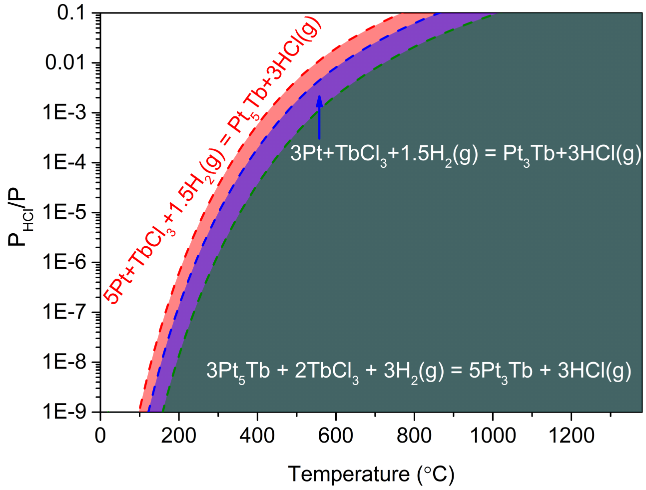

Figure 4.21: Equilibrium partial pressures for Pt_5Tb (red), Pt_3Tb (blue) and conversion from Pt_5Tb to Pt_3Tb (green) for reduction of the $TbCl_3$

All these calculations were done under the assumption that kinetics are not important for the reduction. There are, however, no indications that this is the case. If the process is kinetically limited instead of mass transport limited it will have large implications. Imagining that the reduction is limited by kinetics instead of mass transport, the highest achievable partial pressure will be lower than the equilibrium partial pressure. As a consequence the reduction time is increased and at the same time it open up for the formation of more than one phase of alloy from the onset.

4.5 Summary and Discussion

From the thermodynamics analysed in this section it is clear that the processes are sensitive to both oxygen and water. For low temperature synthesis, where chlorides or similar compounds are to be reduced the extremely low tolerances towards oxygen and water will prevent the formation of any alloy unless the reaction can proceed at rates higher than the influx of oxygen and water in the system. This rules out any synthesis carried out in water as those presented in chapter 2. The water will simply prevent any reduction of the rare earth metals. With this in mind the alkalide reduction method, while performed in a glovebox, would probably be one such method where even the low ppm presence of water in the solvent coupled with the trace oxygen in the glovebox would be enough to stop the alloying process as oxygen and water would be consumed before Pt could protect the reduced Gd or Y atoms. One could increase the concentration of precursor to combat this, however, solubility in the dry solvent could become a problem.

The cathodic corrosion with its heavy H_2 evolution and very negative operating potential forms a near-surface region where there is close to no O_2 or H_2O present allowing for the partial reduction Y. In the case investigated here, where the electrolyte was H_2O based this would most likely have caused the oxidation of the yttrium at the surface of the particles and with further Pt corrosion it could be trapped sub-surface and survive electrochemical measurement and this can also explain the XPS results. If a water free solvent and even more electropositive cations were used the process could potentially work

This leaves only the high temperature reduction by hydrogen as a viable method for alloy formation in it current form. Even in the oxygen and water containing instrumental H_2 the alloying was achieved within a reasonable time frame for the synthesis. Even working with permeable rubber tubing did not prevent the alloy formation. The following chapters will investigate the formation of electrocatalytically active alloy nanoparticles from this method.

Chapter 5

High Temperature Reduction in Quartz Reactor

From the last chapter it was concluded that of the methods investigated the only technique able to definitively produce the Pt_xY alloys is high temperature reduction by H_2. Coupled with the thermodynamic calculations of the reduction reaction, this chapter will further explore the high temperature reduction as a viable method for producing the Pt-RE alloys as active electrocatalysts for the ORR.

The work presented in this chapter was done in close collaboration with Christoffer Mølleskov Pedersen and will therefore present work that is also included in his PhD thesis [194].

5.1 Seed Nanoparticles

Similar as to the work in my Master thesis a commercial catalyst was used as seed crystals for the high temperature reduction. Contrary to the work in my Master thesis, the nanoparticles here were chosen from the insight gained from the model studies by Hernandez-Fernandez *et al.* and Velázquez-Palenzuela *et al.*[131,132] As presented in chapter 2 the optimal size for Pt nanoparticles is around 3 nm, however, as a Pt overlayer of ca. 1 nm is formed on the Pt-RE alloy nanoparticles, no activity enhancement is seen for this size. A Pt/C catalyst

with a larger particle size (6.6 nm specified by supplier) was therefore utilised as seed particles. Specifically a 50 wt % Pt/C catalyst (TEC10EA50E-HT) from Tanaka Kinkinzoku Kogyo K. K. (TKK). The particles were characterised both as received and after annealing to 900 °C following the same temperature profile as for the unsupported Pt black with YCp3.
The XRD analysis of the as received and annealed to 900 °C can be seen on figures 5.1a and 5.1b respectively. The as received catalyst show a crystallite size of 6.8 nm when Rietveld analysis is performed (green envelope). This size is in good agreement with that determined by the supplier. The annealed particles cannot be described by a single phase and two phases with different broadening were used to describe the pattern. One phase shows a close to unchanged crystallite size at 6.4 nm with the other phase showing a significant increase in crystallite size with 28 nm. This does not mean that the size distribution is bi-modal as not all information is captured by the two phases. All that can be concluded is that the size distribution has changed with larger sizes introduced from the annealing.

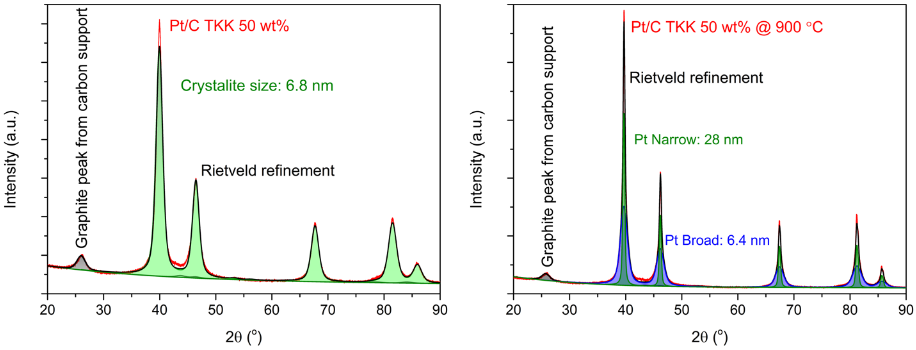

(a) XRD of as received TKK Pt/C

(b) Change in Gibbs free energy for Pt$_5$M alloys

Figure 5.1: (a) The as received TKK Pt/C showing a crystallite size of 6.8 nm from Rietveld analysis (green envelope) **(b)** The annealed TKK Pt/C showing narrower peaks, indicative of agglomeration. Two phases are needed to describe the overall pattern (green and blue envelopes). Both patterns show a broad feature of the graphitised support around 26 ° (grey envelope)

Further analysis was done be TEM imaging performed by Claudie Roy from CINF-DTU. The annealed catalyst was imaged to create the particle size distribution (PSD) seen in figure 5.2b. A representative image of the catalyst can be seen in figure 5.2a. Here the high metal loading impede the analysis as many particles overlap due to the projection. From the 129 particles counted the mean particle size was estimated at 7.7 nm ± 2.1 nm signifying a broad distribution. It is also seen how there is a clear tail towards larger particles.

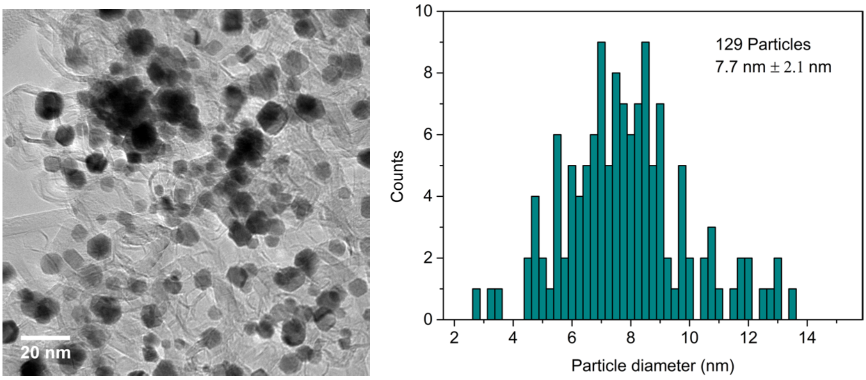

(a) TEM image of the annealed TKK Pt/C

(b) Particle size distribution from TEM imaging

Figure 5.2: **(a)** Representative TEM image of the TKK Pt/C catalyst after annealing showing crystalline particles with broad size distribution **(b)** Particle size distribution of the annealed TKK Pt/C showing clear tail to larger sizes with mean particle size of 7.7 nm ± 2.1 nm

The results from TEM analysis is in line with SAXS measurements performed at DTI.[194] Both as received and annealed TKK Pt/C was analysed showing a clear shift towards larger particle sizes and a broadening of the size distribution. The tail of the distribution reached $> 30\,\text{nm}$ for the annealed catalyst. The cumulative distribution showed that 50 % percent of the volume comes from particles in the desired range of 6 nm – 12 nm down from 75 % before annealing. The measurements also showed a surface per mass loss of 27 % from the annealing. To set up reference values for the synthesised catalysts the C 1s line and the Pt 4f line of the annealed catalyst was measured with XPS. The recorded spectra can be seen in figure 5.3, the value for the C 1s line was 284.7 eV and the Pt 4f line with an energy of 71.4 eV, slightly higher than the reported values for metallic Pt from NIST.[192]

Table 5.1: Electrochemical data for the TKK Pt/C 50 wt%

Catalyst	Specific Activity [mA cm^{-2}]	Mass Activity [$\text{A mg}_{\text{Pt}}{}^{-1}$]	ECSA [$\text{m}^2\,g^{-1}$]
As received	1.0 ± 0.2	0.27 ± 0.04	25 ± 1.5
Annealed 900 °C	1.32 ± 0.09	0.28 ± 0.02	21 ± 0.2

Electrochemical characterisation was carried out by Amado Andres Velázquez-Palenzuela and Christoffer Mølleskov Pedersen at CINF-DTU. The results from this can be seen in table 5.1. The loss of electrochemical surface area (ECSA) is less than measured by SAXS, here the surface area was only 16 % lower after

annealing. As expected with the increase in particle size and the ordering obtained by annealing, see figure 5.2a, the specific activity increased and with the decrease in ECSA, the mass activity was unaffected. This data will serve as the reference point for the synthesis.
Prior to the use of the TKK Pt/C, the catalyst was dried using the same procedure as for the Pt-black catalyst. Afte this it was stored in closed bottle in the aforementioned glovebox.

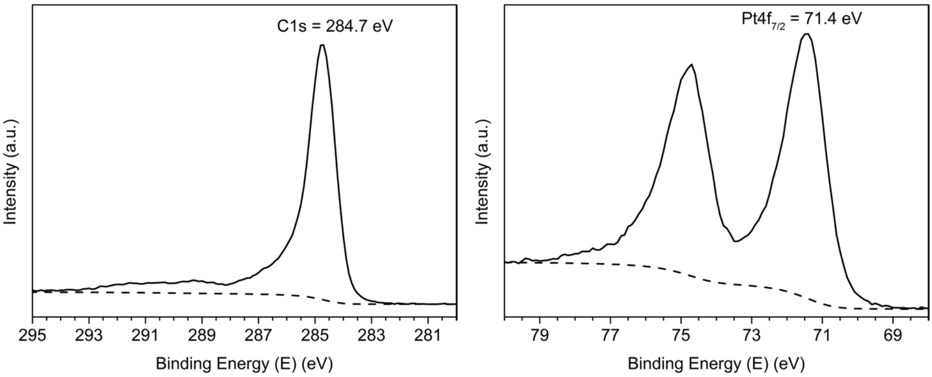

(a) XPS of C 1s for annealed TKK Pt/C

(b) XPS of Pt 4f for annealed TKK Pt/C

Figure 5.3: Reference values for **(a)** C 1s at 284.7 eV for the annealed TKK Pt/C catalyst and **(b)** Pt 4f at 71.4 eV for the annealed TKK Pt/C catalyst

5.2 Synthesis with YCp3

Following the promising results of the unsupported catalyst synthesis, the method was adapted to use the carbon supported TKK catalyst presented in the previous section. This section will go over the catalysts prepared both from the YCp3 and YCl3 precursors and characterise their composition, structure and activity as electrocatalysts. The two precursors will be treated separately and compared at the end.
This section will go over the catalysts prepared with the YCp3 precursor. In table 5.2 all prepared catalysts are listed with their reduction temperatures. Not all catalysts will be discussed in detail, however, the overall similarities will be highlighted and exemplified and outliers will also be explained.
To prove the concept of using the Pt/C as seed particles, an initial synthesis with the same annealing conditions and the same weight ratio between Pt and yttrium precursor (1:3) was performed. This is the catalyst denoted $\mathrm{Pt}_x\mathrm{Y/C}_{1Q}$ in table 5.2. After mortaring in the glovebox, until an uniform powder in both colour and granularity, the precursor mix was sealed in the reactor and transferred to the annealing setup. Here it was connected to the Schlenk line that

was purged with Ar and subsequently H_2. The reactor was then flushed with H_2 for 30 minutes before the heating was started and followed that for the unsupported.

Table 5.2: List of all catalysts prepared from YCp3 and TKK Pt/C in Quartz reactor

Sample	Precursor at. ratio [Pt:Y]	Pt/C weight [mg]	YCp3 weight [mg]	Reduction temperature [°C]
Pt_xY/C_{1Q}	0.48	322	484	900
Pt_xY/C_{2Q}	0.22	150	502	900
Pt_xY/C_{3Q}	0.21	150	515	800
Pt_xY/C_{4Q}	0.22	149	498	800
Pt_xY/C_{5Q}	0.22	128	429	700
Pt_xY/C_{6Q}	0.21	155	550	600
Pt_xY/C_{7Q}	0.20	151	550	550
Pt_xY/C_{8Q}	0.22	121	400	500

5.2.1 Characterisation

Part of the catalyst was washed in 1 M H_2SO_4 and both the unwashed and washed samples were characterised by XRD. Examining figure 5.4 that compares the two samples (blue and navy blue) with the annealed seed particles (red). It is seen how features of pure Pt are still present after the reduction, meaning that areas of the catalyst was not exposed to the precursor during reduction. Most features can be explained by the Pt_3Y and Pt_2Y phases, green and purple triangles respectively. Many of the features associated with Pt_2Y overlap with those of the $AuBe_5$ structure of Pt_5Y making them difficult to separate. However, the decrease in intensity after acid washing of the peaks described by the purple triangles relative to the support reveal that this phase is unstable in acid making Pt_2Y the most likely candidate. The unwashed catalyst showed features best described by $Y_{18}Pt_{50.56}Si_{15.44}$[201] (black asterisk), these disappear after acid washing, however, it indicates that the precursor reacts with the quartz similar as to what was observed for the YCl_3.

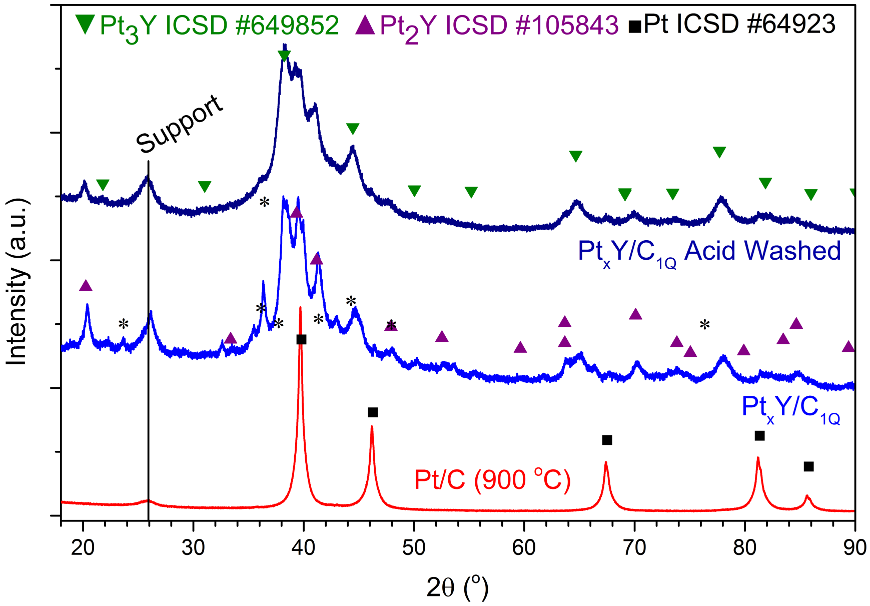

Figure 5.4: XRD pattern of as prepared and acid washed $\mathrm{Pt}_x\mathrm{Y/C}_{1Q}$. Present in both samples are $\mathrm{Pt_3Y}$ (green inverted triangles), $\mathrm{Pt_2Y}$ (purple triangles) and Pt (balck squares). In the as prepared sample an $\mathrm{Y_{18}Pt_{50.56}Si_{15.44}}$ (black asteriks) phase is also present, however, this disappears during acid washing.

Characterising the acid washed sample with XPS show that the Pt 4*f* line is at the same energy as the reference for the annealed TKK Pt/C (71.4 eV). The Y 3*d* line show a very broad profile where four phases were used to describe it. As for the the unsupported Pt black a phase with a binding energy of $\mathrm{Pt_3Y}$ is seen at 155.4 eV together with a $\mathrm{Pt}_x\mathrm{Y}$ phase at 156.4 eV. The two oxidised phases area ascribed to an oxide at 157.2 eV and the major component of the profile is comprised of the carbide phase. Even after acid washing in 1 M this phase persists, additional aggressive washing does remove the last of the oxide, however, some carbide remains even after four acid treatments.[194]

STEM HAADF imaging was use to gain more insight into the local structure of the catalyst. Figure 5.6a shows an overview image revealing large spread in sizes and shapes of the nanoparticles, a large difference from the annealed TKK Pt/C. The large cloud like features stem from particles in different planes than the focal plane of the microscope. Close examination reveal porous particles for which a close up is seen in 5.6b. Here the porous structure is clear and resembles that observed by Wang *et al.* for chemically leached $\mathrm{Cu_3Pt}$ nanoparticles.[202] With the presence of the unstable $\mathrm{Pt_2Y}$ and $\mathrm{Y_{18}Pt_{50.56}Si_{15.44}}$ excessive leaching could be expected. Another possible explanation for the low intensity areas on the particles could be local areas with high Y content. The lower mass of Y compared to Pt would yield significantly lower mass constrast in STEM and could also explain the low intensity regions. These yttrium rich phases would normally dissolve during acid washing, but with the carbide present it could protect these regions and prevent the leaching.

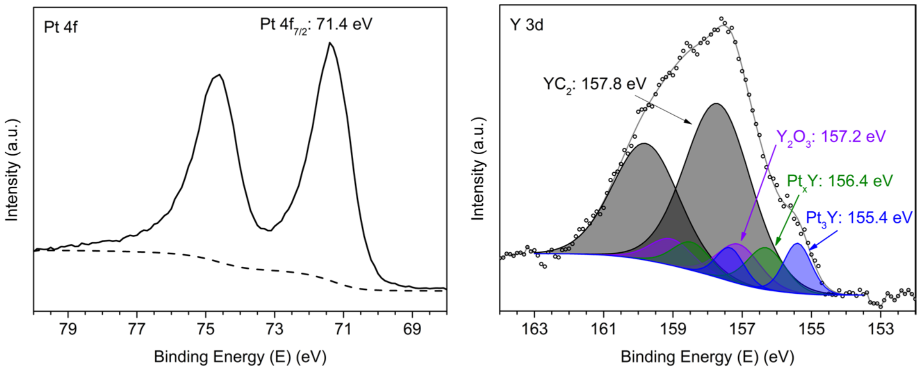

(a) XPS of the Pt $4f$ line for $\mathrm{Pt}_x\mathrm{YC}_{1Q}$

(b) XPS of the Y $3d$ line for $\mathrm{Pt}_x\mathrm{Y/C}_{1Q}$

Figure 5.5: (a) Pt $4f$ line for $\mathrm{Pt}_x\mathrm{Y/C}_{1Q}$ with a binding energy of 71.4 eV the same as for the annealed TKK Pt/C **(b)** Y $3d$ for $\mathrm{Pt}_x\mathrm{Y/C}_{1Q}$ showing two metallic phases at 155.4 eV and 156.4 eV for $\mathrm{Pt}_3\mathrm{Y}$ and $\mathrm{Pt}_x\mathrm{Y}$ respectively. Two oxidised phases are also observed at 157.2 eV and 157.8 eV for the oxide and carbide respectively.

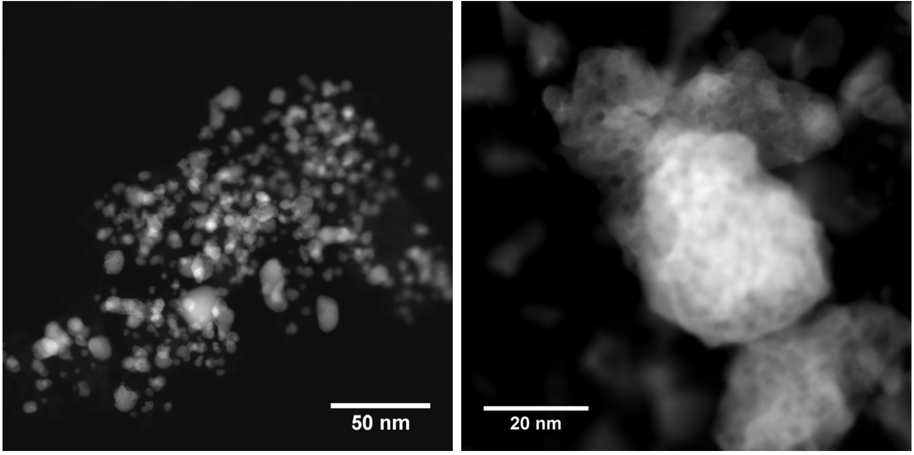

(a) STEM overview image of the $\mathrm{Pt}_x\mathrm{Y/C}_{1Q}$

(b) STEM close up image of the $\mathrm{Pt}_x\mathrm{Y/C}_{1Q}$

Figure 5.6: STEM images of the $\mathrm{Pt}_x\mathrm{Y/C}_{1Q}$ **(a)** Overview image showing the broad size distribution and high loading **(b)** Close up image showing an agglomerated particle with porous structure

The initial attempt with using the TKK Pt/C showed the same as the unsupported catalyst synthesis: Alloying is possible with high temperature reduction of YCp3, but carbide is produced and sits at the surface even after acid washing. It also introduces other alloy phases than the pure Pt_3Y seen for the unsupported catalyst. At the same time Pt particles are still present after the reduction indicating poor precursor mixing.

5.3 Temperature Series for YCp3

To further explore the system a temperature series was performed to explore the onset of alloying and effect on the alloy phases. It was the hope that lowering the reduction temperature would also lessen or stop the formation of carbide on the surface of the catalyst. The lowest temperature of 500 °C was chosen from the studies of Y and Gd modified Pt(111) crystals. As described in chapter 2 the mobility of Y and Gd in Pt had an onset at roughly this temperature.[128,129]
The catalysts were then synthesised in steps of 100 °C with an added synthesis at 550 °C.
The initial synthesis showed not all Pt was converted in during the reduction, as this could stem from inadequate mixing of precursors, the YCp3 amount was doubled. The rest of the procedure followed that of Pt_xY/C_{1Q}.

5.3.1 Characterisation

Figure 5.7 shows the XRD patterns of the acid washed catalysts from the temperature series with YCp3. The graphitised carbon support was seen in all samples and is denoted by S. For Pt_xY/C_{2Q} at 900 °C there were very few discernible features. Prior to acid wash this sample showed a large number of narrow peaks assigned to $Y_{18}Pt_{50.56}Si_{15.44}$,[194] however, these are gone after acid wash and have most probably left behind a porous disordered structure. The catalyst does show a single feature for the $Y_{18}Pt_{50.56}Si_{15.44}$ (asteriks) and a single peak at roughly 38 ° for the Pt_3Y phase (green inverted triangles). An explanation for the difference between this catalyst and the initial Pt_xY/C_{1Q} could be the increased amount of precursor. This could lead to the a larger amount of the $Y_{18}Pt_{50.56}Si_{15.44}$ phase. With this ultimately resulting in far greater leaching upon washing. This $Y_{18}Pt_{50.56}Si_{15.44}$ phase was also visible in Pt_xY/C_{4Q} at 800 °C along with both Pt_3Y and Pt_2Y (purple triangles). The two Pt-Y alloy phases are also present in Pt_xY/C_{5Q} at 700 °C, however, for Pt_xY/C_{6Q} at 600 °C only the Pt_3Y phase is discernible with fairly broad features. In all but the Pt_xY/C_{2Q} at 900 °C Pt peaks are observed at roughly 47 ° and 67 ° indicating that not all Pt was alloyed. The catalyst at 550 °C was added to check if alloying started between the Pt_xY/C_{8Q} and Pt_xY/C_{6Q} catalyst. While not shown here, alloying occurred at this temperature with Pt_3Y

features appearing with very low intensity.[194]

Overall the higher reduction temperatures favour the more yttrium rich alloy, Pt_2Y. This is as expected from the thermodynamics, however, the trend is not unequivocally discernible as the relative intensities between the Pt_3Y and Pt_2Y phases does not follow the expected change with increased annealing temperature. As such other factors may influence this such as mixing of the precursors or the quality of the precursor. While all precursors were checked visually for O_2 and H_2O exposure before use and all vials were from the same batch, it can not be ruled out that storage in the glovebox or slight variances between individual vials could be the cause of this variance.

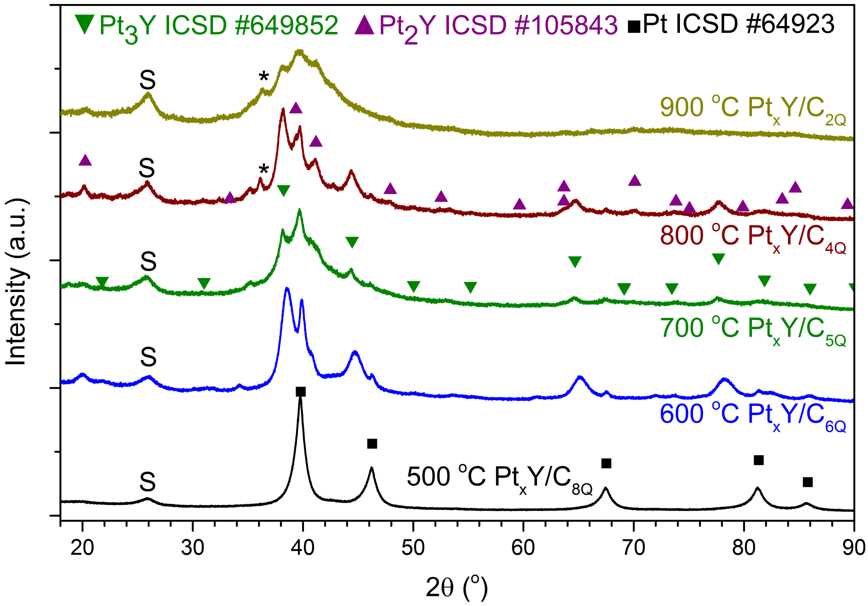

Figure 5.7: XRD patterns of acid washed YCp3 catalyst temperature series. Observed were Pt_3Y (green inverted triangles), Pt_2Y (purple triangles) and Pt (balck squares). For Pt_xY/C_{2Q} and Pt_xY/C_{4Q} an $Y_{18}Pt_{50.56}Si_{15.44}$ (black asteriks) phase was also present even after acid washing.

The temperature series was analysed by XPS after acid washing to identify the composition of the different catalysts, figure 5.8a shows the Y 3*d* spectrum for the catalyst reduced at 700 °C (Pt_xY/C_{5Q}). As for the catalysts reduced at higher temperatures the carbide dominates the surface composition. However there is a metallic component as expected from the XRD pattern in figure 5.7. Figure 5.8 summarises the elemental composition from XPS excluding the oxygen and carbon content. From the analysis it is seen that all catalysts contain varying amounts of carbide with the tendency for lower carbide content at lower reduction temperatures. The broad overlapping features of the XRD patterns precluded any meaningful Rietveld analysis as too many phases would be needed without a proper idea of the constraints on these.

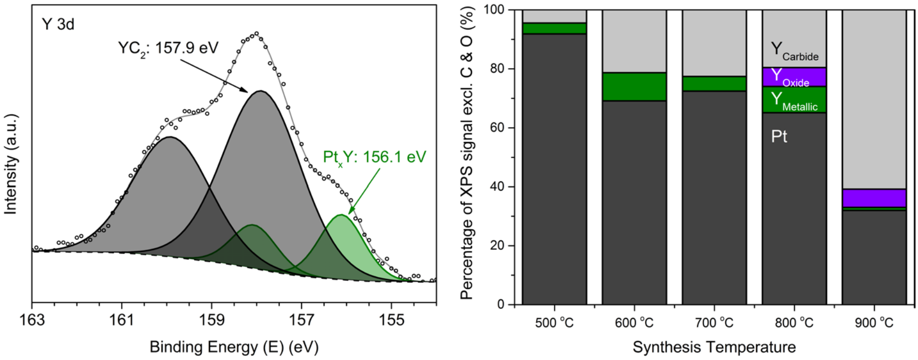

(a) XPS of the Y $3d$ line for Pt$_x$Y/C$_{5Q}$

(b) XPS composition for the YCp3 temperature series

Figure 5.8: (a) Y $3d$ line for Pt$_x$Y/C$_{5Q}$ with a binding energy of 156.4 eV for the metallic component (green) and 157.9 eV for the carbide (grey) **(b)** Elemental composition from XPS for the YCp3 excluding oxygen and carbon.

5.3.2 Electrochemistry

To test the activity of the synthesised nanoparticles towards the ORR, the catalyst reduced at 700 °C was subjected to electrochemical testing by Christoffer Mølleskov Pedersen.[194] This catalyst was chosen for its balance of the alloy phases showing the highest intensity for the Pt$_3$Y compared to Pt$_2$Y while still keeping the Pt features low. Figure 5.9 shows a summary of the electrochemical characterisation, with CVs on the left and the measured activity on the right. Comparing the CVs in N$_2$ saturated electrolyte for Pt$_x$Y/C$_{5Q}$ (red) and the TKK Pt/C (black dashed), it is seen how both the H and OH regions are suppressed as both catalysts are normalised to geometric surface area of the electrode. As the loading was higher on the for Pt$_x$Y/C$_{5Q}$ (21 µg cm^{-2} vs. 15 µg cm^{-2}) the only explanation being a lower ECSA as confirmed by CO stripping showing only 7.5 ± 0.35 m^2 g^{-1} significantly lower than for the seed particles, see table 5.1.[194] The right side graph shows the measured specific activity and it did not change significantly from the annealed TKK Pt/C. Coupled with the low ECSA the mass activity is decreased significantly, as seen on the far right graph in figure figure 5.9.

While both XRD and XPS confirmed that alloying took place during the high temperature reduction of the YCp3 precursor, the electrochemical measurements revealed no improvement in specific activity and a substantial decrease in ECSA. The presence of carbides on the catalyst was also seen from the XPS measurements. As these could not be removed by acid washing the surface of the alloy where the precursor decomposed is blocked by the carbide species and can not act as a catalyst for the ORR. This leaves only the pure Pt particles where no precursor was present during reduction. The YCp3 is therefore not suited as precursor for the formation of active Pt-Y electrocatalysts.

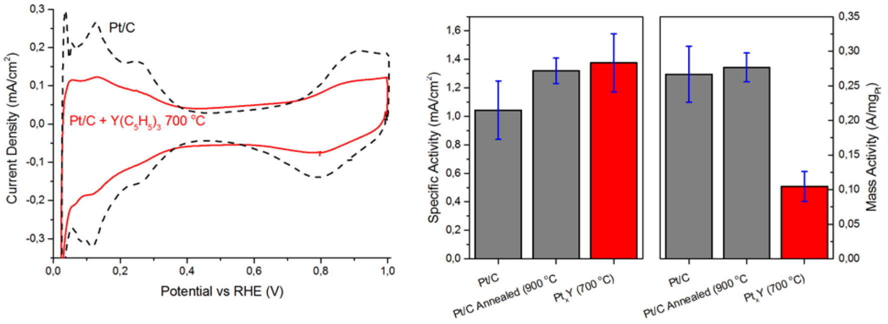

Figure 5.9: Electrochemical measurements for Pt_xY/C_{5Q} (red) and TKK Pt/C (black dashed). On the left are CV's in N_2 saturated electrolyte normalised to geometric area. To the right are the specific activity and mass activity normalised to active surface area after correcting for ohmic drop, mass transport and capacitance. The area was determined by CO stripping. Adapted from Christoffer Mølleskov Pedersen [194]

5.4 Synthesis with YCl_3

The YCl_3 synthesis was also repeated with TKK Pt/C. This section will go over the catalysts prepared by this precursor.
Table 5.3 lists the different catalysts prepared. The initial synthesis adapted the method from the unsupported catalyst by retaining the weight ratio between Pt and YCl_3 of one to three. With a melting point of 721 °C the precursor becomes liquid during the annealing process aiding in distributing it over the high surface area support. This should increase interaction with the Pt nanoparticles and diminish the inhomogeneities that are unavoidable from dry mixing. The procedure was kept the same as for the YCp3 catalysts on carbon support.

5.4.1 Characterisation

The initial YCl_3 reduction at 900 °C (Pt_xY/C_{9Q}) using the TKK Pt/C as seed particles was similar to the YCp3 split into two samples. One that was acid washed in 1 M H_2SO_4 and one that was as prepared. Both were characterised using XRD and the obtained patterns are compared to that of the annealed TKK Pt/C in figure 5.10.

Table 5.3: List of all catalysts prepared from YCl_3 and TKK Pt/C in Quartz reactor

Sample	Precursor at. ratio	Pt/C weight	YCl_3 weight	Reduction temperature
	[Pt:Y]	[mg]	[mg]	[°C]
Pt_xY/C_{9Q}	0.33	400	606	900
Pt_xY/C_{10Q}	0.14	195	682	900
Pt_xY/C_{11Q}	0.1	205	1001	800
Pt_xY/C_{12Q}	0.1	201	1000	700
Pt_xY/C_{13Q}	0.12	232	1001	750

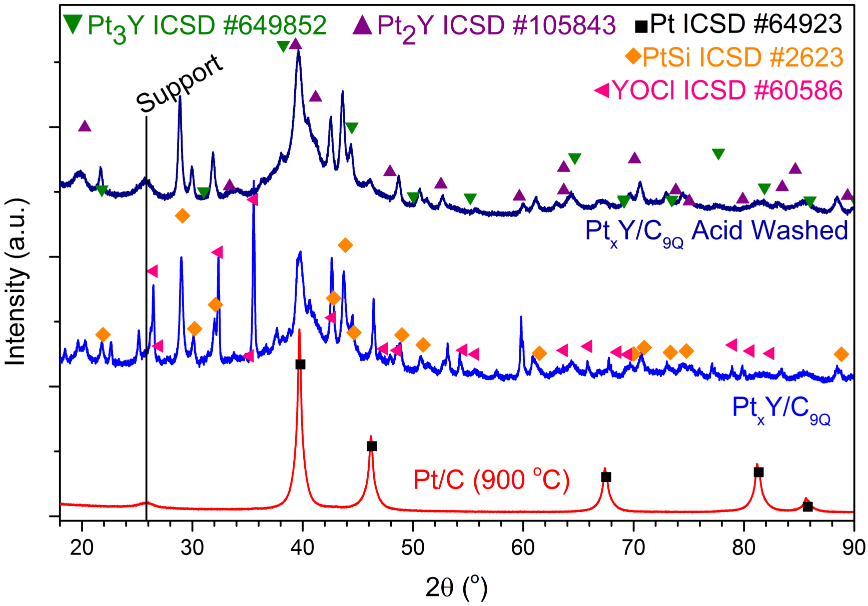

Figure 5.10: XRD pattern of as prepared and acid washed Pt_xY/C_{9Q}. Present in both samples are small amounts of Pt_3Y (green inverted triangles), Pt_2Y (purple triangles) and Pt (black squares). Also observed in the unwashed sample was a PtSi phase (orange diamonds) and YOCl (pink left pointing triangles).

Similar to the unsupported catalyst, the unwashed Pt_xY/C_{9Q} showed sharp peaks not associated with any of the alloy phases or pure Pt. They were best described by a PtSi phase (orange diamonds) and a YOCl phase (pink left pointing triangles). The YOCl phase is completely removed by the acid washing while the PtSi phase remains even after washing. This is further evidence that the YCl_3 facilitates the reduction of the quartz reactor at the elevated reduction temperature. For the unsupported catalyst the main component was Pt_3Y with a small contribution from PtSi alloys. For the carbon supported catalyst, the opposite is seen. Here the Pt_3Y phase is barely discernible, with PtSi dominating along with pure Pt. The only other phase present in the catalyst was Pt_2Y. Even though the precursor becomes liquid at the reduction temperature, the dramatic increase in surface area and the reactor design seems to mitigate the interaction between the precursor and the YCl_3. As a consequence, the interaction with the reactor walls increases and the PtSi would seem to become the more favourable product.

The same observations were done when analysing the acid washed sample with XPS. Overall the spectra for the Pt $4f$ and Y $3d$ lines resemble those of the unsupported catalyst with two Si phases present in the sample and three Y phases. The Pt also show the same two phases as for the unsupported catalyst, with the high binding energy phase most likely originating from the PtSi alloy. As concluded from the XRD the reaction with Si is favoured over the reaction with Y as both the Si phases are more prominent compared to Y here than for the unsupported catalyst in figure 4.16b. At the same time, the Pt_3Y phase at 155.4 eV is significantly reduced.

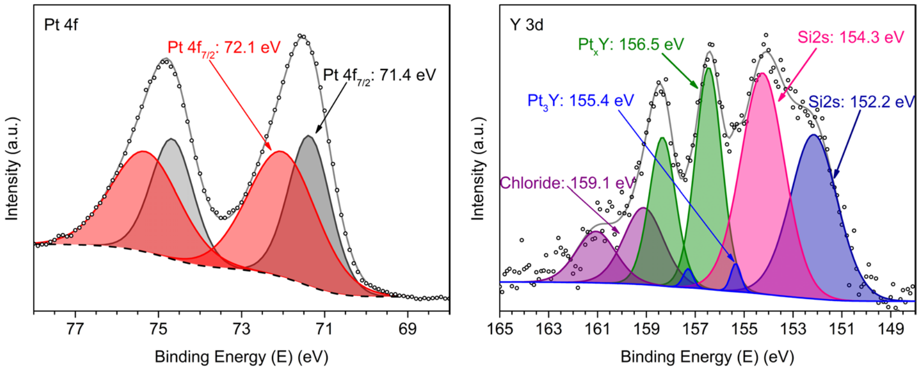

(a) XPS of the Pt $4f$ line for Pt_xY/C_{9Q}

(b) XPS of the Y $3d$ line for Pt_xY/C_{9Q}

Figure 5.11: **(a)** Pt $4f$ line for Pt_xY/C_{9Q} with a binding energy of 71.4 eV the same as for the annealed TKK Pt/C **(b)** Y $3d$ for Pt_xY/C_{9Q} showing two metallic phases at 155.4 eV and 156.4 eV for Pt_3Y and Pt_xY respectively. Two oxidised phases are also observed at 157.2 eV and 157.8 eV for the oxide and carbide respectively.

5.5 Temperature Series for YCl_3

A temperature series was also performed for the YCl_3 precursor to explore the system and reduce the formation of PtSi phases. To increase the interaction further between YCl_3 and the TKK Pt/C the weight ratio was changed from 1:3 to 1:10 for Pt:YCl_3. The rest of the parameters remained unaltered with the reduction temperature changing in steps of 100 °C.

5.5.1 Characterisation

Figure 5.12 compares the XRD pattern for Pt_xY/C_{11Q}, Pt_xY/C_{12Q} and Pt_xY/C_{13Q} reduced at 800 °C, 700 °C and 750 °C respectively. From the profile of the catalyst reduced at 700 °C no significant alloying takes place. The series was therefore stopped at 700 °C and an additional step at 750 °C was added to check if alloying commenced here, similar to the case for YCp3.

Prior to acid wash the patterns were dominated by chloride and oxychlorides. All catalysts also showed minor component of PtSi that disappeared upon acid washing except for the catalyst reduced at 900 °C. Here the PtSi phase was the main constituent of the pattern and it is therefore not included. This further indicates the significance of YCl_3 as the intermediate for the quartz reduction allowing for the formation of PtSi. For the catalyst reduced at 800 °C the main peaks are associated with Pt_3Y and pure Pt. The patterns also reveal that there were no significant changes between the 700 °C and 750 °C catalysts and both mainly showed Pt peaks. However small features not associated with either PtSi, Pt_3Y or Pt_2Y are visible and become more prominent for the 800 °C catalyst. As the features show up at lower temperatures than Pt_3Y the most plausible alloy phase would be Pt_5Y, as the thermodynamic calculations showed that this would be the most favoured reaction. The $AuBe_5$ structure has been included (orange right pointing triangles), however, this does not describe the additional features either.

The catalysts were also characterised by XPS after acid washing, with the Y 3*d* line for Pt_xY/C_{11Q} shown in figure 5.13a. Similar to the Pt_xY/C_{9Q} there is a small component from the Pt_3Y alloy with a large contribution from the Pt_xY alloys. Compiling the elemental composition from XPS (excluding O and C) for the different catalysts gives figure 5.13b. As is seen there is a stark difference between the catalyst reduced at 900 °C and that reduced at 800 °C. For the highest temperature reduction Si contributes more than 70 % of the surface composition when excluding O and C, and does not have any presence at 800 °C. For this catalyst the Pt:Y ratio was 14.5 the same as the ratio seen for the mass selected nanoparticles after electrochemistry.[131] The leaching process is however, different and it is uncertain if the results are comparable. The 700 °C and 750 °C catalysts show very little metallic yttrium compared to the catalyst at 800 °C. These compositions agree with what was measured by SEM-EDS at DTI, however, here the catalyst reduced at 800 °C also contained Si something that was not observed in the XPS and XRD measurements.[194]

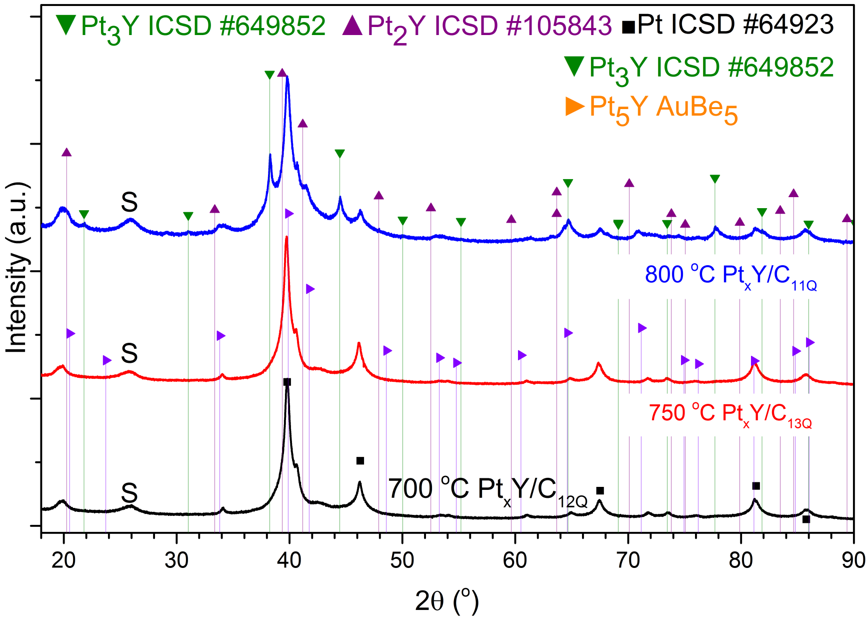

Figure 5.12: XRD patterns of acid washed YCl_3 temperature series. Observed were Pt_3Y (green inverted triangles), with possibly phases being Pt_2Y (purple triangles) and Pt_5Y ($AuBe_5$) (orange right pointing triangles). for all catalysts Pt was observed (balck squares).

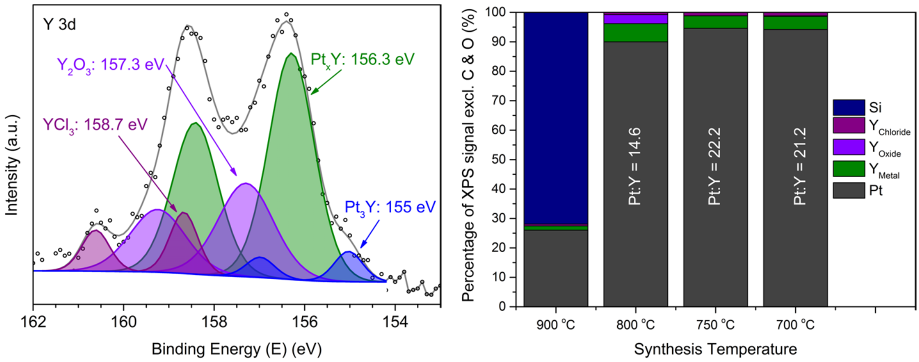

(a) XPS of the Y 3*d* line for Pt_xY/C_{11Q}

(b) XPS composition for the YCp3 temperature series

Figure 5.13: **(a)** Y 3*d* line for Pt_xY/C_{11Q} with a binding energy of 155 eV for the Pt_3Y component, 156.3 eV for the metallic component (green) and 157.3 eV for the oxide (violet) and 158.7 eV for the chloride (purple) **(b)** Elemental composition from XPS for the YCl_3 excluding oxygen and carbon.

The majority of nanoparticles observed with STEM had structures that differed from the bulk structure of Pt. In figure 5.14 two particles showing alternating bright and dark rows of atoms are shown. For the particle in figure 5.14a the alternation in intensity stops before the edge of the particle here all rows show the same intensity. As the particles have been acid washed prior to the STEM analysis this core shell structure is in agreement with the catalyst treatment. Figure 5.14b shows another example of the alternating intensity with the dark rows seemingly missing an atom compared to the bright rows. The fact that the atom structure is still visible after acid washing indicates that these particles are closer to the stable phase than those formed from YCp3. The particles do however show some areas of lower intensity with a concurrent loss of the atomic structure, see figure 5.14.

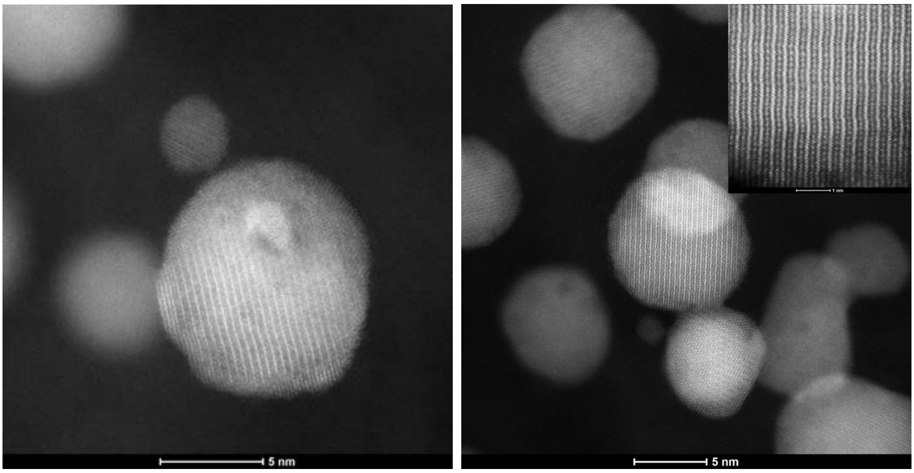

(a) STEM overview image of the Pt_xY/C_{11Q}

(b) STEM close up image of the Pt_xY/C_{11Q}

Figure 5.14: STEM images of the Pt_xY/C_{11Q} **(a)** Overview image showing the broad size distribution and high loading **(b)** Close up image showing an agglomerated particle with porous structure

During the STEM analysis particles exhibiting hexagonal structures with what appears to be cavities at the center were found.[194] One such particle is imaged in figure 5.15 showing the hexagonal structure in the core and thin shell of close packed atoms at the surface. By filtering the central spot of the fast Fourier transform (FFT) away, the hexagonal structure is even more evident as seen from the inverse fast Fourier transform (IFFT) on the right. This also highlights the close packed surface layer of the particle. Though it appears as if the centres of the hexagonal lattice is empty this not the case instead a lighter element takes up the space giving an overall lower intensity for these column. Even though this hexagonal lattice fits with the overall structure of the $CaCu_5$ structure of

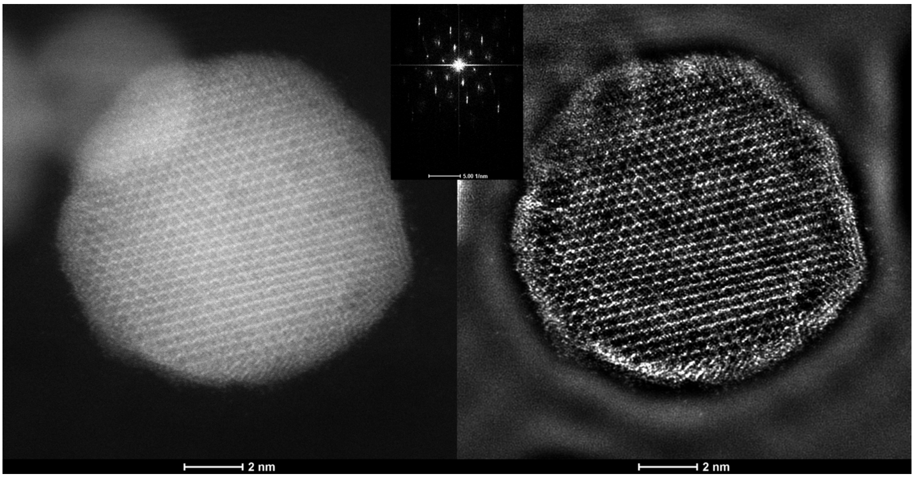

Figure 5.15: (left) STEM image of particle from Pt_xY/C_{11Q}. The particle exhibits a clear hexagonal strucure that is highlighted further by the IFFT image (right) of the FFT (insert) with the central spot filtered away.

Pt_5Y when projected along the [001], the distances between the supposed dark columns of Y does not match up to the inter atomic distances in the bulk crystal structure. Nor does it fit any of the other structures mentioned in chapter 2. Even considering Pt-Si alloys that might have formed when taking the SEM-EDS results from DTI into account no match was found. An explanation for this could be the complex nature of the Pt-Y family of structures that was mentioned in chapter 2. It is possible that a different structure exists that would match the hexagonal structure of this system when subjected to the right $2d$ projection of the structure.

5.5.2 Electrochemistry

The catalyst reduced at 800 °C showed the most optimal results from both XRD, XPS and SEM-EDS. As for the YCp3 precursor the electrochemical characterisation was carried out by Christoffer Mølleskov Pedersen and the results are summarised in figure 5.16. On the left are the CVs in N_2 for both the TKK Pt/C (black), the YCp3 catalyst (red) and the YCl_3 catalyst (green). The YCl_3 catalyst had a slightly lower loading than the other two electrodes with $13.5\ \mu g\ cm^{-2}$ even so the features from H and OH are close to those of the unmodified Pt/C catalyst. This resulted in an ECSA of $19 \pm 4\ m^2\ g^{-1}$, close to that of the annealed Pt/C, see table 5.1. The specific activity on the graph to the right shows a slight increase over both the annealed Pt/C and the catalyst from the YCp3 precursor. The large standard deviation can be an indication of an inhomogeneous catalyst or the local presence of SiO_2 blocking the surface of the nanoparticles. This spread is carried over to the mass activity that sees a significant increase over the YCp3 catalyst as the surface is no longer blocked by carbide species. However, there is no significant increase compared to the annealed Pt/C.

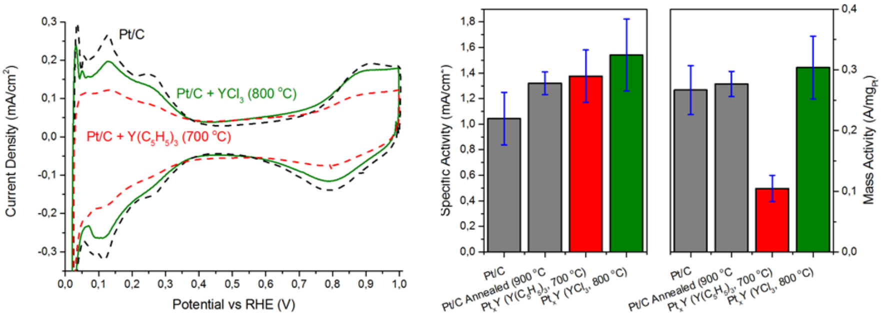

Figure 5.16: Electrochemical measurements for Pt$_x$Y/C$_{11Q}$ (green), Pt$_x$Y/C$_{5Q}$ (red) and TKK Pt/C (black dashed). On the left are CV's in N$_2$ saturated electrolyte normalised to geometric area. To the right are the specific activity and mass activity normalised to active surface area after correcting for ohmic drop, mass transport and capacitance. The area was determined by CO stripping. Adapted from Christoffer Mølleskov Pedersen [194]

5.6 Summary

The step from unsupported Pt black to TKK Pt/C as seed particles presented the synthesis with new challenges. Both the precursors proved capable of forming the alloy on carbon supported Pt seed particles. However, the pure phase system of the unsupported catalyst was no longer present. Instead the catalyst started showing the presence of both Pt$_2$Y and Pt$_5$Y alongside the Pt$_3$Y. The large surface area from the carbon support also meant that the precursor amount needed to be increased significantly and even so a pure Pt phase was observed for most of the catalyst prepared. For the YCp3 precursor it was seen how it was reduced and formed an observable alloy phase already at 550 °C in good agreement with the temperature for Y mobility in Pt, reported by Ulrikkeholm *et al.*[129] However, the precursor also produced an acid resistant carbide that covered the surface. No reduction temperature was without a carbide and as such, the mass activity for the ORR dropped below that of the seed catalyst. STEM analysis also showed what could be interpreted as porous nanoparticles further suggestion a too high concentration of Y in the nanoparticles. Overall it proved to be the lesser candidate of the two precursors.

The YCl$_3$ did not see a significant increase activity either and instead of a carbide the precursor facilitated the reduction of the quartz reactor and the formation of a PtSi alloy. However with a reactor made from a different material than quartz, the possibility of a PtSi alloy can be prevented. This would also allow for better control over the reduction atmosphere as the wholes system could be sealed properly instead of being based on glass-rubber, glass-glass and glass-teflon seals. Such a setup will be introduced in the following chapter and used to further optimise the alloy synthesis.

Chapter 6

High Temperature Reduction in Metal Reactor

From the work done in the quartz reactor it is clear that it is possible to reduce both YCp3 and YCl_3 to form the Pt-Y alloys. The setup using rubber tubing and glass seals proved to not prevent the formation as the synthesis has a manageable tolerance towards H_2O and the time it would take to fully oxidise the alloy by O_2 can be measured in days. However the quartz reactor itself was a problem as the interaction between the SiO_2 and yttrium precursors facilitated the formation of PtSi and $Y_{18}Pt_{50.56}Si_{15.44}$. Two unwanted products that mitigated the desired alloy formation. To prevent the formation of these phases, the setup for the high temperature reduction was redone in metal with VCR fittings and the gas purity was increased to scientific 6.0 to further control over the process. This chapter will present the setup and work done in the new metal reactor. The alloys produced was expanded to also include Pt-Gd and Pt-Tb alloys. From the conclusion of the work performed in the quartz reactor the reduction temperature of 800 °C was kept for all synthesised catalysts in the metal reactors.

In the work presented herein there is one caveat: The Theta Probe XPS was down, due to technical issues during the whole period the studies on this setup were conducted. As such, any observations done with XPS came after all catalysts had been prepared and otherwise characterised by XRD and electrochemistry. The information learned from XPS could therefore not be used to alter and further optimise the process during the thesis work.

6.1 Setups

Two different custom reactors was used for the synthesis. The second of which was taken into use, as the furnace used had to be replaced due to a breakdown. A schematic of the setup, including the two reactors, can be seen in figure 6.1 with the main reactor outlined in red and the reactor used after the furnace exchange outlined in green. The gas was changed from instrumental grade to scientific grade for both Ar and H_2 (N6.0 AGA) with the flow controlled by mass flow controllers. The flow of Ar used to flush the system prior to and following reduction was 10 mL min^{-1} with the hydrogen flow being 100 mL min^{-1} during reduction. The system was closed of from the reactor and the surrounding when not in use by manual valves. On the other side of the furnace/reactor part the exhaust was let through a 3 m coil of 1/8 inch metal tubing to avoid back diffusion of O_2 and H_2O from the air. Both ends of this coil was terminated in a manual valve to keep it closed between experiments. All other tubing was made of 1/4 inch metal tubing and all connections between valves were VCR connectors with Cu gaskets.

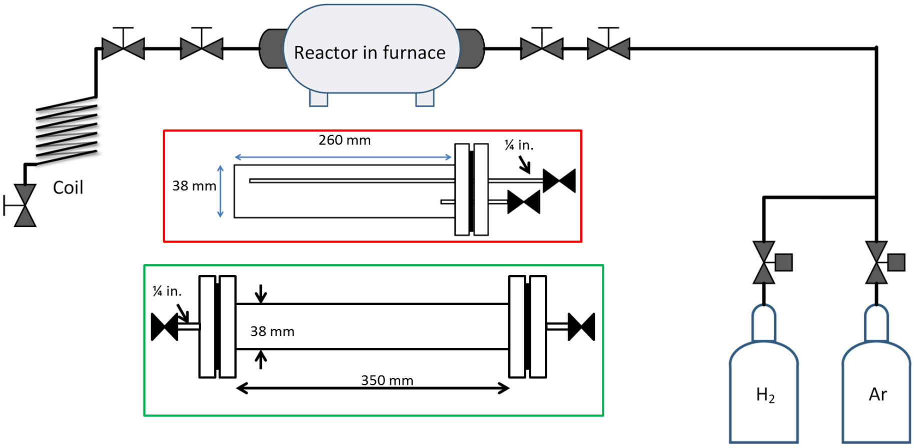

Figure 6.1: Diagram of Setup for Metal reactors with primary reactor (red outline) and reactor used after furnace exchange (green outline)

The reactor themselves were made from 316 stainless steel with 2-3/4 inch CF flanges as end plates with Cu gaskets. Welded into these end plates were the two 1/4 inch tubes with VCR fittings for connection to the gas system. For the main reactor the inlet and outlet were situated at the same end due to the use of a tube furnace. This meant that the inlet tube was extended inside the reactor so that the gas was forced over the precursor mix. As the second furnace was a split tube furnace this allowed the outlet to be placed at the opposite end to the inlet. The reactors were lined with a graphite foil (99.8 %, Alfa Aesar, 0.254 mm) to prevent interactions between the precursors and the metal walls. The change from an upright cross reactor to flat bed like reactor with the precursor mix spread in a thin layer should also enhance the distribution of H_2 through the powder layer, facilitating faster removal of product gas. Overall this should remove any localised mass transport problems that the quartz cross reactor suffered from due to the packing of the precursor mix. The result should be a more homogeneous reduction and final catalyst.

6.2 Methods

This section will go over the procedure for synthesising the catalysts in the metal reactors. Several different parameters were used in an effort to optimise the phase purity of the system.

6.2.1 Dry Mixing

The dry mixing of precursors was repeated in the new metal reactors and expanded to include both $GdCl_3$ and $TbCl_3$ precursors, the two most promising lanthanide metals as reported by Escudero-Escribano *et al.*[119] With the introduction of other RE metals the weight ratio was changed to an atomic ratio of Pt:RE 1:10. After weighing the needed precursors inside the glovebox, they were mortared until uniform in colour and texture. The mix was then spread evenly over the central 5 cm of the reactor. Once the reactor was closed of it was transferred to the setup and purged first with Ar at 10 mL min^{-1} for 20 min before switching to H_2 and further purging for 20 min at 100 mL min^{-1}. Following this the annealing process was started by increasing the temperature 40 °C min^{-1} for 10 min, then 10 °C min^{-1} for 20 min and finally 30 min was then used to reach the 800 °C. The temperature was then kept for 360 min before it was left to cool of naturally. Once at room temperature the gas was switched to Ar and the reactor purged before returning it to the glovebox. The reactor was then opened and the catalyst removed from the reactor and subsequently removed from the glovebox and left to passivate in air. Following this step the catalysts were treated following the same procedure for acid washing as the previous catalysts.

6.2.2 Solvent Mixing

For the subsequent catalysts, the phase selectivity was sought to be improved by limiting the excess amount of chloride precursor. In order to do this, the dispersion of the precursor needed to be optimised to ensure proper alloy formation. To this end anhydrous acetonitrile (99.8 %, Sigma-Aldrich, < 10 ppm H_2O) was used to dissolve the chlorides and mix with the TKK Pt/C. The mixing was done in open glass vial stirred using glass covered magnetic stirrers at 250 rpm. First the precursor was dissolved in the acetonitrile, then the TKK Pt/C catalyst was added and the mix was kept on the stirrer plate until all solvent had evaporated. This process was left for 72 hours to complete. From this step the synthesis procedure followed that of the dry mixing catalysts.

6.3 Dry Mixed Catalysts

The first catalysts prepared in the metal reactors were the dry mixed Pt_xY/C, Pt_xGd/C and Pt_xTb/C. The three catalysts prepared are listed in table 6.1 with their atomic mixing ratios.

Table 6.1: List of dry mixed catalysts prepared from MCl_3 (M = Y, Gd, Tb) and TKK Pt/C in metal reactor

Sample	Precursor at. ratio [Pt:M]	Pt/C weight [mg]	MCl_3 weight [mg]
Pt_xY/C_{15}	0.1	200	1000
Pt_xGd/C_1	0.1	208	1270
Pt_xTb/C_1	0.1	224	1399

Pt_xY/C_{15}

The YCl_3 catalyst prepared by dry mixing was analysed by XRD and XPS to confirm the alloy formation. The pattern after acid wash can be seen in figure 6.2 with all the reference lines normalised to their most intense peaks. Examining the pattern it becomes clear that the change to the metal reactor has both improved the reaction and introduced new obstacles. The peaks for pure Pt have all disappeared indicating full conversion of the Pt particles. However, the alloy formed is not a single phase, instead both Pt_2Y (purple lines) and Pt_3Y (green lines) was observed. The $AuBe_5$ structure of the Pt_5Y can not be directly confirmed by XRD as the many phases with peaks close to each other makes for a broad profile as seen from the insert in figure 6.2. In contrast to the work in the quartz reactor the Pt_3Y phase is the dominant phase from XRD with Pt_2Y being the second most. The complex structure of the pattern and the many possible alloys and phases of these made Reitveld analysis impractical as no physical meaning could be extracted. The XRD pattern also reveal the possible presence of an Pt_3Fe like phase (pink lines). This is most noticeable with the peak at 46.9 °. Such a phase could originate from the HCl_3 gas produced during the synthesis reacting with the gas tube inside the reactor (see the red insert in figure 6.1). From the insert in 6.2 it is seen that, except for the Pt_3Y, the pattern is not described by the presence of either of the presented structures. The simplest explanation for the difference is that the observed peaks are the superposition of the listed phases and as such the resulting peak positions are altered from the pure phase systems. Other possible explanations are stacking faults in the structure of the alloys or completely different structures not yet described. The profile is, however, so broad and with too few distinct peaks to allow for proper analysis of these possibilities.

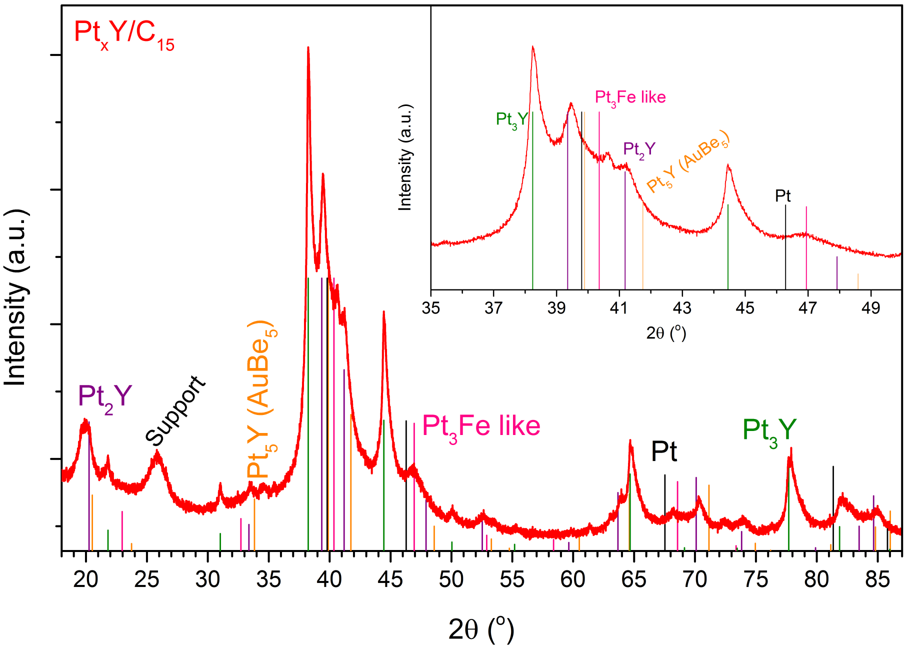

Figure 6.2: XRD pattern of as prepared and acid washed Pt_xY/C_{15}. Reference lines plottet Pt_3Y (green lines), Pt_2Y (purple lines) Pt_3Fe (pink lines) and Pt (balck lines). The insert shows the broad nature of the central region of the pattern

The XPS analysis in figure 6.3 confirms that the alloying has taken place with the appearance of a Pt_3Y phase at 155.3eV and a Y phase at 156.5eV this energy does not fall within the values normally measured for the metallic phase and could potentially be an oxide. The width of the peak, however, resembles that of the metallic phases. The washing procedure would seem to not be thorough enough as a YCl_3 component was also observed at 158.4 eV. The presence of chlorine was confirmed from the slight signal for the Cl 2*p* seen in the insert in figure 6.3. With the indications of a Pt_3Fe phase from XRD the Fe 2*p* line was also examined with XPS without any signal detected.

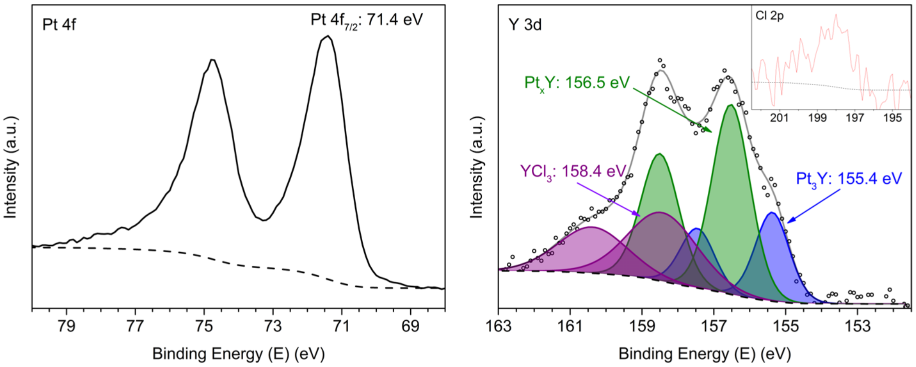

(a) XPS of the Pt $4f$ line for Pt_xY/C_{15} **(b)** XPS of the Y $3d$ line for Pt_xY/C_{15}

Figure 6.3: **(a)** Pt $4f$ line for Pt_xY/C_{15} with a binding energy of 71.4 eV the same as for the annealed TKK Pt/C **(b)** Y $3d$ for Pt_xY/C_{15} showing one metallic phases at 155.3 eV for Pt_3Y and a phase 156.5 eV that could be Pt_xY or an oxidised species. An chloride phase was also observed at 158.4 eV and confirmed by Cl $2p$ signal in the insert.

Pt_xGd/C_1

The result of expanding the synthesis to include the formation of the Pt-Gd can be seen in the obtained XRD pattern in figure 6.4 for Pt_xGd/C_1. As for the YCl_3 reduction there is a possible Pt_3Fe phase with the peak at 46.9 ° being the clearest indication. The peaks for Pt are also gone indicating complete alloying, however, none of the phases believed to be stable in acid correspond to the remaining peaks. Both the Pt_2Gd (purple) and the Pt_5Gd in $CaCu_5$ structure (green) and the structure reported by Ulrikkeholm *et al.*[129] (orange lines) have peaks close to the observed peaks. The $CaCu_5$, however, does have one very unmatched peak at 44.6 ° making it less likely to be present at any significant concentration. The peak at 41 ° is the only one that coincide with a peak from both the two Pt_5Gd structures and the Pt_2Gd structure. As before one explanation for these unmatched peaks is that they are the result of a superposition of phases or the existence of other unknown phases.

The position and shape of the Gd $4d$ line from XPS is compared to that of the reference Pt_5Gd crystal reported by Escudero-Escribano *et al.* in figure 6.5.[118] The slight upwards shift in the position of the Gd $4d$ line is also seen in the Pt $4f$ line that is detected at 71.6 eV. The overall shape does, however fit with the profile of the metallic Gd from the bulk of the crystal further confirming the alloying.

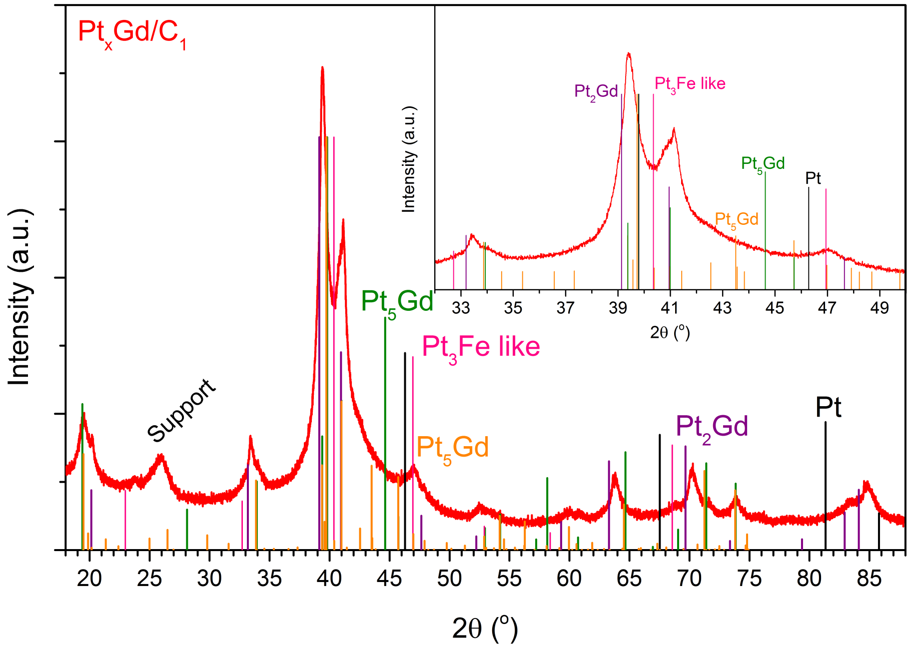

Figure 6.4: XRD pattern of acid washed Pt$_x$Gd/C$_1$. Reference lines included Pt$_5$Gd (green lines, CaCu$_5$), Pt$_5$Gd (orange lines, Ulrikkeholm[129]), Pt$_2$Gd (purple lines) and Pt (balck lines).

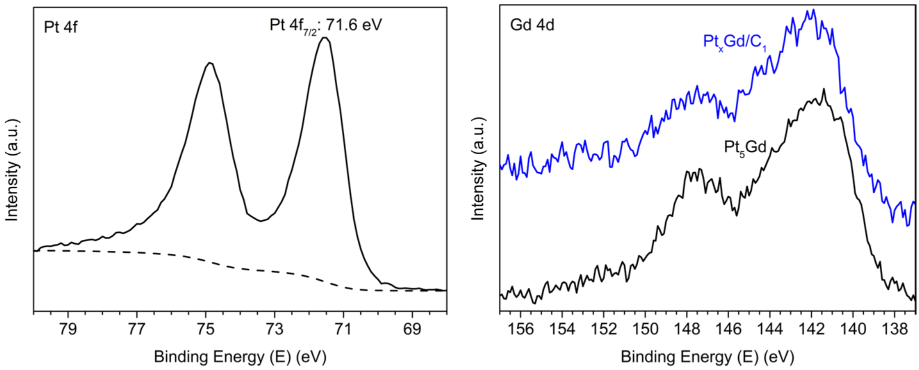

(a) XPS of the Pt 4*f* line for Pt$_x$Gd/C$_1$

(b) XPS of the Gd 4*d* line for Pt$_x$Gd/C$_1$

Figure 6.5: **(a)** Pt 4*f* line for Pt$_x$Gd/C$_1$ with a binding energy of 71.6 eV the same as for the annealed TKK Pt/C **(b)** Gd 4*d* for Pt$_x$Gd/C$_1$ compared to a reference spectrum for Gd 4*d* for polycrystalline Pt$_5$Gd

While not a statistically significant observation, TEM investigation gave some

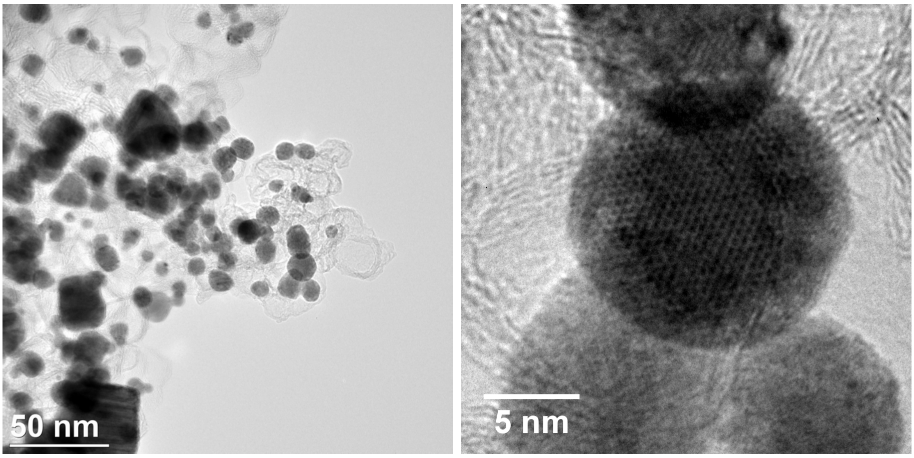

(a) TEM overview image of the Pt_xGd/C_1

(b) TEM close up image of the Pt_xGd/C_1

Figure 6.6: TEM images of the Pt_xGd/C_1 **(a)** Overview image showing the broad size distribution**(b)** Close up image showing a core-shell particle with a crystalline hexagonal core and a shell without apparent structure . The shell thickness is ~ 1 nm. TEM images acquired by Claudie Roy (CINF-DTU).

insight into the crystal structure of the nanoparticles. figure 6.6a shows an overview TEM image of the acid washed Pt_xGd/C_1 catalyst. Most of the particles here are close to, if not above the desired size for the nanoparticles. Examining one of the outlying particles on the right side of the image in figure 6.6a reveal a clear core-shell structure, with a shell thickness around 1 nm. The particle can be seen in figure 6.6b. The core structure is hexagonal and performing a FFT on the particle results in the pattern seen in the insert of figure 6.7a. Applying a mask that selects the eight diffraction spots and performing an IFFT gives the structure seen in figure 6.7a. The hexagonal structure in the core of the particle exhibit distances between centers that is far too large for a pure Pt structure. This is the same type of structure as seen for the YCl_3 synthesised particles examined in chapter 5. Measuring the distance between the low intensity areas of the structure along the red and green vectors reveal 9.213 Å and 5.333 Å respectively. These distances are in good agreement with the Gd-Gd distances in the Pt_5Gd structure in figure 6.7b for the [001] projection of the structure. Here the distances for the red and green vectors are 9.145 Å and 5.280 Å respectively. The Pt_5Gd Structure could not be confirmed by XRD, however, the discovery of this particle indicates that the alloy structure is indeed formed during the reduction. Even though the particles have been exposed to a chemical acid leaching process, the structure of the core survived. This is different from what was observed for for Cu rich Pt-Cu nanoparticles by Wang *et al.*[202] This could be due to the large excess of Cu present in the particles compared to the

Pt rich Pt_5Gd particle, or the ordered structure of the alloy coupled with the strong heat of formation stabilises the particle even though the thermodynamic driving force for dissolution is considerable.

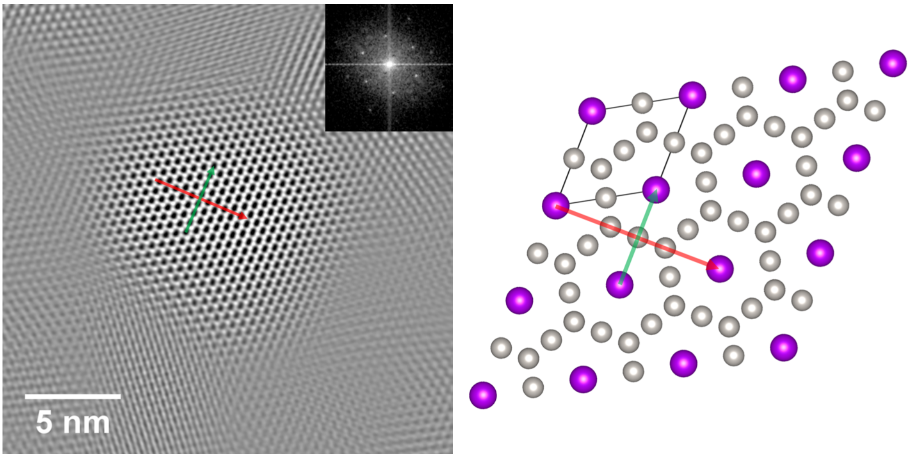

(a) IFFT of crystalline Pt_5Gd nanoparticle with insert of the FFT used for generating the structure

(b) Pt_5Gd $CaCu_5$ structure

Figure 6.7: **(a)** IFFT of the FFT from the crystalline particle from the Pt_xGd/C_1 catalyst **(b)** reference structure of Pt_5Gd in the $CaCu_5$ phase

Pt_xTb/C_1

Continuing the expansion of the alloys formed by the high temperature reduction, the Pt-Tb alloys were synthesised. A comment should be made on the precursor used. While it was of the same grade as both the Y and Gd chlorides (99.99 %, Sigma-Aldrich, anhydrous), the weight was 10 % higher than specified and instead of a loose powder like the other two precursors the $TbCl_3$ was larger crystallites. One possible explanation for this difference could be partial hydration of the precursor even though it was bought as being anhydrous.
The XRD pattern obtained for the Pt_xTb/C_1 catalyst is shown in figure 6.8. A stark difference to the Gd and Y alloys is seen, as the system only consists of two phases of Pt-Tb.

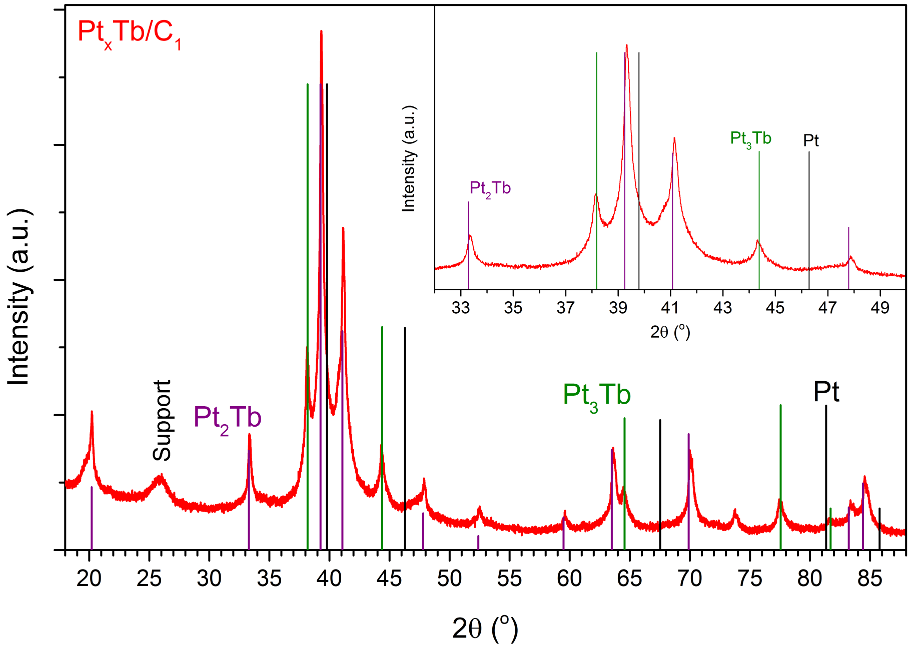

Figure 6.8: XRD pattern of acid washed Pt$_x$Tb/C$_1$. Reference lines included Pt$_5$Gd (green lines, CaCu$_5$), Pt$_5$Gd (orange lines, Ulrikkeholm[129]), Pt$_2$Gd (purple lines) and Pt (balck lines).

One is the Pt$_3$Tb (green) while the other is the Pt$_2$Tb phase (purple). The most abundant phase is again the Pt$_2$Tb, this hampers the promise for the catalyst as the phase is highly unstable under ORR conditions. Again here the Pt peaks are gone indicating complete alloying. Examining Tb 4*d* lines from XPS it is clear from the shape of the feature that the system resembles that of the bulk polycrystalline disc reported by Escudero-Escribano *et al.*[119] Similar to the Pt$_x$Gd/C$_1$ the Pt 4*f* line is shifted upwards compared with the reference value from the seed TKK Pt/C and the values from NIST. For both the Pt$_x$Gd/C$_1$ and Pt$_x$Tb/C$_1$ a fixed offset was measured during XPS. The spectra was therefore shifted so that the C 1*s* line overlapped with that of the TKK Pt/C at 284.7 eV. It could be that the true position should be lower.

The shift to a metallic reactor improved the alloying conditions, as the peaks associated with the Pt structure were gone from the XRD patterns. For YCl$_3$, the Pt$_3$Y alloy became the most abundant phase followed by the Pt$_2$Y alloy. This could pose a problem for the electrocatalyst as the latter phase is highly unstable under ORR operating conditions.[117] The same point can be made for the synthesised catalysts with both Gd and Tb, with Tb showing the simplest phase distribution. The multiple phases observed in the XRD patterns does not

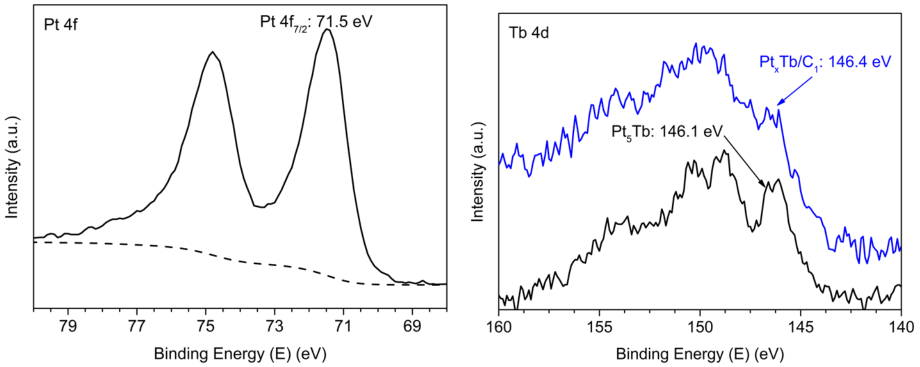

(a) XPS of the Pt $4f$ line for $\mathrm{Pt}_x\mathrm{Tb/C}_1$

(b) XPS of the Gd $4d$ line for $\mathrm{Pt}_x\mathrm{Tb/C}_1$

Figure 6.9: **(a)** Pt $4f$ line for $\mathrm{Pt}_x\mathrm{Tb/C}_1$ with a binding energy of 71.5 eV the same as for the annealed TKK Pt/C **(b)** Tb $4d$ for $\mathrm{Pt}_x\mathrm{Tb/C}_1$ compared to a reference spectrum for Tb $4d$ for polycrystalline $\mathrm{Pt}_5\mathrm{Tb}$

allow for the extraction of any meaningful information related to the structure, as such only local structure by TEM was possible. However, to get statistically relevant data, many more particles are needed for the analysis. All of which have to have ordered structures and be aligned along different crystal orientations.

6.4 Solvent Mixed Catalysts

Table 6.2: List of solvent mixed catalysts prepared from MCl_3 (M = Y, Gd, Tb) and TKK Pt/C in metal reactor. Catalysts **in bold** were prepared using the reactor in green outline in figure 6.1 For all catalysts 15 mL of acetonitrile was used

Sample	Precursor at. ratio [Pt:M]	Pt/C weight [mg]	MCl_3 weight [mg]	Reduction time [minutes]
$\mathrm{Pt}_x\mathrm{Y/C}_{SolMix3}$	1.5	202	80	360
$\mathrm{Pt}_x\mathrm{Y/C}_{SolMix4}$	1.5	202	74	100
$\mathrm{Pt}_x\mathrm{Y/C}_{SolMix5}$	1.5	202	78	360
$\mathbf{Pt}_x\mathbf{Gd/C}_{SolMix1}$	1.5	200	91	360
$\mathbf{Pt}_x\mathbf{Tb/C}_{SolMix1}$	1.5	200	100	360

In an effort to limit the possibility for the catalyst to form the Pt_2M phase, the initial amount of chloride precursor was reduced. In order to still be able to disperse the precursor over the surface area of the catalyst the chloride was dissolved and mixed with the TKK Pt/C catalyst using the dry solvent previously presented.
Table 6.2 lists the different catalysts prepared and presented in this chapter. It shows both the precursor amounts, the intended atomic precursor ratio and the reduction time at 800 °C.

Pt_xY/C

Three catalysts were prepared with a precursor atomic ratio of 1.5 for Pt:M. Due to a furnace failure for $Pt_xY/C_{SolMix4}$ the catalyst was only reduced for 100 min at 800 °C before the temperature started to drop of. In figure 6.10 the XRD patterns obtained for the three catalysts can be seen.

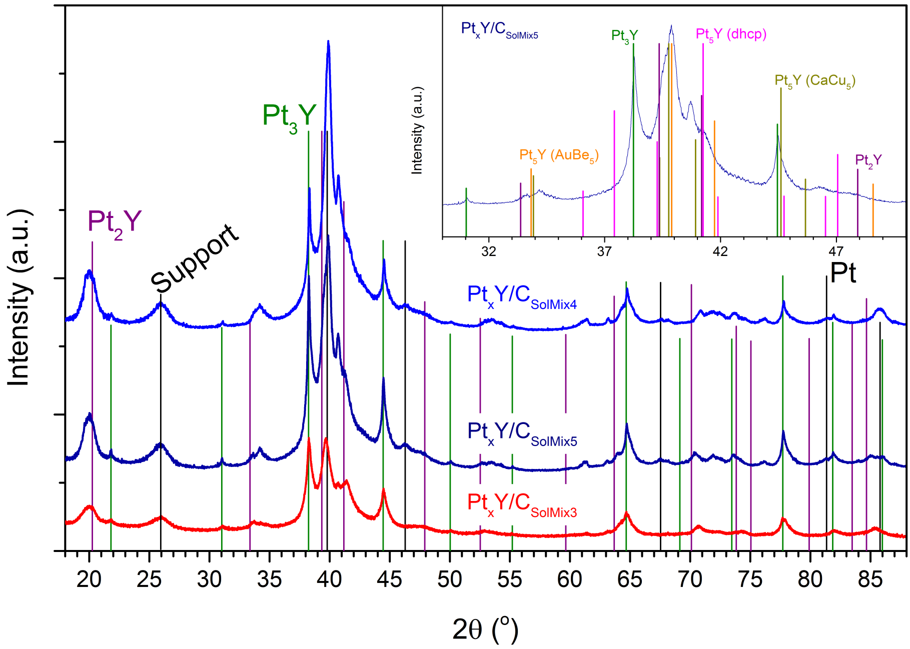

Figure 6.10: XRD pattern of acid washed $Pt_xY/C_{SolMix3}$ through $Pt_xY/C_{SolMix5}$. Reference lines Pt_3Y (green lines), Pt_2Y (purple lines) and Pt (balck lines).

From the patterns it is clear that the process of dispersing the precursor in acetonitrile succeeds in spreading the precursor over the whole surface area. For all catalysts it is seen how the peaks for Pt have disappeared and the alloys formed are also the same as for the dry mixed catalysts. The Pt_2Y phase along with the Pt_3Y phase were the best candidates for the alloys present. However the Pt_5Y structures cannot be neglected as many of the central peaks, seen in the insert, overlap with the reference peaks for the various structures. Two peaks in the insert (34.2 ° and 40.7 °) does not match the Pt_5Y structures and could belong to a different structure. Looking closer at the relative intensities for the Pt_xY peak at 40 ° and Pt_3Y peak at 38 °, it is clear that $Pt_xY/C_{SolMix3}$ has the highest contribution from Pt_3Y, followed by $Pt_xY/C_{SolMix5}$ and finally the catalyst that was only annealed for only 100 min follows, with the lowest Pt_3Y to Pt_xY ratio. The apparent lower amount of Pt_3Y in the catalyst annealed for the shortest time is in line with the thermodynamics described in chapter 4, as the Pt_5Y structure is more favoured it should be the first to form. If the system is kinetically limited the other alloy phases may also form, however, the Pt_5Y phase should be formed at the highest rate. The insert in figure 6.10 show the region of the XRD pattern where all the relevant phases of Pt_xY have their main components. Due to the overlap between all the different phases of Pt_xY mentioned in this thesis, attempts at deconvolution of the patterns were unsuccessful and further phase purity is needed before such attempts can succeed. The different structures of the alloy phases share many peak positions and are also closely related when it comes to stacking sequences as explained in chapter 2. This leads to difficulties when synthesising the many small crystallites that nanoparticles are, as each particle is formed individually and can therefore form any of structures if they are close enough in energy to each other.

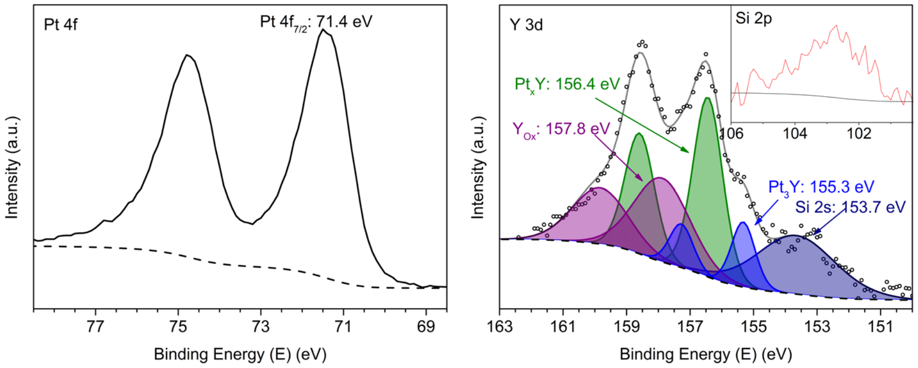

(a) XPS of the Pt $4f$ line for $Pt_xY/C_{SolMix3}$

(b) XPS of the Y $3d$ line for $Pt_xY/C_{SolMix3}$

Figure 6.11: XPS of $Pt_xY/C_{SolMix3}$ **(a)** Pt $4f$ line and **(b)** Y $3d$ showing two metallic phases; 155.3 eV and 156.4 eV for Pt_3Y and Pt_xY respectively. An oxide was observed at 157.8 eV. Si was also observed and confirmed by the Si $2p$ line.

Figure 6.11 show the XPS analysis for the $Pt_xY/C_{SolMix3}$ catalyst. The Y $3d$ line was described by two phases of metallic $Y3d_{5/2}$ at 155.3 eV and 156.4 eV for the the Pt_3Y and Pt_xY respectively. An oxide was observed at 157.8 eV further suggesting that the acid washing is incomplete for the work done in the metal reactor. Si 2*s* was also observed in overlap with the Y 3*d* line and confirmed by the presence of a Si 2*p* line (see insert in figure 6.11). As the following two catalysts did not contain any Si this is thought to be a local contamination and not a systematic problem with the process. Figure 6.12 summarises the elemental composition from XPS of the three catalysts, when excluding oxygen and carbon content. All three show very high content of metallic yttrium compared to the work done in the quartz reactor, underlining the importance of mass transport of the product gas and inertness of the reactor.

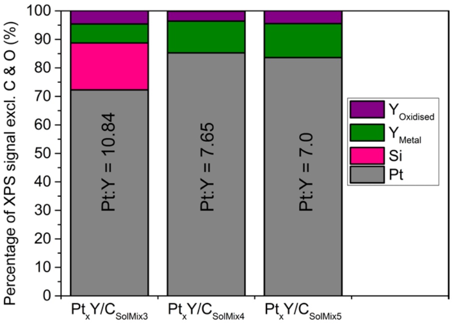

Figure 6.12: Elemental composition from XPS for the three solvent mixed YCl_3 catalysts

Pt_xM/C

For the catalysts with Tb and Gd the XRD patterns in figure 6.13 reveal that not all Pt was alloyed as there were still peaks associated with Pt. Both the Tb and Gd patterns are close to exact copies of each other, even down to the intensities of the individual peaks. This is different from the dry mixed catalysts, where the Tb catalyst was perfectly described by the Pt_3Tb phase together with the Pt_2Tb phase. For the solvent mixing both catalysts are better described by the proposed structure for Pt_5Gd published by Ulrikkeholm *et al.*[129] However this is not a perfect description and the unmatched intensities in the central region of the pattern (see the insert in figure 6.13) coincide with the unmatched for the YCl_3 catalyst. These shared peaks across the different system indicate a separate structure shared amongst the examined alloys of Pt and REs.
Turning to the XPS analysis in figures 6.14a and 6.15a, the Pt 4*f* lines are on top of the reference value for the TKK Pt/C at 71.3 eV and 71.4 eV for the $Pt_xGd/C_{SolMix1}$ and $Pt_xTb/C_{SolMix1}$ respectively. The respective 4*d* lines for Gd and Tb are normalised to the reference lines acquired by Paolo Malacrida at CINF-DTU. Comparing the lines for Gd 4*d* in figure 6.14b it is seen how the position and shape of the spectrum follow that of the reference sample.

From this it can be concluded that the Gd present in the catalyst is in the same chemical state as that present in the bulk crystalline alloy. This being the metallic state of Gd. The same analysis for Tb $4d$ in figure 6.15b show the same tendency, however, here there is a slight shift between the measured catalyst and the reference sample. This shift is on the order of 0.2 eV and not significant enough to classify the Tb as an oxide. As such the Tb present in the catalyst is also in the metallic state and both the XRD and XPS confirm that even with the low amount of precursor available alloying takes place, however, it is incomplete as Pt peaks are still present in the XRD patterns. For both catalysts a clear Si $2s$ line is observed, the reason for this is unknown as the only change was that of the reactor used for the synthesis.

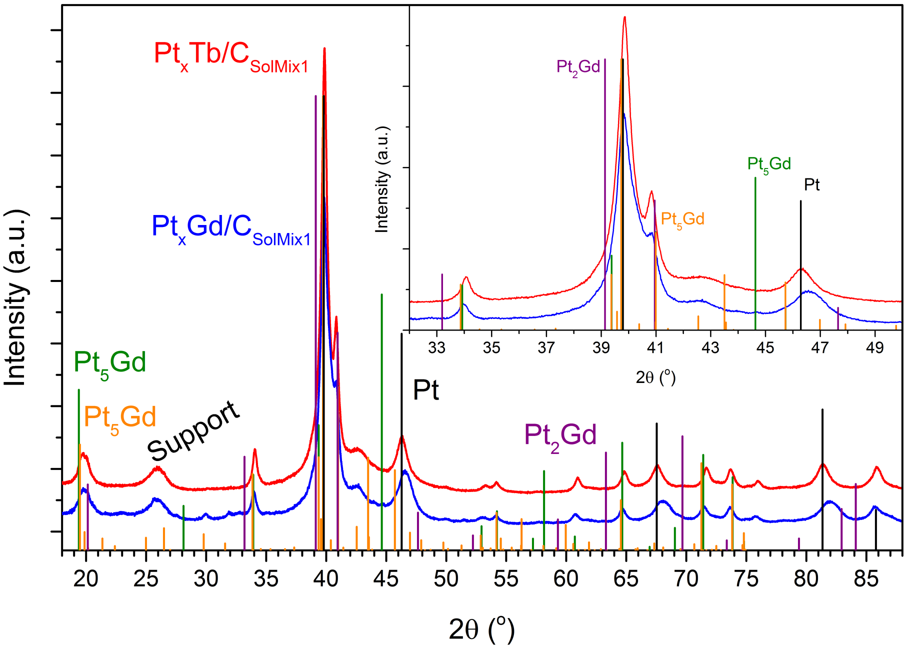

Figure 6.13: XRD pattern of acid washed Pt$_x$Gd/C$_{SolMix1}$ and Pt$_x$Tb/C$_{SolMix1}$. Reference lines included are Pt$_5$Gd (green lines, CaCu$_5$), Pt$_5$Gd (orange lines, Ulrikkeholm[129]), Pt$_2$Gd (purple lines) and Pt (balck lines).

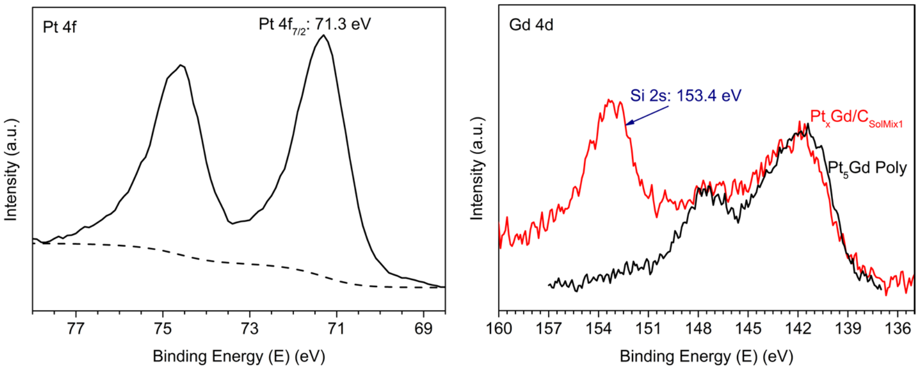

(a) XPS of the Pt $4f$ line for $Pt_xGd/C_{SolMix1}$

(b) XPS of the Gd $4d$ line for $Pt_xGd/C_{SolMix1}$

Figure 6.14: **(a)** Pt $4f$ line for $Pt_xGd/C_{SolMix1}$ with a binding energy of 71.3 eV the same as for the annealed TKK Pt/C **(b)** Gd $4d$ line compared to the reference spectrum of polycrystalline Pt_5Gd. The Si $2s$ line was located at 153.4 eV

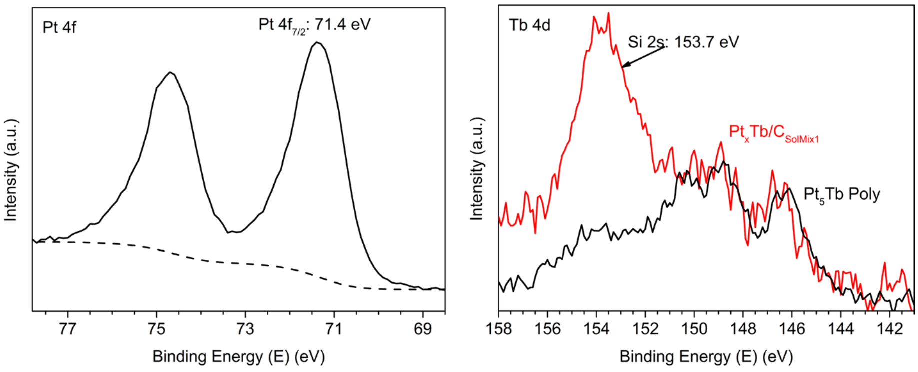

(a) XPS of the Pt $4f$ line for $Pt_xTb/C_{SolMix1}$

(b) XPS of the Tb $4d$ line for $Pt_xTb/C_{SolMix1}$

Figure 6.15: **(a)** Pt $4f$ line for $Pt_xTb/C_{SolMix1}$ with a binding energy of 71.4 eV the same as for the annealed TKK Pt/C **(b)** Tb $4d$ line compared to the reference spectrum of polycrystalline Pt_5Tb. The Si $2s$ line was located at 153.7 eV

6.4.1 Hexagonal Pt_3RE Structure

The seemingly shared structure of the Pt_xRE alloys observed for the $TbCl_3$ and $GdCl_3$ point towards a structure not yet considered for the alloys. The presence of Si is assumed to not affect the XRD patterns, as similar features were observed for the dry mixed catalysts and the solvent mixed YCl_3 catalysts. In an effort to find a structure that fitted with the observed pattern an unrestricted search for binary alloys was performed. $Pt_xTb/C_{SolMix1}$ was used as the reference pattern and it was assumed to only consist of pure Pt and then a single alloy phase. A good candidate came in the form of $GdIr_3$, a hexagonal alloy with space group R -3 m (166). Exchanging the Ir atoms for Pt, the Gd atoms for Tb and optimising the unit cell to the fitted peak positions in HighScore Plus gave the following lattice parameters a: 5.272 ± 0.008 Å, c: 26.405 ± 0.070 Å. The structure is illustrated in figure 6.16. The structure is closely related to the structure reported by Ulrikkeholm *et al.*[129] The powder diffraction pattern for this structure was simulated with the Cu K_α line used in the XRD setup. The resulting pattern is overlaid with the Pt reference and the $Pt_xTb/C_{\mathrm{SolMix1}}$ in figure 6.17. The structure does show a good overlap with the peaks observed in $Pt_xTb/C_{SolMix1}$, however, one peak is not reflected in the measured catalyst. To be conclusive a pure phase system is needed to confirm the validity of this structure. It is also not known if this structure is thermodynamically stable and as such this serves only as a preliminary guess of a possible structure. However the possible presence of yet another structure closely related to the other structures illustrates the problems in characterising the synthesised nano alloys.

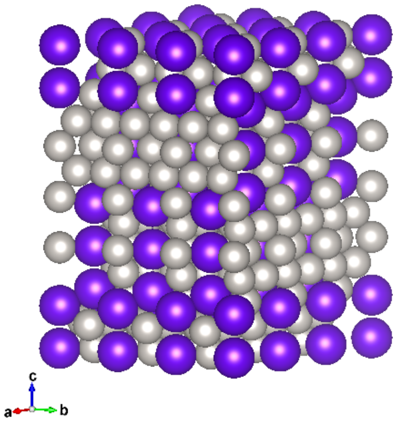

Figure 6.16: Structure of the possible hexagonal Pt_3Tb. The structure is closely related to that proposed by Ulrikkeholm *et al.* [129]

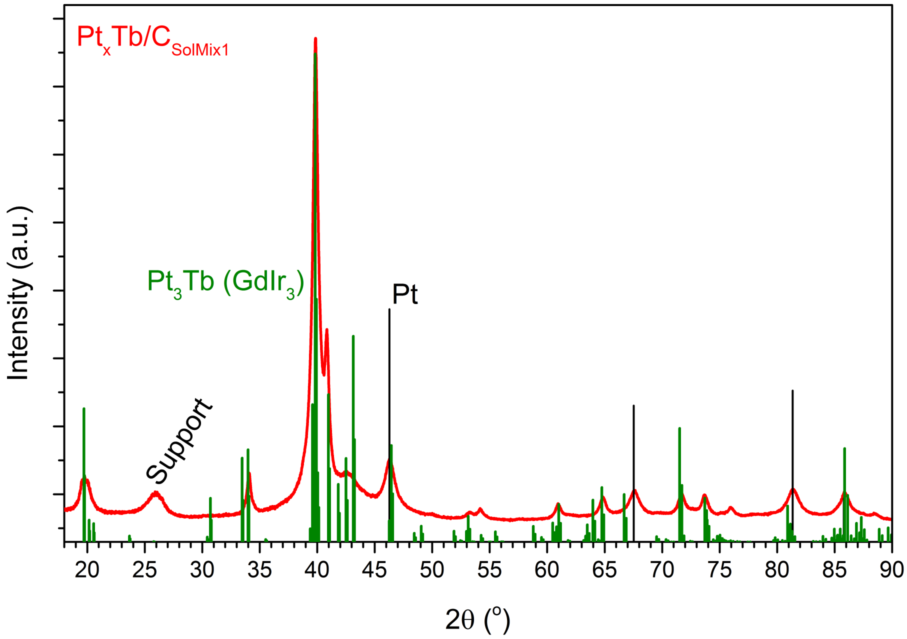

Figure 6.17: XRD pattern of acid washed Pt$_x$Tb/C$_{SolMix1}$. Reference lines included are the calculated hexagonal Pt$_3$Tb lines (green, GdIr$_3$) and Pt (balck lines).

6.4.2 Electrocatalytic Activity for ORR

With the change to a metal reactor it was possible to dramatically lower the amount of precursor needed and still achieve full conversion of the Pt/C catalyst. This was most prevalent in the Pt-Y alloy catalysts with three independent catalysts showing good alloying from both XRD and XPS. The catalyst that had the highest fraction of Pt$_3$Y was Pt$_x$Y/C$_{SolMix3}$ and to test how successful alloying was at creating a active electrocatalyst Amado Andres Velazquez-Palenzuela performed electrochemical measurements.

Figure 6.18 show both the CV in N$_2$ saturated electrolyte and the calculated ECSA from CO-stripping. The catalyst was cycled 162 times before a stable CV was achieved. This can be seen in the blue line in figure 6.18a where the stable cycle is plotted against the initial cycle (red). Here it is seen how the surface is cleaned over time as the features of H and OH start to appear. Overall the features of H adsorption are suppressed compared to the unaltered TKK Pt/C. The slight down shift of the CV seen in is caused by slight wetting of the sides of the glassy carbon and should not affect the catalytic properties or evaluation.

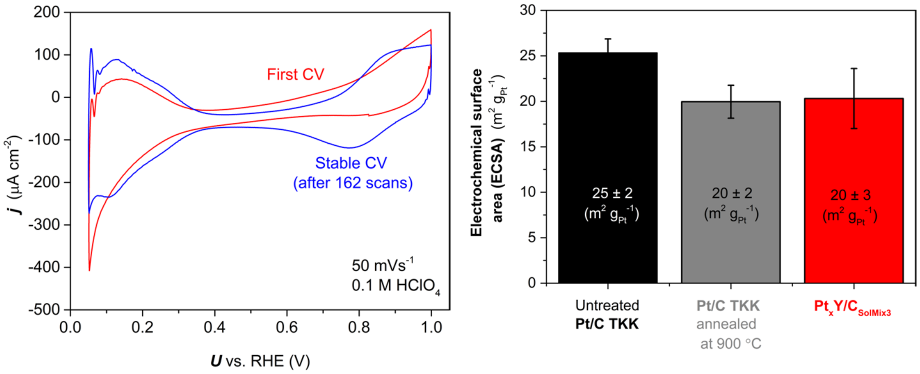

(a) CV's in N_2 saturated electrolyte for $Pt_xY/C_{SolMix3}$

(b) ECSA for $Pt_xY/C_{SolMix3}$ together with TKK Pt/C as recieved and annealed

Figure 6.18: **(a)** CV's in N_2 saturated electrolyte for $Pt_xY/C_{SolMix3}$ showing the initial cycle (red) and the 162nd cycle when the CV is stable (blue) **(b)** The ECSA as determined from CO-stripping for the as recieved and annealed TKK Pt/C (black and grey) and $Pt_xY/C_{SolMix3}$ (red).

Comparing the ECSAs for the synthesised catalyst and that of the seed crystals in figure 6.18b reveal the same as in the quartz reactor. With an ECSA of $20 \pm 3\,\mathrm{m}^2\,\mathrm{g_{Pt}}^{-1}$ the chloride reduction does not affect the ECSA more than annealing the seed particles to a similar temperature. Figure 6.19a shows the anodic sweep of the ORR in 0.1 M $HClO_4$. Here the measurement has been corrected for the capacitance recorded from the CV in N_2 saturated electrolyte. This is done under the assumption that the capacitance is similar in N_2 and O_2 saturated electrolyte. normalising to the measured surface area gives the specific activity seen in figure 6.19b on the left side. Here there is a clear increase over that seen for the as received and annealed TKK Pt/C. Even though the scatter in the measurements indicate inhomogeneity in the catalyst electrodes, all measurement were more active than the reference catalyst. Normalising to the catalyst mass the synthesised catalyst exhibit a significant increase in mass activity increasing from $0.26 \pm 0.01\,\mathrm{A\,mg_{Pt}}^{-1}$ for the annealed TKK Pt/C to $0.41 \pm 0.01\,\mathrm{A\,mg_{Pt}}^{-1}$. This prove that alloying Pt with Y via reduction of the chloride is a viable method for enhancing the catalytic activity towards the ORR. While not reaching the lofty activity of the mass selected nanoparticles, presented in chapter 2, it is an significant improvement over the starting point for the catalyst and well beyond the mass activity of mass selected nanoparticles of Pt with similar size[71] The broad size distribution of the seed catalyst used for the synthesis will also have negative effect on the mass activity of the catalyst. The particles that are to small will not see an improvement in specific activity, due to the excessive overlayer relaxation in these particles. At the same time the particles larger than ∼ 13 nm will see a decline in mass activity as the specific activity reaches its limit at this size.

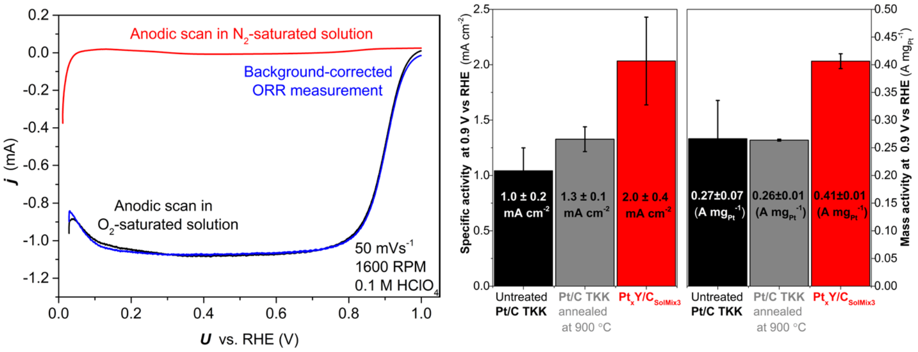

(a) Anodic sweeps for $Pt_xY/C_{SolMix3}$

(b) Specific and mass activity for $Pt_xY/C_{SolMix3}$

Figure 6.19: (a) Anodic sweeps for $Pt_xY/C_{SolMix3}$ in N_2 saturated electrolyte (red), in O_2 saturated electrolyte (black) and the sweep in O_2 corrected for capacitance via the N_2 cycle **(b)**Specific activity on the left and mass activity on the right for for the as recieved and annealed TKK Pt/C (black and grey) and $Pt_xY/C_{SolMix3}$.

6.5 Summary and Discussion

This chapter has established that the synthesis of active Pt-Y alloys is achievable with high temperature reduction. The synthesis of other Pt-RE alloys, such as Pt-Gd and Pt-Tb, was also shown to be achievable. However, further analysis is needed to asses their electrochemical activity. The improved metal reactor lined with carbon allows for better mass transport and distribution of reaction gas. This gives a cleaner alloy, free from pure Pt as the end product. However, this cleaner system also introduces what appears to be a plethora of crystal structures that mitigate the characterisation of the catalyst. Both, Pt_2 Pt_3 and Pt_5 structures could be identified with the possibility for more than two Pt_5 structures and a prosed hexagonal Pt_3 structure. Lowering the amount of precursor did not improve phase selectivity and all phases were produced for the synthesised catalysts with YCl_3. To improve this, further control over the reduction conditions is needed. From the thermodynamic calculations in chapter 4 it was seen that in the mass transport limited cases only Pt_5 structures would be formed until the partial pressure of product gas was reduced. For the catalyst that was only reduced for 100 min all three types of the Pt-Y structures appear, with more Pt_3Y and Pt_xY showing up in the catalyst reduced for the full 360 min. This could indicate that the system is kinetically limited, allowing the formation of all structures at the same time. Another explanation is that neither mass transport or kinetics are any problems and that the reduction time can be reduced significantly. To clarify this, controlled time-temperature series in the improved reactor are needed. Another way to explore the interplay between mass transport and kinetics is to dilute the H_2 flow with Ar. In this way the partial pressure of H_2 can be reduced and the system can be forced into the mass transport limited scenario.

Chapter 7

Conclusion and Outlook

7.1 Conclusion

Through this project it has been the goal to synthesise alloys of platinum and rare earth elements for use as electrocatalysts in fuel cells. This was motivated by the need for sustainable energy sources to be integrated more in transportation to mitigate climate change and ensure energy parity. Fuel cell electric vehicles were presented as a possible solution with the benefits and drawbacks explained. One of which is the poor kinetics of the oxygen reduction reaction provided by the most active single metal catalyst; platinum. In recent years a new group of alloys have seen the light offering vastly improved activity over pure Pt and the potential for long term stability from a strong heat of formation increasing the kinetic barriers for diffusion in the alloy. This group of alloys consists of platinum and rare earth (including yttrium) alloys. However these alloys have never been synthesised in a nanoparticulate form that can be used in fuel cells. This is in large part do to the oxophillic nature of the rare earth elements and their vastly different reduction potential ($< -2.3\,\mathrm{V}$) compared to the standard reduction potential for $\mathrm{Pt}^{2+} \leftrightharpoons \mathrm{Pt}$ of ($+1.18\,\mathrm{V}$). Therefore chapter 4 explored several methods with the potential to reduce the rare earth elements; alkalide reduction, cathodic corrosion and high temperature reduction.
While alkalide reduction proved unsuccessful in the attempts made during the

PhD studies, cathodic corrosion produced what appeared to be pure platinum nanoparticles when examined with XRD, however, the specific activity was higher than expected for pure platinum and metallic yttrium was detected with XPS after the electrochemical measurements. This indicates that even though performed in a water the methods could be capable of reducing the rare earth elements given further optimisation to the conditions for the process. This could include a water free electrolyte with cations that are more electropositive than the element sought to be reduced. From the thermodynamics of high temperature reduction of the rare earth elements together with Pt the tolerances towards water and oxygen were determined. While insurmountable at low temperatures the calculations showed that for the synthesis from oxides in hydrogen containing up to several ppm of water, reduction should be possible from 800 °C and from chlorides the reduction should be possible from 500 °C. The high temperature reduction proved truly successful in producing the alloys with Pt_3Y formed by reducing both an organometallic precursor of yttrium (YCp3) and yttrium chloride (YCl_3) into platinum black.

Chapter 5 expanded on the success of the initial high temperature reduction, by exchanging the platinum black with a carbon supported catalyst from TKK. This catalyst was found to have a broad size distribution, with both sizes above and below the desired range of 6 nm – 12 nm. The YCp3 precursor proved less than optimal, as it decomposed to form insoluble carbides that covered the surface of the catalyst reducing the electrocatalytic activity. The YCl_3 proved capable of producing the alloy on the carbon supported catalyst just as for the unsupported catalyst. However, complications from the reactor design and the increased surface area of the catalyst meant that not all of the Pt was converted to an alloy. The quartz the reactor was made from also proved disadvantageous as the YCl_3 facilitated the reduction of it and the formation of an unwanted PtSi alloy. Modifying the reactor to a horizontal type in stainless steel and separating the precursor mix from the surrounding reactor walls with an inert graphite foil removed this possibility. From this improved setup Pt-Y, Pt-Gd and Pt-Tb alloys were formed and the structures of the different intermetallics between platinum and the rare earth elements were found to be formed simultaneously. Their close relation in structure made their positive identification from XRD patterns difficult, as many of the most intense peaks for the known structures overlaps with each other. An unknown hexagonal Pt_3M structure was even identified as a possible new structure, with a close resemblance to the structure of Pt_5Gd formed on a Gd modified Pt(111) crystal reported in literature.

Even though the structures were not controlled or fully described, the particles did show an improved activity towards the oxygen reduction reaction. The initial seed particles showed a mass activity of $0.27 \pm 0.07\,\mathrm{A\ mg_{Pt}}^{-1}$ with the synthesised particles showing an increased initial activity of $0.41 \pm 0.01\,\mathrm{A\ mg_{Pt}}^{-1}$. This initial gain in activity is far from the reported values for the mass selected nanoparticles prepared by magnetron sputtering, however, this is the first reported synthesis method that has provided high surface area supported nanoparticles of this group of alloys and with further optimisation to the process, it is believed that the mass activity can be improved significantly.

7.2 Outlook

A return to the cathodic corrosion could provide an alternative to the high temperature reduction. Here focus should be on performing the synthesis in a water free environment with cations that are more electropositive than yttrium. With the successful first synthesis of active platinum rare earth alloys the way forward from here is the further elucidation of reduction parameters. While a thermodynamic system was described for the synthesis this is only theoretical and based on data from bulk synthesis. Designing experiments to explore the limits of the mass transport and kinetics of the alloying will prove very useful in controlling the phase purity of the system. This will mainly be needed to avoid the formation of the rare earth rich Pt_2M alloys. Further analysis of the crystal structure will be of academic interest, however, for activity purposes this thought to be less important. A narrower size distribution for the seed particles would be a must for future experiments as this could help increase the gain in mass activity. The optimisation to reduction time and temperature from the proposed studies into the kinetic and mass transport limitations of the system will be able to provide some this in the form of reduced sintering. Otherwise size selective synthesis like pure Pt from cathodic corrosion could be applied,[167,191]. The thermal reduction applied by Schmidt and co-workers could also be adapted to form slightly larger particles.[74] The final goal will be improved mass activity and stability when measured in true MEA setups.

Bibliography

[1] B. Petroleum, "BP statistical review of world energy," Tech. Rep. June, 2015.

[2] International Energy Agency, "CO2 Emissions from Fuel Combustion," tech. rep., Paris, jul 2015.

[3] Gapminder Foundation, "Gapminder tools powered by trendalyzer," May 2016. http://www.gapminder.org/tools/.

[4] The Human Development Report, "Human development index (hdi)," May 2016. http://hdr.undp.org/en/content/human-development-index-hdi.

[5] OECD, "Country statistical profile: China 2016," DOI: http://dx.doi.org/10.1787/csp-chn-table-2016-1-en.

[6] United Nations, "World Population Prospects: The 2015 Revision, Key Findings and Advance Tables," in *Working Paper No. ESA/P/WP.241*, Department of Economic and Social Affairs: Population Division, 2015.

[7] W. Projections, "BP Energy Outlook 2030," tech. rep., 2016.

[8] W. Zittel, J. Zerhusen, and M. Zerta, "Fossil and Nuclear Fuels – the Supply - Outlook," no. March, pp. 1–41, 2013.

[9] D. J. Murphy and C. A. S. Hall, "Year in review-EROI or energy return on (energy) invested," *Annals of the New York Academy of Sciences*, vol. 1185, pp. 102–118, 2010.

[10] M. Raugei and E. Leccisi, “A comprehensive assessment of the energy performance of the full range of electricity generation technologies deployed in the United Kingdom,” *Energy Policy*, vol. 90, pp. 46–59, 2016.

[11] C. Ruehl and J. Giljum, “BP Energy outlook 2030,” Tech. Rep. January, 2011.

[12] IEA, *Energy and Climate Change.* Paris: International Energy Agency, nov 2015.

[13] IEA, “World Energy Outlook 2015 Factsheet: Global energy trends to 2040,” tech. rep., 2015.

[14] S. Solomon, G.-K. Plattner, R. Knutti, and P. Friedlingstein, “Irreversible climate change due to carbon dioxide emissions.,” *Proceedings of the National Academy of Sciences of the United States of America*, vol. 106, pp. 1704–9, feb 2009.

[15] Intergovernmental Panel on Climate change (IPCC), “Climate Change 2014: Synthesis Report,” p. 151, 2014.

[16] UNFCCC, “United nations framework convention on climate change,” May 2016. `http://unfccc.int/essential_background/items/6031.php`.

[17] L. Fulton, P. Cazzola, F. Cuenot, K. Kojima, T. Onoda, J. Staub, and M. Taylor, *Transport, Energy and CO2: MovingTowards Sustainability.* Paris: International Energy Agency, 2009.

[18] F. Kaspar, M. Meinshausen, and M. Schulz, “Climate Change 2014: Mitigation of Climate Change. Contribution of Working Group III to the Fifth Assessment Report of the Intergovern- mental Panel on Climate Change,” pp. 599–670, 2013.

[19] P. Mock, U. Tietge, V. Franco, J. German, A. Bandivadekar, N. Ligterink, U. Lambrecht, J. Kühlwein, and I. Riemersma, “From Laboratory To Road. a 2014 Update of Official and “ Real-World ” Fuel Consumption and CO2 Values for Passenger Cars,” tech. rep., International Council on Clean Transportation Europe, 2014.

[20] Transport & Environment, “Manipulation of fuel economy test results by carmakers: further evidence, costs and solutions,” Tech. Rep. November, Transport & Environment, 2014.

[21] U. Eberle, B. Müller, and R. von Helmolt, “Fuel cell electric vehicles and hydrogen infrastructure: status 2012,” *Energy & Environmental Science*, vol. 5, no. 10, p. 8780, 2012.

[22] C. Bauer, J. Hofer, H.-J. Althaus, A. Del Duce, and A. Simons, “The environmental performance of current and future passenger vehicles: Life Cycle Assessment based on a novel scenario analysis framework,” *Applied Energy*, vol. 157, pp. 1–13, 2015.

[23] T. Franke and J. F. Krems, “What drives range preferences in electric vehicle users?,” *Transport Policy*, vol. 30, pp. 56–62, nov 2013.

[24] O. Egbue and S. Long, “Barriers to widespread adoption of electric vehicles: An analysis of consumer attitudes and perceptions,” *Energy Policy*, vol. 48, pp. 717–729, sep 2012.

[25] O. Gröger, H. a. Gasteiger, and J.-P. Suchsland, “Review—Electromobility: Batteries or Fuel Cells?,” *Journal of The Electrochemical Society*, vol. 162, no. 14, pp. A2605–A2622, 2015.

[26] J. Marcinkoski, J. Spendelow, A. Wilson, and D. Papageorgopoulos, “DOE Hydrogen and Fuel Cells Program Record: On-Road Fuel Cell Stack Durability,” tech. rep., Department of Energy United States of America, 2015.

[27] T. Yoshida and K. Kojima, “Toyota MIRAI Fuel Cell Vehicle and Progress Toward a Future Hydrogen Society,” *Interface magazine*, vol. 24, no. 2, pp. 45–49, 2015.

[28] H. A. Gasteiger and J. Garche, “Fuel Cells,” in *Handbook of Heterogeneous Catalysis:* (G. Ertl, F. Knözinger, and J. Weitkamp, eds.), Weinheim, Germany: Wiley-VCH Verlag GmbH & Co. KGaA, 2008.

[29] F. T. Wagner, B. Lakshmanan, and M. F. Mathias, “Electrochemistry and the Future of the Automobile,” *The Journal of Physical Chemistry Letters*, vol. 1, pp. 2204–2219, jul 2010.

[30] Y.-S. Ye, J. Rick, and B.-J. Hwang, “Water Soluble Polymers as Proton Exchange Membranes for Fuel Cells,” *Polymers*, vol. 4, pp. 913–963, 2012.

[31] J. Larminie and A. Dicks, *Fuel Cell Systems Explained.* Chichester, West Sussex: Wiley & Sons, Ltd, 2nd ed., 2000.

[32] M. Pourbaix, *Atlas of Electrochemical Equilibria in Aqueous Solutions.* Brussels: Pergamont Press, second ed., 1974.

[33] H. A. Gasteiger, S. S. Kocha, B. Sompalli, and F. T. Wagner, “Activity benchmarks and requirements for Pt, Pt-alloy, and non-Pt oxygen reduction catalysts for PEMFCs,” *Applied Catalysis B: Environmental*, vol. 56, pp. 9–35, mar 2005.

[34] P. J. Loferski, “Minerals Yearbook - Platinum Group Metals,” Tech. Rep. August, U.S. Department of the Interior, U.S. Geological Survey August, 2013.

[35] OICA, "WORLD MOTOR VEHICLE PRODUCTION - World Ranking of Manufacturers Year 2011," tech. rep., International Organization of Motor Vehicle Manufacturers, 2013.

[36] A. J. Bard and L. R. Faulkner, *Electrochemical Methods: Fundamentals and applications.* Wiley & Sons, Inc., 2nd ed., 2001.

[37] I. E. L. Stephens, A. S. Bondarenko, U. Grønbjerg, J. Rossmeisl, and I. Chorkendorff, "Understanding the electrocatalysis of oxygen reduction on platinum and its alloys," *Energy & Environmental Science*, vol. 5, no. 5, p. 6744, 2012.

[38] E. Higuchi, H. Uchida, and M. Watanabe, "Effect of loading level in platinum-dispersed carbon black electrocatalysts on oxygen reduction activity evaluated by rotating disk electrode," *Journal of Electroanalytical Chemistry*, vol. 583, pp. 69–76, sep 2005.

[39] By No machine-readable author provided. Smokefoot assumed (based on copyright claims). [Public domain], via Wikimedia Commons, "Catalysisscheme." Online, May 2016. `https://commons.wikimedia.org/wiki/File%3ACatalysisScheme.png`.

[40] J. K. Nørskov, J. Rossmeisl, A. Logadottir, L. Lindqvist, J. R. Kitchin, T. Bligaard, and H. Jónsson, "Origin of the Overpotential for Oxygen Reduction at a Fuel-Cell Cathode," *The Journal of Physical Chemistry B*, vol. 108, pp. 17886–17892, nov 2004.

[41] G. A. Tritsaris, J. Greeley, J. Rossmeisl, and J. K. Nørskov, "Atomic-Scale Modeling of Particle Size Effects for the Oxygen Reduction Reaction on Pt," *Catalysis Letters*, vol. 141, pp. 909–913, jun 2011.

[42] I. Chorkendorff and J. W. Niemantsverdriet, *Concepts of Modern Catalysis and Kinetics.* Weinheim, Germany: Wiley-VCH Verlag GmbH & Co. KGaA, 2011.

[43] P. Sabatier, "Hydrogénations et déshydrogénations par catalyse," *Berichte der deutschen chemischen Gesellschaft*, vol. 44, pp. 1984–2001, jul 1911.

[44] J. Greeley and N. M. Markovic, "The road from animal electricity to green energy: combining experiment and theory in electrocatalysis," *Energy & Environmental Science*, vol. 5, no. 11, p. 9246, 2012.

[45] M. K. Debe, "Electrocatalyst approaches and challenges for automotive fuel cells.," *Nature*, vol. 486, pp. 43–51, jun 2012.

[46] A. Rabis, P. Rodriguez, and T. J. Schmidt, "Electrocatalysis for Polymer Electrolyte Fuel Cells : Recent Achievements and Future Challenges," 2012.

[47] Y. J. Wang, N. Zhao, B. Fang, H. Li, X. T. Bi, and H. Wang, "Carbon-Supported Pt-Based Alloy Electrocatalysts for the Oxygen Reduction Reaction in Polymer Electrolyte Membrane Fuel Cells: Particle Size, Shape, and Composition Manipulation and Their Impact to Activity," *Chemical Reviews*, vol. 115, no. 9, pp. 3433–3467, 2015.

[48] G. S. Karlberg, J. Rossmeisl, and J. K. Nørskov, "Estimations of electric field effects on the oxygen reduction reaction based on the density functional theory.," *Physical chemistry chemical physics : PCCP*, vol. 9, pp. 5158–61, oct 2007.

[49] J. Rossmeisl, G. S. Karlberg, T. Jaramillo, and J. K. Nørskov, "Steady state oxygen reduction and cyclic voltammetry," *Faraday Discussions*, vol. 140, p. 337, 2009.

[50] J. Rossmeisl, A. Logadottir, and J. Nørskov, "Electrolysis of water on (oxidized) metal surfaces," *Chemical Physics*, vol. 319, pp. 178–184, dec 2005.

[51] V. Tripković, E. Skúlason, S. Siahrostami, J. K. Nørskov, and J. Rossmeisl, "The oxygen reduction reaction mechanism on Pt(111) from density functional theory calculations," *Electrochimica Acta*, vol. 55, pp. 7975–7981, nov 2010.

[52] A. K. Jepsen, *Stability and Activity of New Alloy Catalysts for the Oxygen Reduction Reaction under Acidic Conditions.* PhD thesis, Technical University of Denmark, 2012.

[53] F. Abild-Pedersen, J. Greeley, F. Studt, J. Rossmeisl, T. Munter, P. Moses, E. Skúlason, T. Bligaard, and J. Nørskov, "Scaling Properties of Adsorption Energies for Hydrogen-Containing Molecules on Transition-Metal Surfaces," *Physical Review Letters*, vol. 99, pp. 4–7, jul 2007.

[54] F. Calle-Vallejo, J. I. Martínez, J. M. García-Lastra, J. Rossmeisl, and M. T. M. Koper, "Physical and Chemical Nature of the Scaling Relations between Adsorption Energies of Atoms on Metal Surfaces," *Physical Review Letters*, vol. 108, p. 116103, mar 2012.

[55] I. E. L. Stephens, A. S. Bondarenko, F. J. Perez-Alonso, F. Calle-Vallejo, L. Bech, T. P. Johansson, A. K. Jepsen, R. Frydendal, B. P. Knudsen, J. Rossmeisl, and I. Chorkendorff, "Tuning the activity of Pt(111) for oxygen electroreduction by subsurface alloying.," *Journal of the American Chemical Society*, vol. 133, pp. 5485–91, apr 2011.

[56] M. Watanabe and S. Motoo, "Electrocatalysis by ad-atoms: Part II. Enhancement of the oxidation of methanol on platinum by ruthenium adatoms," *Journal of Electroanalytical Chemistry and Interfacial Electrochemistry*, vol. 60, pp. 267–273, apr 1975.

[57] T. Yajima, N. Wakabayashi, H. Uchida, and M. Watanabe, "Adsorbed water for the electro-oxidation of methanol at Pt–Ru alloy," *Chemical Communications*, pp. 828–829, mar 2003.

[58] B. Hammer and J. Nørskov, "Electronic factors determining the reactivity of metal surfaces," *Surface Science*, vol. 343, pp. 211–220, dec 1995.

[59] B. Hammer and J. K. Nørskov, "Why Gold Is the Noblest of All the Metals," *Nature*, vol. 376, no. 6537, pp. 238–240, 1995.

[60] B. Hammer, Y. Morikawa, and J. Nørskov, "CO Chemisorption at Metal Surfaces and Overlayers," *Physical Review Letters*, vol. 76, no. 12, pp. 2141–2144, 1996.

[61] A. Ruban, B. Hammer, P. Stoltze, H. Skriver, and J. Nørskov, "Surface electronic structure and reactivity of transition and noble metals1Communication presented at the First Francqui Colloquium, Brussels, 19–20 February 1996.1," *Journal of Molecular Catalysis A: Chemical*, vol. 115, pp. 421–429, feb 1997.

[62] J. R. Kitchin, N. A. Khan, M. A. Barteau, J. G. Chen, B. Yakshinskiy, and T. E. Madey, "Elucidation of the active surface and origin of the weak metal-hydrogen bond on Ni/Pt(1 1 1) bimetallic surfaces: A surface science and density functional theory study," *Surface Science*, vol. 544, no. 2-3, pp. 295–308, 2003.

[63] J. R. Kitchin, J. K. Nørskov, M. a. Barteau, and J. G. Chen, "Modification of the surface electronic and chemical properties of Pt(111) by subsurface 3d transition metals.," *The Journal of chemical physics*, vol. 120, pp. 10240–6, jun 2004.

[64] M. Mavrikakis, B. Hammer, and J. Nørskov, "Effect of Strain on the Reactivity of Metal Surfaces," *Physical Review Letters*, vol. 81, pp. 2819–2822, sep 1998.

[65] T. Bligaard and J. Nørskov, "Ligand effects in heterogeneous catalysis and electrochemistry," *Electrochimica Acta*, vol. 52, pp. 5512–5516, may 2007.

[66] (U.S. Department of Energy), "Fuel Cell Technical Team Roadmap," *Usdrive*, no. June, p. 9, 2013.

[67] A. Ohma, K. Shinohara, A. Iiyama, T. Yoshida, and A. Daimaru, "Membrane and Catalyst Performance Targets for Automotive Fuel Cells by FCCJ Membrane, Catalyst, MEA WG," vol. 41, pp. 775–784, 2011.

[68] H. a. Gasteiger and N. M. Marković, "Just a dream–or future reality?," *Science (New York, N.Y.)*, vol. 324, pp. 48–9, apr 2009.

[69] K. Kinoshita, *Electrochemical oxygen technology*, vol. 30. John Wiley & Sons, 1992.

[70] G. a. Tritsaris, J. Greeley, J. Rossmeisl, and J. K. Nørskov, "Atomic-Scale Modeling of Particle Size Effects for the Oxygen Reduction Reaction on Pt," *Catalysis Letters*, vol. 141, pp. 909–913, jun 2011.

[71] F. J. Perez-Alonso, D. N. McCarthy, A. Nierhoff, P. Hernandez-Fernandez, C. Strebel, I. E. L. Stephens, J. H. Nielsen, and I. Chorkendorff, "The effect of size on the oxygen electroreduction activity of mass-selected platinum nanoparticles.," *Angewandte Chemie (International ed. in English)*, vol. 51, pp. 4641–3, may 2012.

[72] M. Nesselberger, S. Ashton, J. C. Meier, I. Katsounaros, K. J. J. Mayrhofer, and M. Arenz, "The particle size effect on the oxygen reduction reaction activity of Pt catalysts: influence of electrolyte and relation to single crystal models.," *Journal of the American Chemical Society*, vol. 133, pp. 17428–33, nov 2011.

[73] E. Fabbri, S. Taylor, A. Rabis, P. Levecque, O. Conrad, R. Kötz, and T. J. Schmidt, "The effect of platinum nanoparticle distribution on oxygen electroreduction activity and selectivity," *ChemCatChem*, vol. 6, no. 5, pp. 1410–1418, 2014.

[74] S. Taylor, E. Fabbri, P. Levecque, T. J. Schmidt, and O. Conrad, "The Effect of Platinum Loading and Surface Morphology on Oxygen Reduction Activity," *Electrocatalysis*, pp. 287–296, 2016.

[75] M. Nesselberger, M. Roefzaad, R. F. Hamou, P. U. Biedermann, F. F. Schweinberger, S. Kunz, K. Schloegl, G. K. H. Wiberg, S. Ashton, U. Heiz, K. J. J. Mayrhofer, and M. Arenz, "The effect of particle proximity on the oxygen reduction rate of size-selected platinum clusters.," *Nature materials*, vol. 12, pp. 919–24, oct 2013.

[76] W. Liu, P. Rodriguez, L. Borchardt, A. Foelske, J. Yuan, A. K. Herrmann, D. Geiger, Z. Zheng, S. Kaskel, N. Gaponik, R. Kötz, T. J. Schmidt, and A. Eychmüller, "Bimetallic aerogels: High-performance electrocatalysts for the oxygen reduction reaction," *Angewandte Chemie - International Edition*, vol. 52, no. 37, pp. 9849–9852, 2013.

[77] W. Liu, A. K. Herrmann, N. C. Bigall, P. Rodriguez, D. Wen, M. Oezaslan, T. J. Schmidt, N. Gaponik, and A. Eychmüller, "Noble metal aerogels-synthesis, characterization, and application as electrocatalysts," *Accounts of Chemical Research*, vol. 48, no. 2, pp. 154–162, 2015.

[78] Y. Shao-Horn, W. C. Sheng, S. Chen, P. J. Ferreira, E. F. Holby, and D. Morgan, “Instability of Supported Platinum Nanoparticles in Low-Temperature Fuel Cells,” *Topics in Catalysis*, vol. 46, pp. 285–305, nov 2007.

[79] V. Stamenković, T. J. Schmidt, P. N. Ross, and N. M. Marković, “Surface Composition Effects in Electrocatalysis: Kinetics of Oxygen Reduction on Well-Defined Pt 3 Ni and Pt 3 Co Alloy Surfaces,” *The Journal of Physical Chemistry B*, vol. 106, pp. 11970–11979, nov 2002.

[80] V. Stamenkovic, B. S. Mun, K. J. J. Mayrhofer, P. N. Ross, N. M. Markovic, J. Rossmeisl, J. Greeley, and J. K. Nørskov, “Changing the activity of electrocatalysts for oxygen reduction by tuning the surface electronic structure.,” *Angewandte Chemie (International ed. in English)*, vol. 45, pp. 2897–901, apr 2006.

[81] V. R. Stamenkovic, B. S. Mun, M. Arenz, K. J. J. Mayrhofer, C. a. Lucas, G. Wang, P. N. Ross, and N. M. Markovic, “Trends in electrocatalysis on extended and nanoscale Pt-bimetallic alloy surfaces.,” *Nature materials*, vol. 6, pp. 241–7, mar 2007.

[82] V. Stamenković, T. Schmidt, P. Ross, and N. Marković, “Surface segregation effects in electrocatalysis: kinetics of oxygen reduction reaction on polycrystalline Pt3Ni alloy surfaces,” *Journal of Electroanalytical Chemistry*, vol. 554-555, pp. 191–199, sep 2003.

[83] V. R. Stamenkovic, B. S. Mun, K. J. J. Mayrhofer, P. N. Ross, and N. M. Markovic, “Effect of surface composition on electronic structure, stability, and electrocatalytic properties of Pt-transition metal alloys: Pt-skin versus Pt-skeleton surfaces.,” *Journal of the American Chemical Society*, vol. 128, pp. 8813–9, jul 2006.

[84] V. R. Stamenkovic, B. Fowler, B. S. Mun, G. Wang, P. N. Ross, C. A. Lucas, and N. M. Marković, “Improved oxygen reduction activity on Pt3Ni(111) via increased surface site availability.,” *Science (New York, N.Y.)*, vol. 315, pp. 493–7, jan 2007.

[85] S.-I. Choi, S. Xie, M. Shao, J. H. Odell, N. Lu, H.-C. Peng, L. Protsailo, S. Guerrero, J. Park, X. Xia, J. Wang, M. J. Kim, and Y. Xia, “Synthesis and Characterization of 9 nm Pt–Ni Octahedra with a Record High Activity of 3.3 A/mg Pt for the Oxygen Reduction Reaction,” *Nano Letters*, vol. 13, pp. 3420–3425, jul 2013.

[86] S. Chen, P. J. Ferreira, W. Sheng, N. Yabuuchi, L. F. Allard, and Y. Shao-Horn, “Enhanced activity for oxygen reduction reaction on "Pt3Co" nanoparticles: direct evidence of percolated and sandwich-segregation

structures.," *Journal of the American Chemical Society*, vol. 130, no. 42, pp. 13818–13819, 2008.

[87] M. K. Carpenter, T. E. Moylan, R. S. Kukreja, M. H. Atwan, and M. M. Tessema, "Solvothermal Synthesis of Platinum Alloy Nanoparticles for Oxygen Reduction Electrocatalysis," *Journal of the American Chemical Society*, vol. 134, pp. 8535–8542, may 2012.

[88] C. Cui, L. Gan, M. Heggen, S. Rudi, and P. Strasser, "Compositional segregation in shaped Pt alloy nanoparticles and their structural behaviour during electrocatalysis," *Nature Materials*, vol. 12, no. 8, pp. 765–771, 2013.

[89] D. Wang, H. L. Xin, R. Hovden, H. Wang, Y. Yu, D. a. Muller, F. J. DiSalvo, and H. D. Abruña, "Structurally ordered intermetallic platinum–cobalt core–shell nanoparticles with enhanced activity and stability as oxygen reduction electrocatalysts," *Nature Materials*, vol. 12, pp. 81–87, oct 2012.

[90] S.-i. Choi, M. Shao, N. Lu, A. Ruditskiy, H.-c. Peng, J. Park, S. Guerrero, J. Wang, M. J. Kim, and Y. Xia, "Synthesis and Characterization of Pd@Pt–Ni Core–Shell Octahedra with High Activity toward Oxygen Reduction," *ACS Nano*, vol. 8, pp. 10363–10371, oct 2014.

[91] X. Huang, Z. Zhao, L. Cao, Y. Chen, E. Zhu, Z. Lin, M. Li, A. Yan, A. Zettl, Y. M. Wang, X. Duan, T. Mueller, and Y. Huang, "High-performance transition metal – doped Pt3Ni octahedra for oxygen reduction reaction," *Science*, vol. 348, no. 2009, pp. 1230–1234, 2015.

[92] C. Chen, Y. Kang, Z. Huo, Z. Zhu, W. Huang, H. L. Xin, J. D. Snyder, D. Li, J. A. Herron, M. Mavrikakis, M. Chi, K. L. More, Y. Li, N. M. Markovic, G. A. Somorjai, P. Yang, and V. R. Stamenkovic, "Highly Crystalline Multimetallic Nanoframes with Three-Dimensional Electrocatalytic Surfaces," *Science*, vol. 343, pp. 1339–1343, mar 2014.

[93] S. Koh and P. Strasser, "Electrocatalysis on bimetallic surfaces: modifying catalytic reactivity for oxygen reduction by voltammetric surface dealloying.," *Journal of the American Chemical Society*, vol. 129, pp. 12624–5, oct 2007.

[94] P. Strasser, Z. Liu, and S. Koh, "Aging Studies of Voltammetrically Dealloyed Pt-Cu Nanoparticle ORR Electrocatalysts," in *ECS Transactions*, vol. 16, pp. 515–522, ECS, 2008.

[95] P. Mani, R. Srivastava, and P. Strasser, "Dealloyed Pt-Cu Core-Shell Nanoparticle Electrocatalysts for Use in PEM Fuel Cell Cathodes," *Journal of Physical Chemistry C*, vol. 112, pp. 2770–2778, feb 2008.

[96] K. Neyerlin, R. Srivastava, C. Yu, and P. Strasser, "Electrochemical activity and stability of dealloyed Pt–Cu and Pt–Cu–Co electrocatalysts for the oxygen reduction reaction (ORR)," *Journal of Power Sources*, vol. 186, pp. 261–267, jan 2009.

[97] P. Strasser, S. Koh, T. Anniyev, J. Greeley, K. More, C. Yu, Z. Liu, S. Kaya, D. Nordlund, H. Ogasawara, M. F. Toney, and A. Nilsson, "Lattice-strain control of the activity in dealloyed core–shell fuel cell catalysts," *Nature Chemistry*, vol. 2, pp. 454–460, jun 2010.

[98] F. Hasché, M. Oezaslan, and P. Strasser, "Activity, Stability, and Degradation Mechanisms of Dealloyed PtCu3 and PtCo3 Nanoparticle Fuel Cell Catalysts," *ChemCatChem*, pp. n/a–n/a, 2011.

[99] B. Han, C. E. Carlton, A. Kongkanand, R. S. Kukreja, B. R. Theobald, L. Gan, R. O'Malley, P. Strasser, F. T. Wagner, and Y. Shao-Horn, "Record activity and stability of dealloyed bimetallic catalysts for proton exchange membrane fuel cells," *Energy Environ. Sci.*, vol. 8, no. 1, pp. 258–266, 2015.

[100] I. E. L. Stephens, A. S. Bondarenko, F. J. Perez-Alonso, F. Calle-Vallejo, L. Bech, T. P. Johansson, A. K. Jepsen, R. Frydendal, B. P. Knudsen, J. Rossmeisl, and I. Chorkendorff, "Tuning the activity of Pt(111) for oxygen electroreduction by subsurface alloying.," *Journal of the American Chemical Society*, vol. 133, pp. 5485–91, apr 2011.

[101] D. Wang, Y. Yu, H. L. Xin, R. Hovden, P. Ercius, J. a. Mundy, H. Chen, J. H. Richard, D. a. Muller, F. J. DiSalvo, and H. D. Abruña, "Tuning oxygen reduction reaction activity via controllable dealloying: a model study of ordered Cu3Pt/C intermetallic nanocatalysts.," *Nano letters*, vol. 12, pp. 5230–8, oct 2012.

[102] S. Chen, H. a. Gasteiger, K. Hayakawa, T. Tada, and Y. Shao-Horn, "Platinum-Alloy Cathode Catalyst Degradation in Proton Exchange Membrane Fuel Cells: Nanometer-Scale Compositional and Morphological Changes," *Journal of The Electrochemical Society*, vol. 157, no. 1, p. A82, 2010.

[103] L. Gan, C. Cui, S. Rudi, and P. Strasser, "Core-shell and nanoporous particle architectures and their effect on the activity and stability of Pt ORR electrocatalysts," *Topics in Catalysis*, vol. 57, no. 1-4, pp. 236–244, 2014.

[104] R. Makharia, S. Kocha, P. Yu, M. A. Sweikart, W. Gu, F. Wagner, and H. a. Gasteiger, "Durable PEM Fuel Cell Electrode Materials: Requirements and Benchmarking Methodologies," in *ECS Transactions*, vol. 1, pp. 3–18, ECS, 2006.

[105] F. Maillard, L. Dubau, J. Durst, M. Chatenet, J. André, and E. Rossinot, "Durability of Pt3Co/C nanoparticles in a proton-exchange membrane fuel cell: Direct evidence of bulk Co segregation to the surface," *Electrochemistry Communications*, vol. 12, no. 9, pp. 1161–1164, 2010.

[106] L. Dubau, F. Maillard, M. Chatenet, L. Guetaz, J. André, and E. Rossinot, "Durability of Pt3Co/C Cathodes in a 16 Cell PEMFC Stack: Macro/Microstructural Changes and Degradation Mechanisms," *Journal of The Electrochemical Society*, vol. 157, no. 12, p. B1887, 2010.

[107] R. Makharia, S. Kocha, P. Yu, M. A. Sweikart, W. Gu, F. Wagner, and H. A. Gasteiger, "Durable PEM Fuel Cell Electrode Materials: Requirements and Benchmarking Methodologies," *ECS Transactions*, vol. 1, no. 8, pp. 3–18, 2006.

[108] M. Arenz and A. Zana, "Fuel cell catalyst degradation: Identical location electron microscopy and related methods," *Nano Energy*, pp. 1–15, 2015.

[109] A. S. Mezzavilla, S. Cherevko, C. Baldizzone, E. Pizzutilo, G. Polymeros, K. J. J. Mayrhofer, S. Mezzavilla, S. Cherevko, C. Baldizzone, E. Pizzutilo, and G. Polymeros, "Experimental methodologies to understand the degradation of nanostructured electrocatalysts for PEM fuel cells : advances and opportunities," pp. 1–14, 2016.

[110] T. Nagai, H. Murata, and Y. Morimoto, "Influence of Experimental Conditions on the Catalyst Degradation in the Durability Test," *Journal of The Electrochemical Society*, vol. 161, no. 6, pp. F789–F794, 2014.

[111] S. Cherevko, G. P. Keeley, S. Geiger, A. R. Zeradjanin, N. Hodnik, N. Kulyk, and K. J. J. Mayrhofer, "Dissolution of Platinum in the Operational Range of Fuel Cells," *ChemElectroChem*, vol. 2, no. 10, pp. 1471–1478, 2015.

[112] J. Erlebacher and D. Margetis, "Mechanism of Hollow Nanoparticle Formation Due to Shape Fluctuations," *Physical Review Letters*, vol. 112, no. 15, p. 155505, 2014.

[113] G. Wu, K. L. More, C. M. Johnston, and P. Zelenay, "High-Performance Electrocatalysts for Oxygen Reduction Derived from Polyaniline, Iron, and Cobalt," *Science*, vol. 332, pp. 443–447, apr 2011.

[114] Y. Hu, J. O. Jensen, W. Zhang, L. N. Cleemann, W. Xing, N. J. Bjerrum, and Q. Li, "Hollow Spheres of Iron Carbide Nanoparticles Encased in Graphite Layers as Oxygen Reduction Catalysts," *Angewandte Chemie International Edition*, pp. n/a–n/a, feb 2014.

[115] U. G. Vej-Hansen, J. Rosmeisl, I. Stephens, and J. Schiøtz, “Correlation between diffusion barriers and alloying energy in binary alloys,” *Phys. Chem. Chem. Phys.*, pp. 3302–3307, 2015.

[116] J. Greeley, I. E. L. Stephens, a. S. Bondarenko, T. P. Johansson, H. a. Hansen, T. F. Jaramillo, J. Rossmeisl, I. Chorkendorff, and J. K. Nørskov, “Alloys of platinum and early transition metals as oxygen reduction electrocatalysts.,” *Nature chemistry*, vol. 1, pp. 552–6, oct 2009.

[117] I. E. L. Stephens, A. S. Bondarenko, L. Bech, and I. Chorkendorff, “Oxygen Electroreduction Activity and X-Ray Photoelectron Spectroscopy of Platinum and Early Transition Metal Alloys,” *ChemCatChem*, vol. 4, pp. 341–349, mar 2012.

[118] M. Escudero-Escribano, A. Verdaguer-Casadevall, P. Malacrida, U. Grønbjerg, B. P. Knudsen, A. K. Jepsen, J. Rossmeisl, I. E. L. Stephens, and I. Chorkendorff, “Pt5Gd as a highly active and stable catalyst for oxygen electroreduction.,” *Journal of the American Chemical Society*, vol. 134, pp. 16476–9, oct 2012.

[119] M. Escudero-Escribano, P. Malacrida, M. H. Hansen, U. G. Vej-Hansen, A. Velazquez-Palenzuela, V. Tripkovic, J. Schiotz, J. Rossmeisl, I. E. L. Stephens, and I. Chorkendorff, “Tuning the activity of Pt alloy electrocatalysts by means of the lanthanide contraction,” *Science*, vol. 352, pp. 73–76, apr 2016.

[120] P. Malacrida, M. Escudero-Escribano, A. Verdaguer-Casadevall, I. E. L. Stephens, and I. Chorkendorff, “Enhanced activity and stability of Pt–La and Pt–Ce alloys for oxygen electroreduction: the elucidation of the active surface phase,” *Journal of Materials Chemistry A*, vol. 2, no. 12, p. 4234, 2014.

[121] R. Hultgren, U. S. atomic energy commission., A. iron, A. society for metals., AEC., ASM., and USAEC., *Selected values of the thermodynamic properties of binary alloys.* 1973.

[122] H. Kleykamp, “Thermodynamics of the systems of the platinum metals with other transition metals: I. Integral data,” *Journal of Nuclear Materials*, vol. 201, no. C, pp. 193–217, 1993.

[123] R. Walker and J. Darby, “Thermodynamic properties of solid nickel-platinum alloys,” *Acta Metallurgica*, vol. 18, pp. 1261–1266, dec 1970.

[124] R. Pretorius, T. Marais, and C. Theron, “Thin film compound phase formation sequence: An effective heat of formation model,” *Materials Science Reports*, vol. 10, pp. 1–83, jul 1993.

[125] K. Jacob and Y. Waseda, "Gibbs energies of formation of rare earth MPt5 compounds," *Thermochimica Acta*, vol. 165, pp. 223–233, aug 1990.

[126] U. G. Vej-Hansen, *Structure, activity, and stability of platinum alloys as catalysts for the oxygen reduction reaction.* Phd thesis, Technical University of Denmark, 2015.

[127] B. Han, C. E. Carlton, J. Suntivich, Z. Xu, and Y. Shao-Horn, "Oxygen reduction activity and stability trends of bimetallic Pt0.5M0.5 nanoparticle in acid," *Journal of Physical Chemistry C*, vol. 119, no. 8, pp. 3971–3978, 2015.

[128] T. P. Johansson, E. T. Ulrikkeholm, P. Hernandez-Fernandez, M. Escudero-Escribano, P. Malacrida, I. E. L. Stephens, and I. Chorkendorff, "Towards the elucidation of the high oxygen electroreduction activity of PtxY: surface science and electrochemical studies of Y/Pt(111).," *Physical chemistry chemical physics : PCCP*, vol. 16, pp. 13718–25, jul 2014.

[129] E. T. Ulrikkeholm, A. F. Pedersen, U. G. Vej-Hansen, M. Escudero-Escribano, I. E. Stephens, D. Friebel, A. Mehta, J. Schiøtz, R. K. Feidenhansl', A. Nilsson, and I. Chorkendorff, "PtxGd alloy formation on Pt(111): Preparation and structural characterization," *Surface Science*, feb 2016.

[130] A. F. Pedersen, E. T. Ulrikkeholm, M. Escudero-Escribano, T. P. Johansson, P. Malacrida, C. M. Pedersen, M. H. Hansen, K. D. Jensen, J. Rossmeisl, D. Friebel, A. Nilsson, I. Chorkendorff, and I. E. Stephens, "Probing the nanoscale structure of the catalytically active overlayer on Pt alloys with rare earths," *Nano Energy*, pp. 1–12, 2016.

[131] P. Hernandez-Fernandez, F. Masini, D. N. McCarthy, C. E. Strebel, D. Friebel, D. Deiana, P. Malacrida, A. Nierhoff, A. Bodin, A. M. Wise, J. H. Nielsen, T. W. Hansen, A. Nilsson, I. E. L. Stephens, and I. Chorkendorff, "Mass-selected nanoparticles of PtxY as model catalysts for oxygen electroreduction.," *Nature chemistry*, vol. 6, pp. 732–8, aug 2014.

[132] A. Velázquez-Palenzuela, F. Masini, A. F. Pedersen, M. Escudero-Escribano, D. Deiana, P. Malacrida, T. W. Hansen, D. Friebel, A. Nilsson, I. E. Stephens, and I. Chorkendorff, "The enhanced activity of mass-selected PtxGd nanoparticles for oxygen electroreduction," *Journal of Catalysis*, vol. 328, pp. 297–307, aug 2015.

[133] D. Deiana, J. B. Wagner, and T. W. Hansen, "Structure and Stability of Pt-Y Alloy Particles for Oxygen Reduction Studied by Electron Microscopy," *ECS Transactions*, vol. 66, pp. 115–127, may 2015.

[134] B. P. Knudsen, *Synthesis and Test of New Platinum Alloy Electro Catalysts.* Msc. thesis, Technical University of Denmark, 2012.

[135] C. M. Pedersen, M. Escudero-Escribano, A. Velázquez-Palenzuela, L. H. Christensen, I. Chorkendorff, and I. E. L. Stephens, "Benchmarking Pt-based electrocatalysts for low temperature fuel cell reactions with the rotating disk electrode: Oxygen reduction and hydrogen oxidation in the presence of CO (review article)," *Electrochimica Acta*, vol. 179, pp. 647–657, 2015.

[136] D. Deiana, *Atomic-level Electron Microscopy of Metal and Alloy Electrocatalysts.* PhD thesis, Technical University of Denmark, 2014.

[137] J. L. Moriarty, J. E. Humphreys, R. O. Gordon, and N. C. Baenziger, "X-ray examination of some rare-earth-containing binary alloy systems," *Acta Crystallographica*, vol. 21, no. 5, pp. 840–841, 1966.

[138] N. C. Baenziger and J. L. Moriarty, "Gadolinium and dyprosium intermetallic phases. II. Laves phases and other structure types," *Acta Crystallographica*, vol. 14, pp. 948–950, 1961.

[139] N. Baenziger and J. Moriarty, "Gadolinium and dysprosium intermetallic phases. I. The crystal structures of DyGa and GdPt and their related compounds," *Acta Crystallographica*, vol. 14, pp. 946–947, 1961.

[140] R. F. Berger, S. Lee, J. Johnson, B. Nebgen, and A. C.-Y. So, "Laves Phases, γ -Brass, and 2x2x2 Superstructures: A New Class of Quasicrystal Approximants and the Suggestion of a New Quasicrystal," *Chemistry - A European Journal*, vol. 14, pp. 6627–6639, jul 2008.

[141] B. T. Kilbourn, "A LANTHANIDE LANTHOLOGY Part II: M-Z," in *A LANTHANIDE LANTHOLOGY*, Mountain Pass: Molycorp, Inc, 1993.

[142] W. Bronger, "Preparation and x-ray investigation of platinumalloys with the rare-earth metals (Pt5Ln and Pt3Ln Phases)," *Journal of the Less Common Metals*, vol. 12, 1967.

[143] B. Erdmann, "Darstellung von Actiniden-Lanthaniden-Edelmetall (Pt, Pd, Ir, Rh)-Legierungsphasen durch gekoppelte Reduktion," *Kernforschungszentrum Karlsruhe Report*, 1971.

[144] C. Keller and B. Erdmann, "Actinide (Lanthanide) -Noble Metal Alloy Phases , Preparation and Properties," *Journal of Solid State Chemistry*, vol. 7, pp. 40–48, 1973.

[145] A. E. Dwight, J. W. Downey, and R. A. Conner Jr., "Some AB3 compounds of the transitiom metals," *Acta Crystallographica*, vol. 14, no. 1, pp. 75–76, 1961.

[146] T. H. Geballe, B. T. Matthias, V. B. Compton, E. Corenzwit, G. W. Hull, and L. D. Longinotti, “Superconductivity in Binary Alloy Systems of the Rare Earths and of Thorium with Pt-Group Metals,” *Physical Review*, vol. 137, pp. A119–A127, jan 1965.

[147] N. Krikorian, “The reaction of selected lanthanide carbides with platinum and iridium,” *Journal of the Less Common Metals*, vol. 23, pp. 271–279, mar 1971.

[148] K. W. Lux and E. J. Cairns, “Lanthanide–Platinum Intermetallic Compounds as Anode Electrocatalysts for Direct Ethanol PEM Fuel Cells : Synthesis and Characterization of LnPt2 (Ln = Ce, Pr) Nanopowders,” *Journal of The Electrochemical Society*, vol. 153, no. 6, p. A1139, 2006.

[149] K. W. Lux and E. J. Cairns, “Lanthanide–Platinum Intermetallic Compounds as Anode Electrocatalysts for Direct Ethanol PEM Fuel Cells : II. Performance of Nanopowders in an Operating PEM Fuel Cell,” *Journal of The Electrochemical Society*, vol. 153, no. 6, p. A1139, 2006.

[150] M. K. Jeon and P. J. McGinn, “Carbon supported Pt–Y electrocatalysts for the oxygen reduction reaction,” *Journal of Power Sources*, vol. 196, pp. 1127–1131, feb 2011.

[151] SpringerMaterials, “Thermodynamic Properties of Compounds, RuO3 to Ti3O5,” in *Pure Substances. Part 4 _ Compounds from HgH_g to ZnTe_g*, vol. 19A4 of *Landolt-Börnstein - Group IV Physical Chemistry*, pp. 325–350, Berlin/Heidelberg: Springer-Verlag, 2001.

[152] X. Liu, E. H. Yu, and K. Scott, “Preparation and evaluation of a highly stable palladium yttrium platinum core–shell–shell structure catalyst for oxygen reduction reactions,” *Applied Catalysis B: Environmental*, vol. 162, pp. 593–601, jan 2015.

[153] K. Nishanth, P. Sridhar, and S. Pitchumani, “Enhanced oxygen reduction reaction activity through spillover effect by Pt–Y(OH)3/C catalyst in direct methanol fuel cells,” *Electrochemistry Communications*, vol. 13, pp. 1465–1468, dec 2011.

[154] Y. Luo, A. Habrioux, L. Calvillo, G. Granozzi, and N. Alonso-Vante, “Yttrium Oxide/Gadolinium Oxide-Modified Platinum Nanoparticles as Cathodes for the Oxygen Reduction Reaction,” *ChemPhysChem*, vol. 15, pp. 2136–2144, jul 2014.

[155] D. Saha, E. D. Bøjesen, K. M. Ø. Jensen, A.-C. Dippel, and B. B. Iversen, “Formation Mechanisms of Pt and Pt 3 Gd Nanoparticles under Solvothermal Conditions: An in Situ Total X-ray Scattering Study,” *The Journal of Physical Chemistry C*, vol. 119, pp. 13357–13362, jun 2015.

[156] J. L. Dye and K.-l. Tsai, "Small alloy particles formed by Co-reduction of soluble precursors with alkalides or electrides in aprotic solvents," *Faraday Discussions*, vol. 92, p. 45, 1991.

[157] K.-l. Tsai and J. L. Dye, "Synthesis , Properties , and Characterization of Nanometer-Size Metal Particles by Homogeneous Reduction with Alkalides and Electrides in Aprotic Solvents," vol. 5, no. 13, pp. 540–546, 1993.

[158] M. J. Wagner and J. L. Dye, "Alkalides, Electrides, and Expanded Metals," *Annual Review of Materials Science*, vol. 23, pp. 223–253, aug 1993.

[159] J. a. Nelson, L. H. Bennett, and M. J. Wagner, "Solution synthesis of gadolinium nanoparticles.," *Journal of the American Chemical Society*, vol. 124, pp. 2979–83, mar 2002.

[160] J. A. Nelson and M. J. Wagner, "Yttrium Oxide Nanoparticles Prepared by Alkalide Reduction," no. 15, pp. 915–917, 2002.

[161] C. Yan and M. J. Wagner, "Air- and water-stable gold-coated gadolinium metal nanocrystals.," *Nano letters*, vol. 13, pp. 2611–4, may 2013.

[162] S.-B. Han, "Electrodeposited Nanoporous PtY Alloy Electrodes with Enhanced Oxygen Reduction Reaction," *International Journal of Electrochemical Science*, vol. 11, pp. 3803–3814, 2016.

[163] W. Zhou, J. Wu, and H. Yang, "Highly uniform platinum icosahedra made by hot injection-assisted GRAILS method.," *Nano letters*, vol. 13, pp. 2870–4, jun 2013.

[164] E. Bennett, J. Monzó, J. Humphrey, D. Plana, M. Walker, C. McConville, D. Fermin, A. Yanson, and P. Rodriguez, "A Synthetic Route for the Effective Preparation of Metal Alloy Nanoparticles and Their Use as Active Electrocatalysts," *ACS Catalysis*, vol. 6, no. 3, pp. 1533–1539, 2016.

[165] A. I. Yanson, P. Rodriguez, N. Garcia-Araez, R. V. Mom, F. D. Tichelaar, and M. T. M. Koper, "Cathodic corrosion: a quick, clean, and versatile method for the synthesis of metallic nanoparticles.," *Angewandte Chemie (International ed. in English)*, vol. 50, pp. 6346–50, jul 2011.

[166] P. Rodriguez, F. D. Tichelaar, M. T. M. Koper, and A. I. Yanson, "Cathodic corrosion as a facile and effective method to prepare clean metal alloy nanoparticles.," *Journal of the American Chemical Society*, vol. 133, pp. 17626–9, nov 2011.

[167] a. I. Yanson, P. V. Antonov, P. Rodriguez, and M. T. M. Koper, "Influence of the electrolyte concentration on the size and shape of platinum nanoparticles synthesized by cathodic corrosion," *Electrochimica Acta*, pp. 1–6, jan 2013.

[168] D. Brandon and B. Kaplan, *Microstructural Characterization of Materials.* Wiley & Sons, Ltd, 2nd ed., 2008.

[169] L. W. Finger, D. E. Cox, and A. P. Jephcoat, "A correction for powder diffraction peak asymmetry due to axial divergence," *Journal of Applied Crystallography*, vol. 27, pp. 892–900, Dec 1994.

[170] J. Bolze, D. Beckers, and V. Kogan, "Size Distribution Determination of Nanoparticles and Nanosized Pores by Small-Angle X-Ray Scattering (SAXS) on a Multi-Purpose X-Ray Diffractometer," tech. rep., PANalytical.

[171] H. Schnablegger and Y. Singh, "The SAXS Guide: Getting acquainted with the principles," tech. rep., Anton Paar GmbH, 2013.

[172] I. ChorKendorff, *Surface Physics / Chemistry.* Center for Individual Nanoparticle Functionality, 2010.

[173] P. Malacrida, S. Horch, and I. Chorkendorff, *Alloys of Pt and Rare Earths for the Oxygen Electroreduction Reaction.* PhD thesis, 2014.

[174] By Claudionico commonswiki (Own work) [CC BY-SA 4.0 (http://creativecommons.org/licenses/by-sa/4.0)], via Wikimedia Commons, "Catalysisscheme." Online, June 2016. `https://commons.wikimedia.org/wiki/File%3AElectron_Interaction_with_Matter.svg`.

[175] C. Hamann, A. Hamnett, and W. Vielstich, *Electrochemistry.* Wiley-VCH, 1998.

[176] Pine Instrument Company, "Educator's Reference Guide for Electrochemistry," tech. rep., Pine Instruments, Grove City, 2000.

[177] K. Mayrhofer, D. Strmcnik, B. Blizanac, V. Stamenkovic, M. Arenz, and N. Markovic, "Measurement of oxygen reduction activities via the rotating disc electrode method: From Pt model surfaces to carbon-supported high surface area catalysts," *Electrochimica Acta*, vol. 53, pp. 3181–3188, feb 2008.

[178] Y. Garsany, O. a. Baturina, K. E. Swider-Lyons, and S. S. Kocha, "Experimental methods for quantifying the activity of platinum electrocatalysts for the oxygen reduction reaction.," *Analytical chemistry*, vol. 82, pp. 6321–8, aug 2010.

[179] U. Paulus, T. Schmidt, H. Gasteiger, and R. Behm, "Oxygen reduction on a high-surface area Pt/Vulcan carbon catalyst: a thin-film rotating ring-disk electrode study," *Journal of Electroanalytical Chemistry*, vol. 495, pp. 134–145, jan 2001.

[180] M. J. Fleige, G. K. H. Wiberg, and M. Arenz, "Rotating disk electrode system for elevated pressures and temperatures," *The Review of scientific instruments*, vol. 86, no. 6, p. 64101, 2015.

[181] C. M. Zalitis, D. Kramer, and A. R. Kucernak, "Electrocatalytic performance of fuel cell reactions at low catalyst loading and high mass transport.," *Physical chemistry chemical physics : PCCP*, vol. 15, no. 12, pp. 4329–40, 2013.

[182] M. Markiewicz, C. Zalitis, and A. Kucernak, "Performance measurements and modelling of the ORR on fuel cell electrocatalysts – the modified double trap model," *Electrochimica Acta*, vol. 179, pp. 126–136, oct 2015.

[183] G. K. H. Wiberg, M. Fleige, and M. Arenz, "Gas diffusion electrode setup for catalyst testing in concentrated phosphoric acid at elevated temperatures," *Review of Scientific Instruments*, vol. 86, no. 2, 2015.

[184] J. L. Dye and M. G. DeBacker, "Physical and Chemical Properties of Alkalides and Electrides," *Annual Review of Physical Chemistry*, vol. 38, pp. 271–299, oct 1987.

[185] M. J. Wagner, "Inorganic Nanomaterials Synthesis Using Alkalide Reduction," in *Encyclopedia of Inorganic and Bioinorganic Chemistry*, no. L, pp. 1–12, John Wiley & Sons, Ltd, 2011.

[186] W. L. Armarego and C. L. L. Chai, *Purification of Laboratory Chemicals*. Elsevier, 6 ed., 2009.

[187] A. Simas, V. Pereira, C. Barreto Jr., D. de Sales, and L. de Carvalho, "An Expeditious and Consistent Procedure for Tetrahydrofuran (THF) Drying and Deoxygenation by the Still Apparatus," *Quim. Nova*, vol. 32, no. 9, pp. 2473–2475, 2009.

[188] D. B. G. Williams and M. Lawton, "Drying of Organic Solvents: Quantitative Evaluation of the Efficiency of Several Desiccants," *The Journal of Organic Chemistry*, vol. 75, pp. 8351–8354, dec 2010.

[189] A. I. Yanson and Y. I. Yanson, "Cathodic corrosion. II. Properties of nanoparticles synthesized by cathodic corrosion," *Low Temperature Physics*, vol. 39, no. 3, pp. 312–317, 2013.

[190] Y. I. Yanson and A. I. Yanson, "Cathodic corrosion. I. Mechanism of corrosion via formation of metal anions in aqueous medium," *Low Temperature Physics*, vol. 39, no. 3, pp. 304–311, 2013.

[191] A. Yanson, P. Antonov, Y. Yanson, and M. Koper, "Controlling the size of platinum nanoparticles prepared by cathodic corrosion," *Electrochimica Acta*, vol. 110, pp. 796–800, nov 2013.

[192] National Institute of Standards and Technology, Gaithersburg, 2012, "Nist x-ray photoelectron spectroscopy database, version 4.1," June 2016. http://srdata.nist.gov/xps/.

[193] W. e. Haynes, *CRC Handbook of Chemistry and Physics : Internet Version 2016*. CRC Press, 96th ed., 2016. http://www.hbcpnetbase.com/.

[194] C. M. Pedersen, *New catalysts for miniaturized methanol fuel cells*. PhD thesis, Technical University of Denmark, 2015.

[195] G. Meyer and T. Staffel, "Die Tieftemperatur-Synthese von Oxidhalogeniden, YOX (X = Cl, Br, I), als Quelle der Verunreinigung von Yttriumtrihalogeniden, YX3, bei der Gewinnung nach der Ammoniumhalogenid-Methode. Die Analogie von YOCl und YSCl," *Zeitschrift für anorganische und allgemeine Chemie*, vol. 532, pp. 31–36, jan 1986.

[196] A. A. Permyakova, *Electrocatalysts and their Supporting Materials for Proton Exchange Membrane Fuel Cells: Activity and Durability Studies*. ph.d. thesis, Technical University of Denmark, 2013.

[197] H. Kleykamp, "Thermodynamics of the systems of the platinum metals with other transition metals: I. Integral data," 1993.

[198] L. Hellwig, *Thermodynamische Untersuchungen an den Systemen Yttrium-Platin und Neptunium-Platin durch EMK-Messungen mit galvanischen Festkörperketten*. No. November, Kernforscungszentrum Karlsruhe, 1978.

[199] G. Kemmler, "Untersuchungen zur stabilität von lanthaniden-platin verbindungen," Tech. Rep. Report No. KFK 2452, Kernforschungszentrum Karlsruhe, Germany, 1977.

[200] M. Mangelmann, "KFK 2107: Untersuchungen zur Stabilität von Erdalkali-/Lanthaniden-Edelmetallegierungen," tech. rep., Kerforschung Karlsruhe, 1975.

[201] A. Tursina, A. Gribanov, H. Noel, P. Rogl, and Y. Seropegin, "Crystal structure of the new ternary silicides Dy18Pt50+xSi16-x (x=0.28) and Y18Pt50+xSi16-x (x=0.56)," *Journal of Alloys and Compounds*, vol. 395, pp. 93–97, may 2005.

[202] D. Wang, Y. Yu, H. L. Xin, R. Hovden, P. Ercius, J. a. Mundy, H. Chen, J. H. Richard, D. a. Muller, F. J. DiSalvo, and H. D. Abruña, "Tuning oxygen reduction reaction activity via controllable dealloying: a model study of ordered Cu3Pt/C intermetallic nanocatalysts.," *Nano letters*, vol. 12, pp. 5230–8, oct 2012.

Appendix A

Crystal Structures

Table 7.1: List of the crystal structures used during the studies with corresponding ICSD database cards

Structure	ICSD database card
Pt	64923
Pt_2Y	105843
Pt_3Y	649852
PtGd	104120
Pt_2Gd	104121
Pt_3Gd	104122
PtTb	10511
Pt_2Tb	105807
Pt_3Tb	105808
Pt_3Fe	42588
PtSi	2623
YOCl	60586
Y_2O_3	16394
Gd_2O_3	40473
$Y_{18}Pt_{50.56}Si_{15.44}$	152705

Pt_5Y ($AuBe_5$)

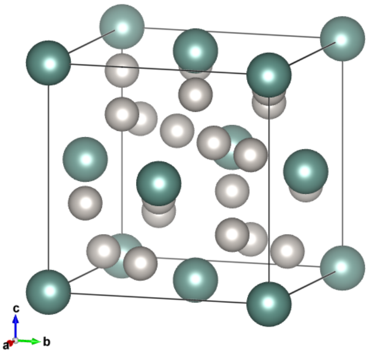

parameter	value
Space group	F -4 3 m
a Å	7.49000
b Å	7.49000
c Å	7.49000
$\alpha(^\circ)$	90.00
$\beta(^\circ)$	90.00
$\gamma(^\circ)$	90.00

Pt_5Y ($CaCu_5$)

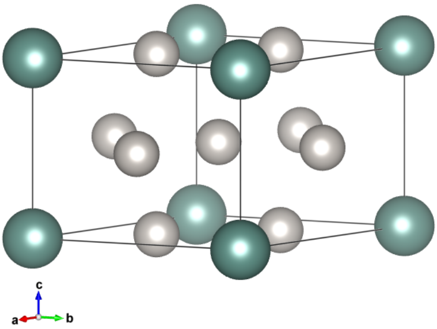

parameter	value
Space group	P 6/m m m
a Å	5.28060
b Å	5.28060
c Å	4.40740
$\alpha(^\circ)$	90.00
$\beta(^\circ)$	90.00
$\gamma(^\circ)$	120.00

Pt_5Y (DHCP)

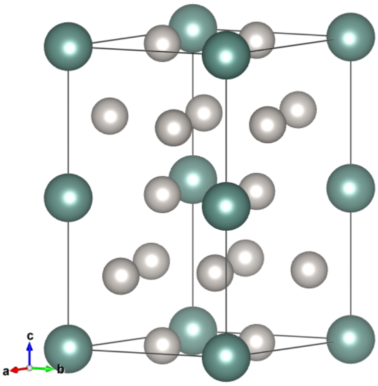

parameter	value
Space group	P 63/m c m
a Å	4.97660
b Å	4.97660
c Å	9.16960
$\alpha(^\circ)$	90.00
$\beta(^\circ)$	90.00
$\gamma(^\circ)$	120.00

Pt_5Gd ($CaCu_5$)

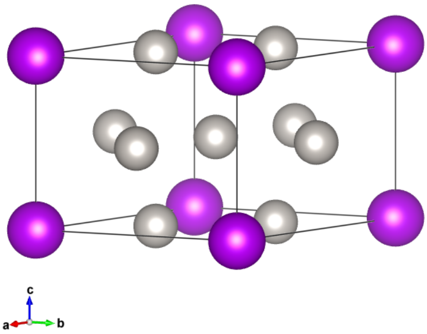

parameter	value
Space group	P 6/m m m
a Å	5.28000
b Å	5.28000
c Å	4.40000
$\alpha(^\circ)$	90.00
$\beta(^\circ)$	90.00
$\gamma(^\circ)$	120.00

Pt_5Gd (Ulrikkeholm *et al.*)

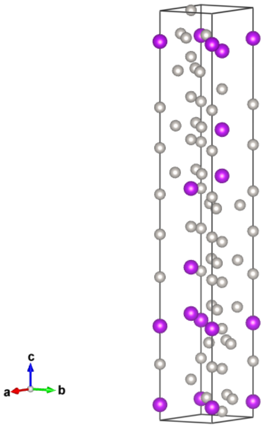

parameter	value
Space group	R 3 m
a Å	5.33090
b Å	5.33090
c Å	40.35800
$\alpha(^\circ)$	90.00
$\beta(^\circ)$	90.00
$\gamma(^\circ)$	120.00

Pt_3Tb ($GdIr_3$)

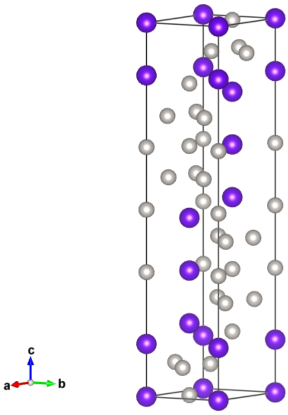

parameter	value
Space group	R -3 m
a Å	5.27246
b Å	5.27246
c Å	26.40555
$\alpha(^\circ)$	90.00
$\beta(^\circ)$	90.00
$\gamma(^\circ)$	120.00

Paper I

Scalable Synthesis of Carbon Supported Platinum - Rare Earth Alloys for use as Fuel Cell Cathodes

Brian P. Knudsen, Christoffer M. Pedersen, Amado Velázquez-Palenzuela, Leif H. Christensen, Ifan E. L. Stephens, Ib Chorkendorff,

In preparation

Scalable Synthesis of Carbon Supported Platinum - Rare Earth Alloys for use as Fuel Cell Cathodes

Brian P. Knudsen,[a] Christoffer M. Pedersen,[a,b] Amado Velázquez-Palenzuela,[a,b] Leif H. Christensen,[b] Ifan E. L. Stephens,[a] Ib Chorkendorff,[a]

[a] Center for Individual Nanoparticle Functionality , Department of Physics, Technical University of Denmark, DK-2800 Kgs. Lyngby, Denmark
[b] Center for Nano- and Micro technology, Danish Technological Institute (DTI), Gregersenvej, DK-2630 Taastrup, Denmark

Abstract

Platinum rare earth alloys have proven both active and stable under accelerated stability tests in their bulk polycrystalline form. However, a scalable method for the synthesis of high surface area supported catalyst of these alloys has so far not been presented. Herein we discuss the thermodynamics relevant for the reduction conditions of the rare earths to form alloys with platinum. We show how the tolerance for water and oxygen severely limits the synthesis parameters and how under certain conditions the thermal reduction of YCl_3 with H_2 is possible at temperatures above 500 ˚C. From the insight gained we have synthesized a Pt_xY/C catalyst by modifying a commercial TKK Pt/C catalyst and confirmed the alloying by both XRD and XPS measurements. The XRD spectra reveal crystalline intermetallic phases of Pt_xY and the metallic state of yttrium is confirmed by XPS. Without any optimisations to the method, the catalyst has an improved mass activity compared to the unmodified catalyst, proving the method viable. Improvement and optimization of the methods for obtaining a more phase clean and a more well-controlled size distribution of the alloy nanoparticles will be discussed.